UNIVERSITY OF OKLAHOMA

GRADUATE COLLEGE

METHODS FOR BLOCK FUNCTIONALIZATION OF CARBON NANOTUBES AND APPLICATIONS

A DISSERTATION

SUBMITTED TO THE GRADUATE FACULTY

in partial fulfillment of the requirements for the

Degree of

DOCTOR OF PHILOSOPHY

By

LAWRENCE WILLIAM BARRETT
Norman, Oklahoma
2019

METHODS FOR BLOCK FUNCTIONALIZATION OF CARBON NANOTUBES

AND APPLICATIONS

A DISSERTATION APPROVED FOR THE
SCHOOL OF CHEMICAL, BIOLOGICAL AND MATERIALS ENGINEERING

BY

Dr. Steven P. Crossley, Chair

Dr. Daniel E. Resasco

Dr. Brian P. Grady

Dr. Jeffrey H. Harwell

Dr. Daniel T. Glatzhofer

I would like to dedicate this work to my parents, John and Anita Barrett.

Acknowledgements

Dr. Steven Crossley for being my advisor throughout all of this. He has been a never-ending fountain of ideas and enthusiasm.

Dr. Daniel Resasco for encouraging me to approach everything critically.

Dr. Keith Hohn for starting me on the path to research and opening my eyes to just how much we don't know.

Committee member Dr. Harwell, Dr. Grady, and Dr. Glatzhofer for their assistance and guidance in this endeavor.

Fellow graduate students Nick Briggs, Fatoumata Ide Seyni, and Donald Jones, without their help I would not have been able to complete my project.

My mother and father, who have always held me to the highest standard, and who have done everything in their power to help ensure I can make it.

Andrea Kieffer, who will always be a close friend, for encouraging me though the tough times and being my inspiration.

Joshua Liebe and Andrew Woolley for keeping me from going insane after long nights in the lab.

Arron Collier and Jacob Hunt for leading me spiritually and helping me grow closer to the Lord my God.

Table of Contents

List of Tables

List of Figures

Abstract

This work has shown a method to produce block functionalized carbon nanotubes, BF-CNTs, with polymer covalently grafted to the sidewall with a selectivity along the length of the nanotube. This selectivity is reversible meaning either half can be polymerized. This was accomplished by doping the nanotube with nitrogen during growth. The nitrogen forms pyridine groups which then act as P-type dopants on the outer wall, weakening the bonds that CNTs form with radicals. This allowed a radical polymerization to selectively occur where the bonds were weak, allowing for a selective initiation of the polymerization reaction. These BF-CNTs were then placed at a polymer-polymer interface in which half the nanotube was selectively soluble in each phase, and the interfacial strength was tested with the asymmetric double cantilever beam test. The BF-CNTs showed interfacial toughness strengthening on par or greater than block copolymers, the currently accepted method.

BF-CNTs were also created with two different metals on the different ends of the nanotube. This was done by evaporation of the selected metal on each side of a thick vertically aligned nanotube forest. The nanotubes were then tested for a variety of reactions important to upgrading of biomass derived compounds to fuel based products based on the configuration of the metals on the nanotube, either touching or separated. The active sites for three reactions were able to be identified and were either created by promotor effects or were the result of short range interactions between the two components in the bifunctional catalyst system. Hydrogen spillover across the nanotube from one

metal to the other was observed in all cases, and is fast enough to not become a rate limiting step in the reactions tested.

Chapter 1: Introduction

Carbon nanotubes, CNTs, are a unique structure composed of linked benzene rings forming a cylinder with one or more walls, similar to an elongated fullerene[1]. CNTs have been at the forefront of materials sciences since their first intentional production[2,3], due to their unique chemical[4-7], electrical[8-10], and mechanical[11-13] properties, though their first use dates back to the 17th century[14]. Carbon nanotubes are considered among the strongest of materials when measured in the z direction[11,12], however fairly weak along the radial[15,16] direction and prone to fracturing upon bending. Regardless they have become a common additive in materials engineering[17-24] and are used for strengthening and tuning the electrical properties of numerous materials.

Functionalization of carbon nanotubes has been studied since their discovery, with nearly all methods relying on producing a defect in the wall of the nanotube. This is done with a strong oxidizing agent, typically refluxing nitric or sulfuric acid to produce carboxylic groups on the nanotube wall. The carboxylic groups then can go through subsequent acylation and amination reactions to attach organic functional groups. This form of functionalization is well characterized and often used to change the surface chemistry of the nanotube, resulting in enhanced interaction s between the nanotube and its surroundings. Acid oxidation introduces functionalities along the length of the nanotube indiscriminately, as well as destroys the nanotube lattice, resulting in a weakened nanotube. More recently work has been done in spatially controlled

functionalization, or asymmetrically functionalized nanotubes, to increase the various uses of the nanotubes.

The original site-specific functionalization of nanotubes was to use to carboxylic groups that occur naturally at the tips of a broken nanotube as the basis for functionalization. This yields a two phase three piece tube, with the two ends having the same functional groups and the bulk of the sidewall of the nanotube as unfunctionalized. This technique was first accomplished by Li et. al. as a method for detecting DNA[25]. Tip functionalization has also been accomplished by floating a forest of nanotubes on a photoreactive liquid by Dai et. al.[26]. By flipping the forest both tips were functionalized, and this is the first method to place different functional groups selectively on the different ends of the nanotube leading to the creation of the asymmetrically functionalized nanotube. This enabled realistic expectations of self-assembly of nanotubes into ropes[26], and idea which has yet to be realized.

Further asymmetrical tip functionalization was performed by Perepichka et. al. who attached oxidized single walled carbon nanotubes to a functionalized gold surface using ester bonds formed between the nanotube and the modified Au surface[27]. This left the free end of the nanotube available for functionalization. This method made two important advancements in asymmetrically tip functionalization carbon nanotubes. First it used wet chemistry and randomly aligned tubes so in theory it is scalable, and secondly it used masking in the process. The requirement of a gold surface and the

minimal fraction of nanotubes which actually align on the surface make this method impractical for mass production however.

Dai et. al. then expanded on the idea of asymmetrically functionalized nanotubes to form block nanotubes[18,28], that is nanotubes with functional groups not only on the tips, but along the length of the wall as well, while maintaining a spatial difference in the functional groups. This was done by masking half the nanotube by embedding a vertically aligned forest in a molten polymer, leaving the second half of the nanotube available for functionalization[18,28]. Dia et. al. did this functionalization via the SEED method to place a metal nanoparticle on the surface, but this method could be envisioned to used with an oxidation so that more traditional grafting methods can be used. Block nanotubes show promise in a variety of applications[18,19,27-30], but for any to be viable larger quantities need to be produced than can be by the masking technique.

One of the important uses for a block functionalized carbon nanotube, BF-CNT, is in polymer blends. Polymers tend to be immiscible in each other, leading to an emulsion like structure with a weak interface when polymers are mixed[19,31,32]. If a BF-CNT could be made with two different polymers attached to the surface it could enable to nanotube to span the interface and strengthen the material. It has already been shown that particles other than nanotubes can be forced to a 2-phase interface by selective surface chemistry compatibility[32-37]. With the amount of polymer blends created every year, either by recycling or

intentional production of new materials, this provides a large market for a block polymer functionalized nanotube.

Some work has been done in this area with noncovalently functionalized nanotubes[17]. By creating a 3 phase block copolymer: polymer A, polyethylene, polymer B, Schmaltz et. al. was able to adsorb the polyethylene section using the van der Waals forces on the nanotube. This allowed polymer A and B to align creating patches of similar functionalities around the nanotube, yielding a structure similar to a block nanotube, but control along the length of the nanotube was lacking. This method also has the weakness of not being covalently bound to the nanotube, so the weakest point in the nanotube-polymer interface, and the system may come apart when placed in a polymer blend, particularly under shear forces.

The purpose of this work will be to produce a block polymer functionalized carbon nanotube as depicted in Figure 1. All methods proposed in this work will be scalable to ensure the new method is useful for real world applications. It is our belief that growth followed by

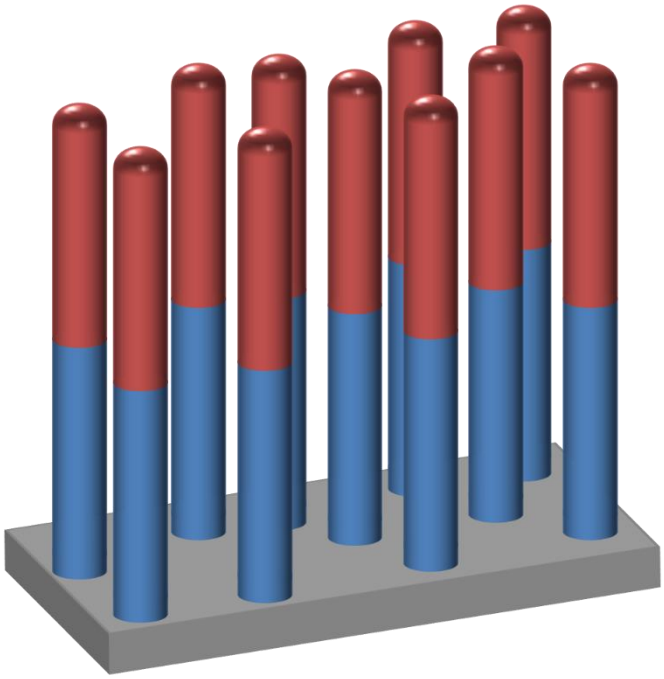

Figure 1: Block CNT forest demonstrating one functional group on top and one functional group on the bottom

subsequent functionalization are not scalable via current methods, as it will require careful manipulation of the nanotubes. For this reason, functionalities will be introduced during the growth process to ensure selectivity. These functionalities will then be used to attach a polymer to the nanotube. After new method of producing the block nanotubes are explored, new applications for BF-CNTs will be examined.

Chapter 2: Carbon Nanotube Growth and Purification

Introduction

CNTs are grown in one of several ways; arc discharge, laser ablation and chemical vapor deposition, CVD, are the most popular but hydrothermal and electrolysis methods are also used[38]. Arc discharge, also known as plasma discharge, is the method used by Iijima to first produce carbon nanotubes[2]. Two graphite rods are evaporated by applying a high voltage under moderate vacuum, with the distance between the rods being closely controlled to change the arcing that occurs[38]. This method is known for using significantly higher temperatures than the CVD method and as a result the nanotubes produced have on average a higher degree of crystallinity[1,38,39]. Growth rates can also be larger[1,38,39] as a result of the elevated temperature, but this is highly dependent of the feedstock and catalysts used in the CVD method[38]. The downside is the efficiency of the arc discharge method. A large amount of the evaporated carbon ends up in non-nanotube structures such as graphitic carbon and fullerenes[1,38,39].

Chemical vapor deposition is generally considered superior to arc discharge for commercial production, as it is often performed in a fluidized bed, a system that is easily scalable and well established in industry. Catalysts containing iron, cobalt, nickel, molybdenum and copper [1,38,39]in various combinations have been used successfully to grow nanotubes via the CVD method. The active catalysts have been supported on a wide array of semiconducting materials such as silica, alumina, and mica[30,39-42], as well as

cofed into the reactor as an organometallic compound[38,43]. CVD usually has light hydrocarbons, traditionally ethylene[1,38,39], flowing over reduced metal catalysts. Growth occurs either with the catalysts attached to the base substrate[44] or the nanotube attached with the catalyst particle elevated like a kite[44]. Base growth vs tip growth is controlled through the force attaching the particle to the substrate, with weaker attachments leading to tip growth. One easily observable factor for controlling tip vs base growth is the size of the catalyst particle, with larger nanoparticles leading to increased binding to the substrate and therefore more base growth[44]. Alumina can also be used to bind the nanoparticles to the substrate more strongly, which has the added benefit of preventing sintering of the nanoparticles, which would lead to the growth of carbon nano fibers rather than nanotubes.

The CVD method yields a higher purity nanotubes product than the arc discharge method[38,45,46]. The nanotubes, particularly when multiwalled, have more defects than in the higher temperature arc discharge method[38,39]. This weakens the nanotubes structurally, however the defects can be used as the basis for further functionalization[5,47]. The CVD method does yield product attached to a substrate, which requires further purification, but it is still the method used most by industry and was used for this project.

When spherical or porous substrates are used for the CVD method the resulting nanotubes are known as randomly oriented. Randomly oriented nanotubes are subject to fracturing from the mechanical forces of fluidized pellets colliding[40], and as such the final product tends to have a large dispersion

in length distributions. A more attractive growth orientation is vertically aligned nanotubes, in which all nanotubes have a overall parallel orientation to each other, and perpendicular to the substrate the catalysts is deposited on. Traditionally vertically aligned nanotube forests have been produced on large flat substrates such as silicon wafers[30,40], which provide easily characterizable forests but do not have a high surface area to volume ratio, making them unsuitable for mass production. They do have the advantage of remaining stationary in the reactor, or at least avoiding contact with each other's growing surfaces so the attrition common in the randomly aligned nanotubes doesn't occur. While a conveyor belt approach with airlocks on both ends could be dreamt of to mass produce nanotubes on such wafers, there have been more recent developments in growing vertically aligned nanotubes using materials with easily separated layers. Nanotubes grow both on the surface on these particles as well as inside the individual particles, see Figure 2. Such flat lamellar supports with very thin thicknesses offer more realistic industrial opportunities.

Using a lamellar support such as mica flakes allows for a flat substrate on which nanotubes can be grown, ensuring an even particle size distribution, which isn't always the case with rough spherical or porous particles. Mica give the additional benefit of protecting the inner forests from collisions with other fluidized particles, preventing attrition. The outer forests which are subject to abrasive action of the fluidized bed are also protected by decrease in weight of the particles which decreases the force on the forest when the particles collide

compared to alumina or silica particles. Several groups have reported growth on lamellar supports dating back to 2009[40,48-50] but lack a method of purification post growth. Earlier work by this research group has shown large quantities of vertically aligned nanotubes on muscovite can be grown depending on catalyst composition and growth conditions[40]. We studied a similar mica, one which is more capable of purification, but with similar surfaces for growth. A diagram of the catalyst impregnation on mica and subsequent nanotube growth is shown in Figure 2, with each sheet representing approximate 100 sheets of mica based on SEM images measuring the thickness.

The most promising method for producing a block functionalized nanotube in a scalable manner is to introduce the functionalities during growth to prevent the need for physical manipulation of nanoparticles to achieve the necessary spatial selectivity. Nitrogen interstitial atoms will be used as the primary functionality of the nanotube, and their uses will be discussed in detail

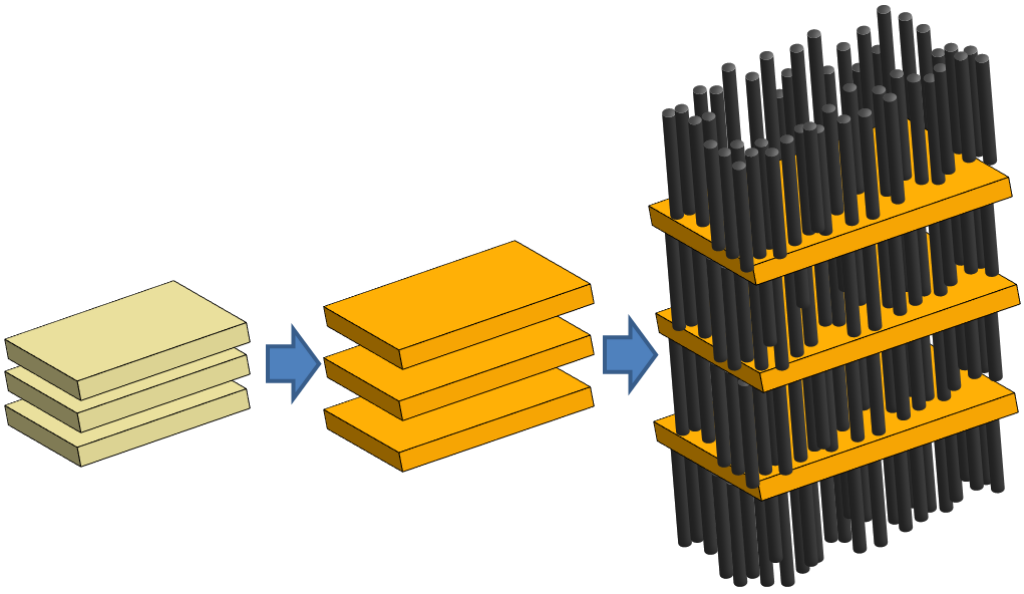

Figure 2:Catalysts impregnation of vermiculite and nanotube growth on vermiculite showing protection of forests from attrition

in Chapter 3. By growing approximately half the nanotube with nitrogen functionalities, also known as a nitrogen doped nanotube or a CN_xNT, and the second half of the nanotube without the interstitial nitrogen creates a block nanotube. Growth studies will be performed by changing the time and temperature of growth for each feedstock to ensure the two halves of the nanotube are roughly equal in length, as well as to ensure the nanotube is as short as reasonable. Short nanotubes will be preferential as they are less susceptible to breakage, which would destroy the block functionality. Diblock nanotubes of 1 micron in length is the goal, because numerous studies have shown that nanotube breakage below this starting length in melt mixing with a polymer tend to be small. Once the nanotubes are grown a novel purification method will be needed to prevent functionalization of the nanotube surface.

Traditionally nanotubes are purified via acid attacks such as HF or nitric acid, both of which can introduce functionalities[5,47,51] on the nanotube when they dissolve the substrate. Vermiculite is a lamellar structure in which each layer is magnesium oxide sandwiched between two layers of alumina silicate and has been shown to dissolve easily under both basic and acidic conditions.[52-54] both NaOH and HCl have been shown to be inert[47,55] with

pristine MW-CNTs so these will be the starting points for removal of the vermiculite support.

Experimental

Catalyst Production and Growth

All chemicals used were obtained from Sigma Aldrich and were of ACS reagent grad >98% or higher. All gasses were ultra-high purity, or in the case of air grade zero, and were purchased form Airgas. All water was obtained through an in house Col Parmer filtration set up which produced water with a pH of 6.7. Vermiculite (Sigma Z765422) was suspended in nanopure and homologized by a IKA T-25 homogenizer operating at 10,000 hertz. The vermiculite was then wet sieved to between 150 and 350 microns. This was done to prevent mass transfer issues in the large particles. A catalyst solution of 1.11 wt% iron (III) nitrate nonahydrate (Sigma 216828), 1.23 wt% aluminum nitrate nonahydrate (Sigma 237973), and 0.39 wt% cobalt (II) nitrate hexahydrate (Sigma 239267) all with respect to water, which was 18MΩ. The catalyst solution was then wet impregnated into the vermiculite, followed by calcination in air at 450°C for 1 hour. The catalysts impregnation was repeated 3 times in total to ensure maximum coverage.

To determine growth rate, it was advantageous to only have one forest, so silicone wafers were used for a support. The silicon wafers were cut to 22 mm, calcined at 600°C for 2 hours to form a silica layer on the surface which was found to prevent sintering of the particles. The wafers were then washed with acetone, ethanol, and isopropyl alcohol to clean the growth surface. The

catalysts solution mentioned above was modified to contain 7.5 g/L 2-hydroxyethyl cellulose with a MW of 1,300,000 (Sigma 434981) to increase viscosity. The new catalysts solution was spin coated onto the wafers at 2000 rpm. Subsequent calcination and growth procedures match the vermiculite growth conditions.

For growth on the vermiculite 5 grams of catalysts was placed in a vertical quartz tube 1” in diameter, when the wafers were used 2 wafers were placed back to back in a horizontal quartz tube. In either case reduction of the catalyst was achieved by ramping the reactor at 10°C/min from room temperature to 650°C under a flow of 200 sccm, followed by a 30 minute isothermal reduction. The gas was switched to 200 sccm of argon as the reactor ramped to the desired growth temperatures, either 675°C or 725°C. For pristine nanotubes, 200 sccm of ethylene was flowed into the reactor, which raised the fluidization height to 18”. For CN_xNTs acetonitrile (Sigma 271004) was used as the feedstock at a rate of 300 ml/hr. The acetonitrile was preheated to 80°C prior to injection and allowed to evaporate into the reactor with the carrier gas. Feedstock gasses were shut off at the end of the growth period and the carrier gas flow was continuous throughout the growth and cooldown procedure.

Purification

Nanotubes grown on wafers were not purified, as they were used only to test growth rate. All purification was done on nanotubes supported on vermiculite. Anhydrous sodium hydroxide (Sigma 795429) was placed in a steel

beaker and heated to 400°C. Once the NaOH was completely liquid the CNTs on vermiculite was stirred into the solution and held at 400°C for 5 minutes. The solution was cooled to room temperature and dissolved in 3 L of water under moderate stirring for 2 hours to solubilize sodium silicates. Excess NaOH and the water soluble products were removed from the nanotubes by vacuum filtration. The resulting solids were weighed and dispersed in 100 ml of water. The solution was reacted with 10% stoichiometric excess 1 M HCl, assuming the entire weight of the solid product had been $Mg(OH)_2$, and allowed to stir for 2 hours. The CNTs were then filtered a second time which removed MgCl and solubilized iron from residual catalysts particles.

Analysis

Nanotube length was measured via SEM on a Zeiss Neon operating at 1 keV. Forests grown on wafers were split in half and the interior of the forest was measured at 4 points to obtain an average forest height away from potential edge effects. TEM was used to study the juncture between the CN_xNT and CNT segments, as well as the nanotube width. TEM was performed on a Zeiss 10A operating at 80 keV. Nanotube samples were dispersed in IPA by bath sonication for 1 minute and placed dropwise onto copper grids with a lacy carbon coating.

Thermogravimetric analysis, TGA, was performed to measure purity of the samples on a Netzsch STA 449F1. TGA was performed under a blanket of 60 sccm of air for TPO and 60 sccm Ar for TPD studies. Temperature ramp was from room temperature to 700°C with a rate of 2°C/min to minimize heat

transfer issues inside the crucible. Outlet gasses were measured by an Aeölos quadrapole mass spectrometer, scanning each mass from 2-200 for 0.25 seconds.

Results

Growth

Prior work in this group has shown growth with ethylene to be faster than growth with acetonitrile, so the growth temperature of ethylene was 675°C and the growth temperature for the nitrogen doped nanotubes was increased to 725°C to compensate. At 675°C the growth rate of nanotubes with ethylene was found to be 1.7 microns/minute, which matches very closely the 1.8 microns/min found using acetonitrile at 725°C. The growth measurements can be seen in Figure 3.

After initial growth rates were assessed on the silicon wafers a two phase growth was attempted, with the nitrogen doped phase occurring first at 725°C , followed by a cooldown and growth at 675°C with ethylene. During the cool down phase, a layer of carbon seemed to form, and can be seen in Figure 4. All SEM images of acetonitrile growth showed a thin layer of amorphous carbon near the bottom of the forests. It has been theorized that nanotubes

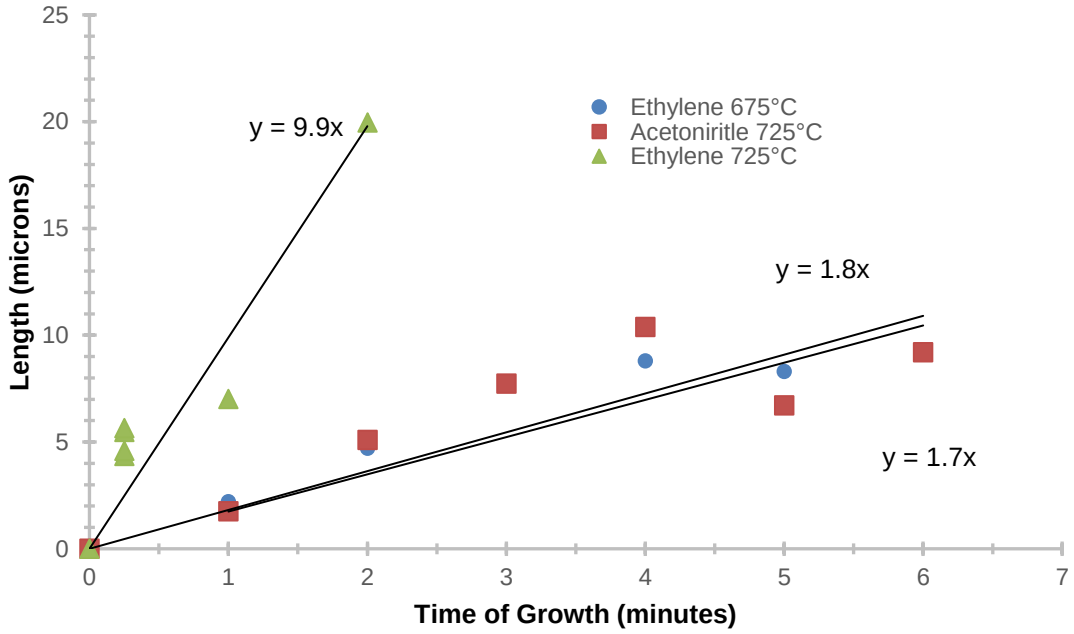

Figure 3: Growth rates of carbon nanotubes using various feedstocks and temperatures as a function of time using acetonitrile and ethylene as feedstock. Growth rates were measured from forests grown on silicon wafers

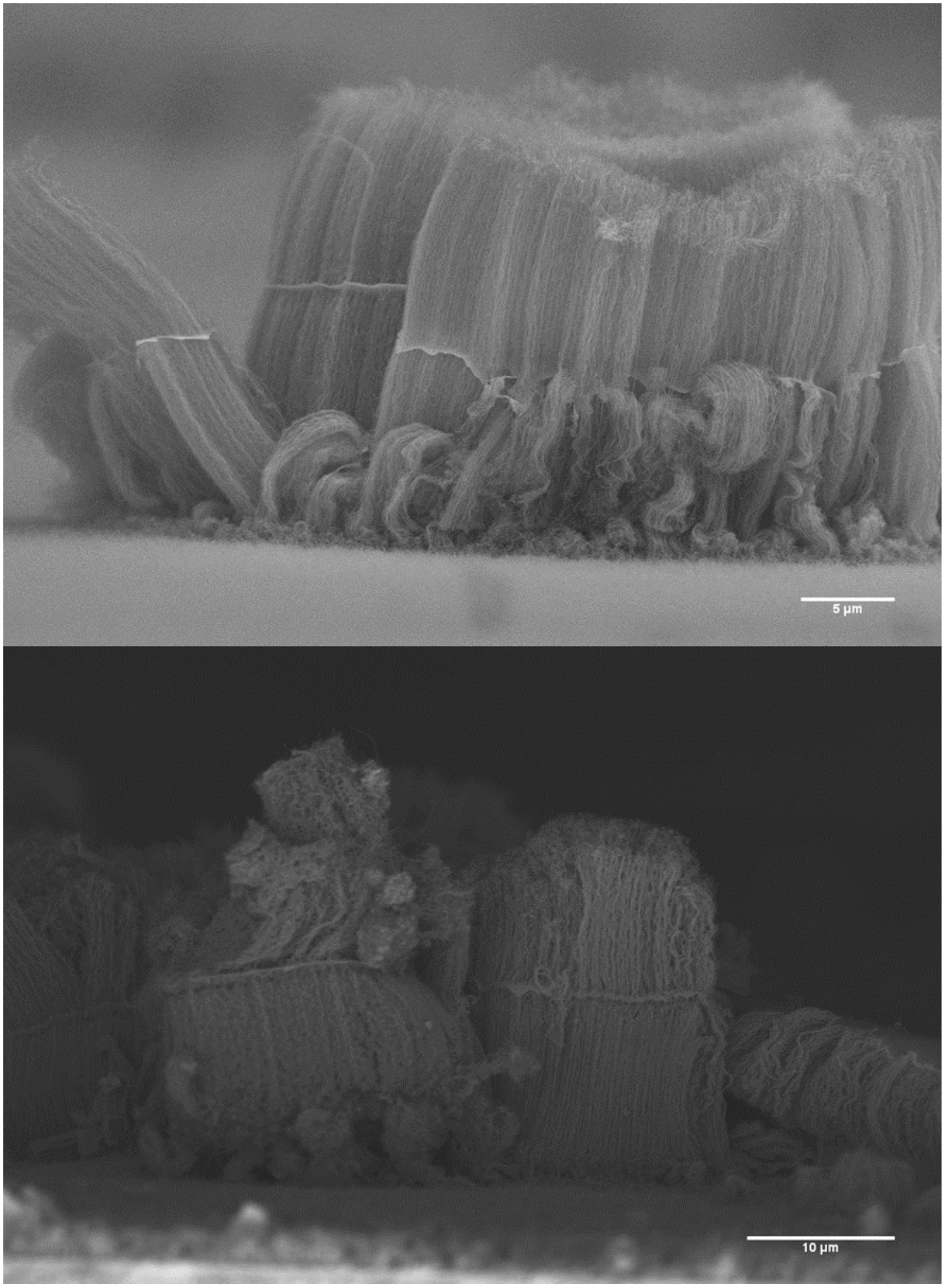

Figure 4: SEM of CNTs grown in two phases: 725°C with acetonitrile, 675°C with Ethylene. Two distinct phases are seen separated by a layer of amorphous carbon

grow via a radical reaction after the feedstock dissociates on the metal catalysts particle[44,56]. This layer of amorphous carbon should then be radical carbon which has spilled over from the catalyst and polymerized on the surface. If the ethylene then penetrates through the amorphous carbon layer and starts the nanotube growth process again it is possible the amorphous carbon layer is then carried up by the growth of the nanotube, which would explain the presence of amorphous carbon halfway up the forests.

This is assuming a base growth method as opposed to tip growth, and that the catalysts particles are bound to the substrate, while the amorphous carbon is loosely bound to the substrate but are tightly bound, perhaps even chemically linked to the nanotube. This allows for a potentially interesting structure where two halves of a nanotube are physically separated from each other. Future work should be focused on this phenomenon, but it is considered undesirable for the block functionalized nanotube project for several reasons. The amorphous carbon may be concealing a break in the nanotubes, such that the top and bottom half of the forest may not be connected. Alternatively, if they are connected the amorphous carbon will need to be removed to use the nanotubes as individual anchors in the polymer matrix.

To prevent the growth of the amorphous carbon, a second set of growth trials was performed with ethylene flow at the same temperature as the acetonitrile growth, 725°C. In this case the pristine non-doped nanotubes were found to grow at a rate of nearly 10 microns/min. When the block nanotubes were grown no amorphous carbon layer was observed under SEM. Figure 5

shows a SEM image of the block nitrogen doped nanotubes grown on a single sheet of vermiculite. The vermiculite sheet in the middle has nanotube growth on both sides, and a clear color change in the nanotubes where the amorphous carbon layer had been in the case of two growth temperatures. Nitrogen doping of nanotubes is known to change their conductivity, and it is believed that this conductivity difference is the reason for a color change under SEM. This color difference can only be seen at extremely high contrast ratios, indicating it is faint.

TEM further showed a CN_xNT portion of nanotube connected directly to a pristine section. Nanotubes grown with acetonitrile under these conditions are known to exhibit a bamboo like structure commonly referred to as herringbone

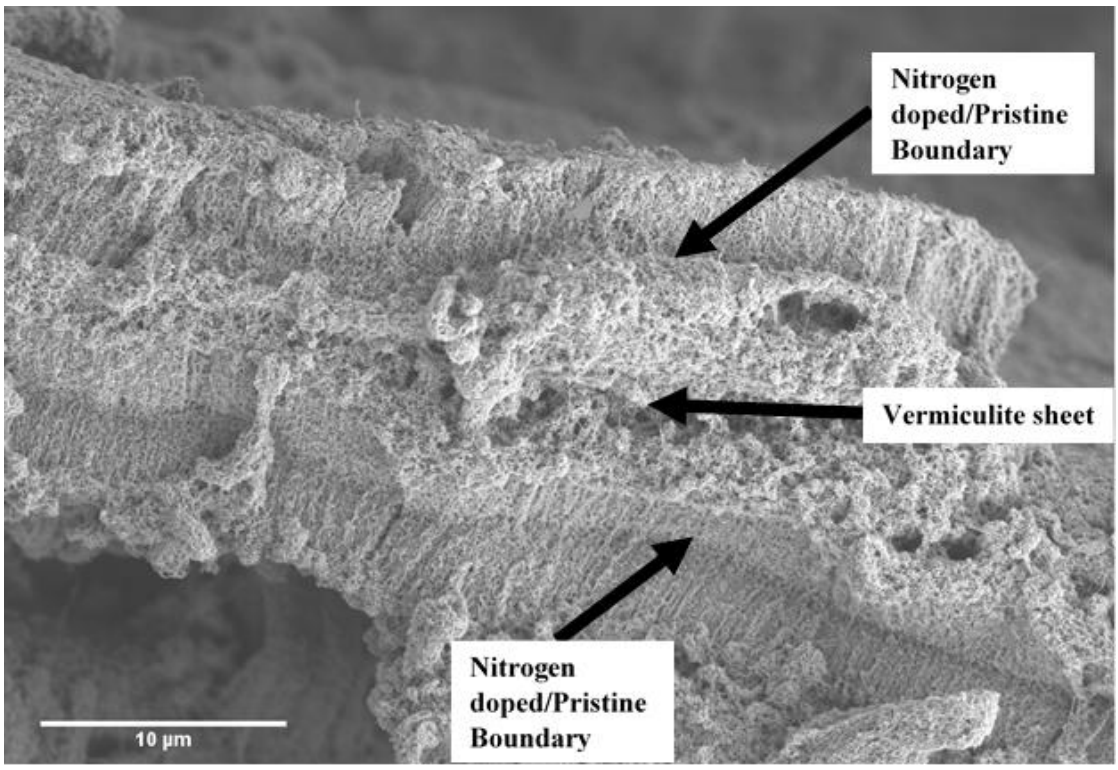

Figure 5: SEM of block nitrogen doped nanotubes grown on a single sheet of vermiculite. A color change is observed at the boundary between the nitrogen doped section and the pristine section.

structures. These will be discussed in more detail in Chapter 3 but are useful for

identifying the nitrogen doped portion. Figure 6 shows several TEM images of nanotubes which contain herringbone structure on one end, and no herringbone structure on the other end. This is conclusive evidence of a block nitrogen doped nanotube, which will be used in the remainder of this work. A transition region can be seen in between the two phases, where the acetonitrile flow had stopped, but had not yet been purged from the reactor.

Purification

Purification of the nanotubes was accomplished on the nanotubes grown

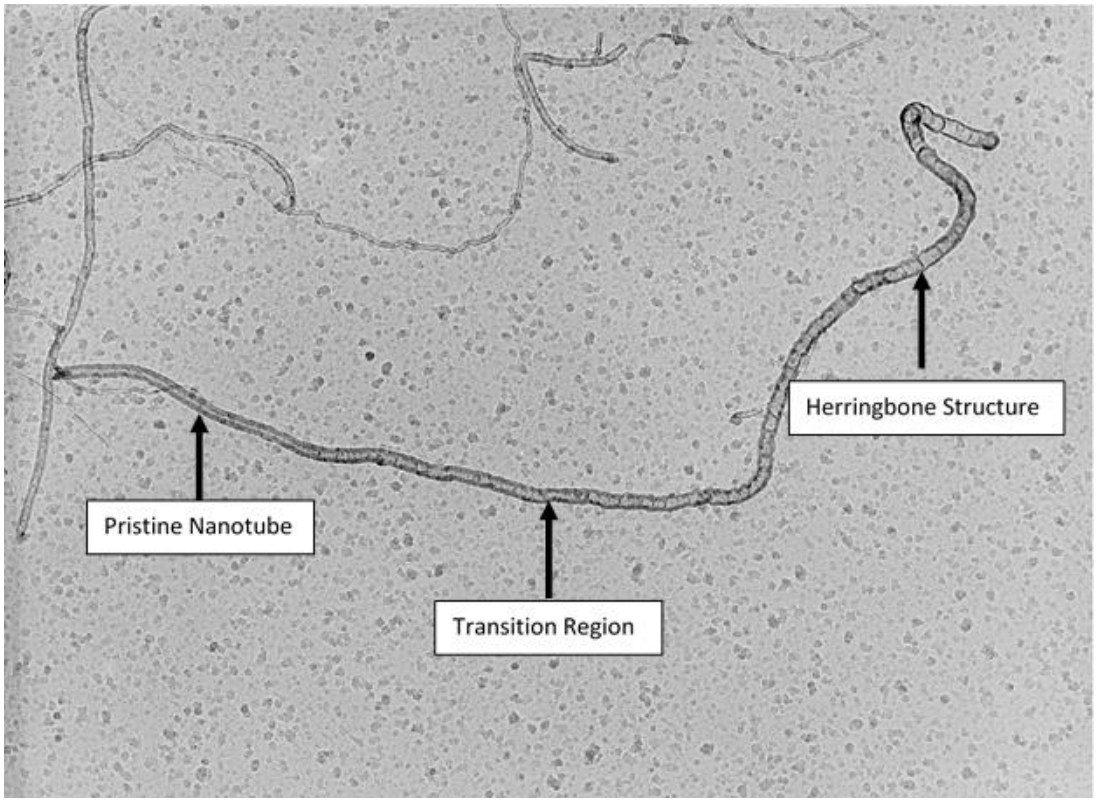

Figure 6: TEM image of block nitrogen doped nanotube showing herringbone structure on one end and no herringbone structure on the other end, indicating half block half pristine with a short transition region in the middle.

on vermiculite and was accomplished in two steps. Liquid NaOH was used to dissolve the alumina silicates into short chain sodium silicates and aluminum

hydroxide, both of which are water soluble under basic conditions. SEM with EDX confirmed after the first filtration step only magnesium, carbon, and oxygen remained, all silicon, aluminum and metal catalysts had been removed. A further washing with dilute HCl was sufficient to remove the MgOH leaving behind the carbon nanotubes. Neither treatment is capable of functionalizing the nanotubes[5,47,55].

TGA was used to test the purity of the nanotubes and can be seen in Figure 7. Initial nanotube purity is 28 wt% which is much higher than the same nanotubes on silicone wafers, <1 wt%. Purity on the vermiculite is significantly below levels found in literature on mica supports, as is expected. The majority of work in the literature has been focused on growing the maximum length of nanotube, which would necessarily increase the CNT wt%, while this work is focused on growing short nanotubes. A slight dip just prior to 300°C can be observed in both cases, and is attributed to the burning of amorphous carbon, which is known to decompose prior to crystalline carbon. Residual mass is attributed to iron catalysts particles protected from the purification process by the nanotubes and were composed of a fine red powder that was responsive to magnetic stimulation. Final purity of the product was found to be

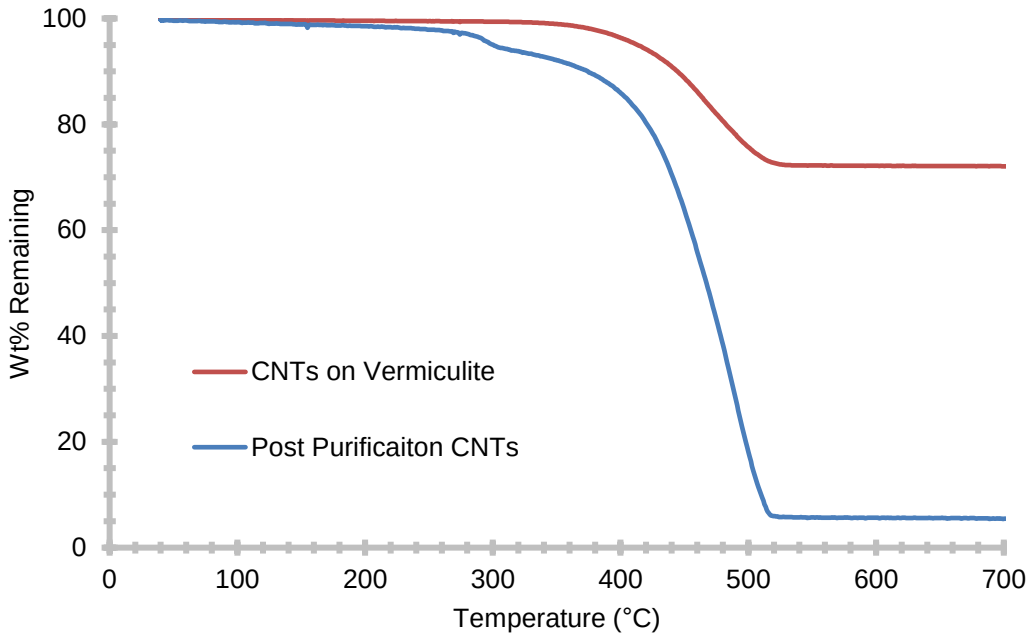

Figure 7: TGA in air of block nanotubes before and after purification process showing a significant increase in the wt% carbon after purification. MS indicates the drop in weight immediately prior to 300°C is carbon material, likely amorphous carbon.

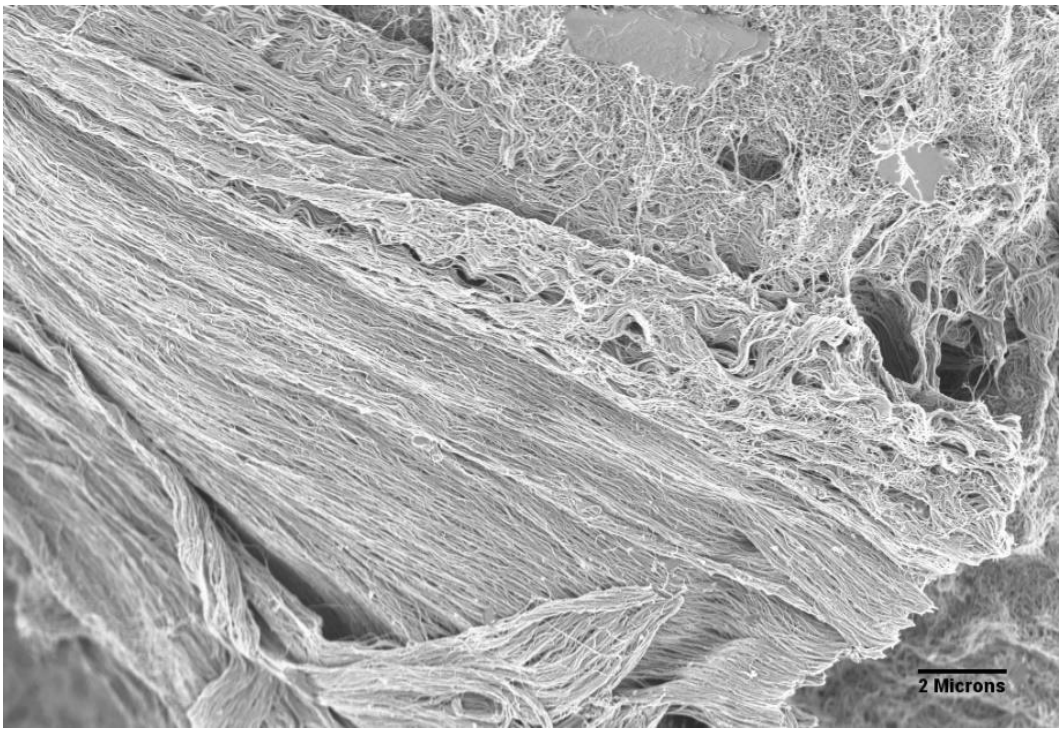

Figure 8: CN_xNTs grown on vermiculite and purified to test forest cohesion through purification process.

90 wt% CNT, 5 wt% amorphous carbon, and 5 wt% residual iron trapped inside the carbon nanotube.

SEM was performed on the nanotubes to determine the extent of breakage of both the individual nanotubes as well as the forest during the purification process. Nitrogen doped nanotubes were used for this case as they are more soluble in water than the pristine nanotubes, due to the hydrogen bonding between the pyridine groups and the water, which should allow the forest to come apart easier. The nanotubes total initial length was 25 μm, as long tubes break more easily than short tubes. This represents a worst-case scenario for breaking both the forest and the nanotubes. The longer forest should show increased cohesion, but this should be mitigated by the likelihood of fracturing the tubes. An example of the nanotube forest after purification can be seen in Figure 8, which shows the nanotube array held together and breakage of the nanotubes did occur around the edges of the forest but for the most part was negligible. This is attributed to the lack of sonication throughout the process which is common in nanotube processing.

Conclusions

Block nitrogen doped nanotubes were grown on a support consisting of flat lamellar layers both on the outside of the structure, as well as the inside of vermiculite, between the layers. TEM and SEM were both able to identify two phases on the nanotubes corresponding to functionalities introduced by changing the feedstock by the herringbone structures and conductivity change in the nanotube based on its composition. Purification was accomplished via

sequential base/acid attacks to yield a 90 wt% pure nanotube product from a mica support. The total length of the nanotubes was between 5-10 microns, with minimal breakage during processing. These processes together have led to a block functionalized nanotube produced in a scalable manner, something which has never been accomplished before.

As is, the two types of tubes were always in the higher surface energy phase in the polymer blends that were investigated. For this work, we wish to us blends of polystyrene (PS) and poly(methyl methacrylate) PMMA) because both polymers are amorphous and because this blend system has been studied extensively. Hence, further work will need to be focused on a reaction scheme to differentiate the two blocks so that one block resides in PMMA and other resides in PS.

Chapter 3: Nitrogen Functionalization of Carbon Nanotubes

Introduction

The purpose of this work is to create asymmetrically functionalized nanotubes in a mass producible way. Until vertical alignment of randomly oriented nanotubes becomes possible the most efficient way to control the location of functionalities on the nanotubes is to place the functionalities during the growth process. Nanotube growth is a one-dimensional process, meaning the catalyst will facilitate growth in the z direction, but not expand the nanotube radially. Additionally, functionalities not present at the moment a segment grows will not be incorporated to a large extent into that segment at a later time during the growth, but can be added later from a variety of active species[57-59]. The strategy employed then will rely on changing the nanotube feedstock to change the chemistry along the length of the nanotube.

One of the most well studied functionalities to add to a carbon nanotube is nitrogen. Due to the size of a nitrogen atom relative to carbon, it fits easily into the carbon lattice, making the doping process easier[60]. Additionally, it causes significant changes in nanotube properties[60,61]. Changes in hardness[61], conductivity[61-64], radical scavenging[6] and chemical reactivity[59,61,63,64] have all been observed. In Chapter 2 the growing of pristine and nitrogen containing carbon nanotubes is discussed, and a method for creating a half and half nanotube where the nitrogen functionalities are asymmetric along the z axis to use these changes in properties for further functionalization.

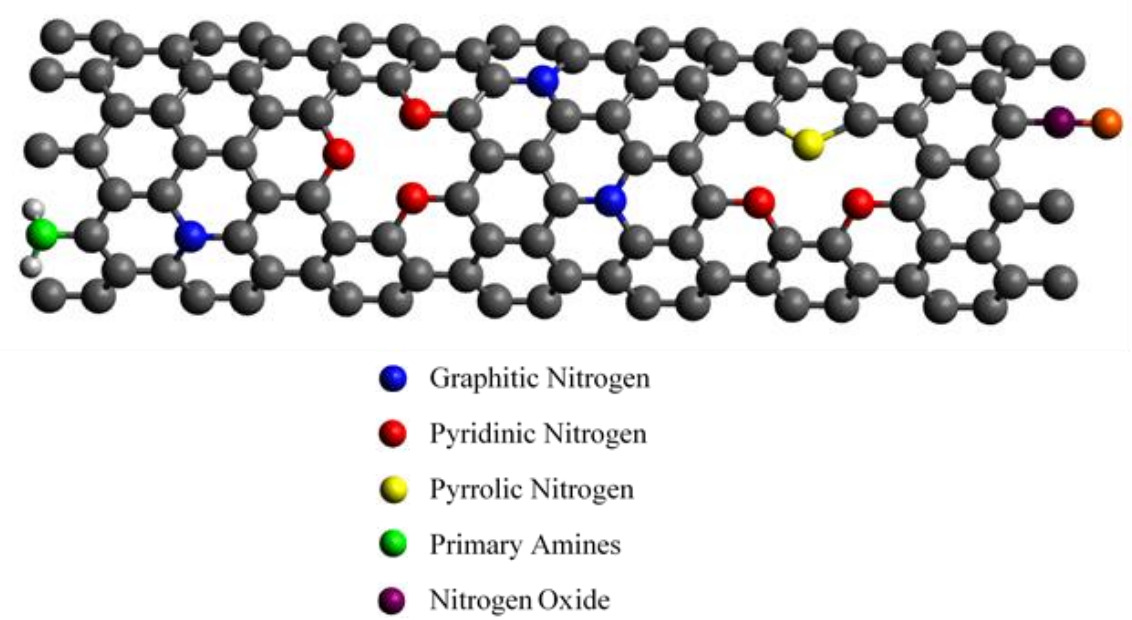

Nitrogen Species

Figure 9: Carbon nanotube showing different types of possible nitrogen functionalities

Nitrogen can be incorporated into the nanotube from a variety of feeds stocks, either pure compounds such as acetonitrile, pyridine[65], or phthalocyanine[45,46,66,67] or a mixture of nitrogen containing compounds[68,69]. The starting feedstock has a large control over both the species of nitrogen that is incorporated initially[68,70-72], as well as the extent to which nitrogen is incorporated[43,72,73]. There are 5 main species of nitrogen often incorporated into the nanotube[65,68,73-76], which can be seen in Figure 9. Pyridinic nitrogen refers to a SP2 hybridized nitrogen which is a member of a 6-atom ring and is bonded to two carbon atoms. Pyrrolic nitrogen is similar to pyridinic nitrogen with the exception of being a member of a 5-atom ring. Both forms are sp^2 hybridized and derive their names from the simple organic structure pyridine and pyrrole. These structures ordinary occur in clusters to stabilize the defects[65,73,77-79]

caused by the nitrogen, though on small diameter nanotubes have been shown to be stable with a carbon vacancy[80]. These forms of nitrogen have been shown to have a p type dopant effect on graphene[77,81], and should exhibit similar effects on CNTs. Two of the nitrogen electrons form sigma bonds with the carbon atoms, two e^- form a lone pair, and the last valence electron occupies a place in the pi carbon-nitrogen bond, leaving one spot in the pi bond open, thus exhibiting an n-type dopant effect on the nanotube.

Graphitic nitrogen, properly known as fully coordinated nitrogen, has a carbon-nitrogen bond with three different carbons[68,73,76] . Graphitic nitrogen will act as an N-type dopant[81] as four of the five valence electrons from the nitrogen will go to the sigma and pi orbitals, resulting in a single extra electron. This will potentially yield two methods for functionalizing the nanotube, utilizing both the n and p type dopant structures. Literature from Wang et. al. and Payne et. al. suggests the distance over which the dopant effects are distributed are on the order of a new nanometers, though there is a substantial difference between semi conducting and metallic nanotubes[64,77]. As the nanotubes are multiwalled both orientations can be present, so the nanotubes will be assumed to be as conductive as possible with regards to the distance of the charge delocalization. This characteristic gives hope to the idea of spatially separating the nitrogen doped and pristine section of nanotube will allow for a selective block functionalization. Alternative if the p and n type dopants cancel each other out, the electronic effects of the dopant could be moot which will limit possible functionalization routes.

Primary amines can form, though typically through post growth functionalization rather than nitrogen doping during growth[76] and are also shown to be p type dopants. Lastly is nitrogen oxide, which is a SP3 hybridized nitrogen bonded to two carbons and an oxygen[73,76]. Each species can be identified by XPS binding energy[68,73,76], pyridinic: 398.5 eV, pyrrolic: 400.1 eV, graphic nitrogen and protonated pyridinic nitrogen: 401-403 eV, nitrogen oxide: 403.5 eV[76].

Determining the exact species of nitrogen present is difficult without access to XPS. Relying on literature, Bulusheva et. al. found at 800°C using pure acetonitrile the nanotubes contained 3 at% nitrogen and contained pyridinic, graphitic and pyrrolic nitrogen in a ratio of 4:4:1. Other groups have found up to 20 at% nitrogen[41] from acetonitrile, however the catalysts and growth laid out by Bulusheva et. al. is most closely related to the conditions outlined in Chapter 2. Bulusheva et. al. went on to use near edge XAFS combined with XPS to show the ratio of graphitic and pyridinic/pyrrolic nitrogen is not uniform across the walls of a MW-CNT. Pyridinic and pyrrolic nitrogen are most likely to exist on the outer walls of a nanotube, where graphitic nitrogen is in higher abundance vs. the inner walls

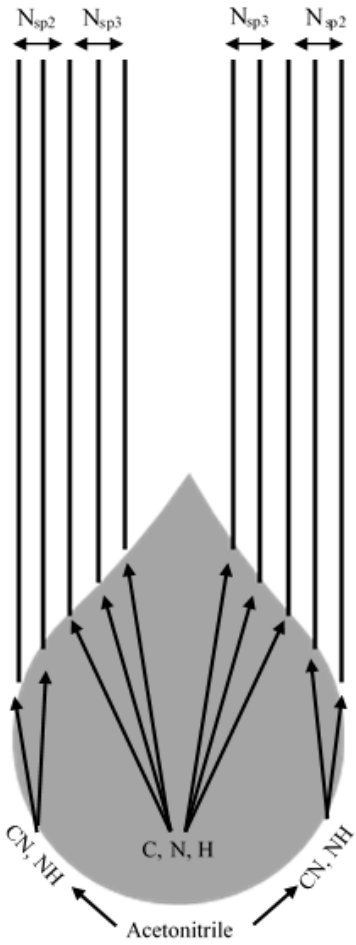

Figure 10: CN_xNT growth mechanism explained by Bulusheva, showing a concentration gradient between the nitrogen species of the inner and outer walls.

of a MW-CNT[68]. They attribute this to two different growth mechanisms. The carbon structure formed on the surface of the catalyst particle, which becomes the outer walls of the nanotube, is formed from C-N and N-H dissociated species which can only diffuse through a small amount of the catalysts. The smaller species of individual C and N atoms can diffuse faster through the catalyst and thus can move through the bulk of the catalysts particle and form the inner walls of the nanotube. This explanation is supported by the existence of N_2 inside the walls of the nanotube, which could only have been formed by two single nitrogen atoms coming together inside the catalyst particle. A diagram depicting the proposed mechanism can be seen in Figure 10. If this mechanism is true, then the planned functionalization route can focus on using p type dopants, as they will be more abundant on the surface, assuming they are not negated by the n type dopants.

Pristine nanotubes were functionalized with ammonia post growth by Schlögl et. al. and heated in situ while monitoring the binding energy of the nitrogen groups by XPS, as well as the off put gasses by MS. They found that upon heating the most abundant form of nitrogen in a CN_xNT can change[76] from primary and secondary amines to the more stable graphitic nitrogen. This is attributed to a thermal desorption of the less tightly bound primary amines as well a dynamic surface rearrangement that forms pyridinic nitrogen below 450 K. Above this temperature a small portion of sp^2 hybridized nitrogen decomposed or was converted into graphitic nitrogen. This suggests that at growth temperatures of 725°C, few if any primary amines should be present,

which is in agreement with the Bulusheva et. al. experimental results of growth with acetonitrile, and the DFT studies of Wang et. al. that concluded the sp^2 hybridized nitrogen were more stable than primary nitrogen in graphene, while graphitic nitrogen is the most stable[77].

Growth Mechanism

Although not directly relevant to the planning of a functionalization route, the growth mechanisms of CN_xNTs proved to be very interesting. The herringbone structure described in Chapter 2 was used to prove a single nanotube could contain portions which were nitrogen doped and non-nitrogen doped. The mechanism laid out by Bulusheva et. al. describing the movement of single atoms through the catalyst nanoparticle bulk does not fully explain the presence of the bamboo structures. Bamboo-like structures were first observed in 1993 in nanotubes formed without a nitrogen containing precursor[82]. Terrones et al. first described the growth of CNTs using a nitrogen containing precursor, acetonitrile, in 1996 and viewed the same bamboo like structures under TEM[83]. Terrones proposed a mechanism in which only a small portion of the catalyst nanoparticle is exposed, and the rest is covered with the outer wall of the carbon nanotube. The small exposed area allows the feedstock to dissociate on the surface and diffuse through the nanoparticle and form a new internal wall, which increases pressure on the catalyst particle. Growth of new inner walls continues until the catalyst particle slips out of the nanotube enclosure made by the nanotube walls and proceeds to repeat this cycle of growth, entrapment, pressure buildup, and release. This mechanism has been

generally accepted but can only be used to explain tip growth method. Base growth method requires the catalyst particle to be bound to the surface, which wouldn't leave the needed area for new feedstock adsorption and dissociation. Additionally, no reason was proposed why this doesn't occur with all nanotubes, though it could be the nitrogen doped nanotubes provide more nucleation points for the crystallization of the nanotube to start, so it will cover the catalysts particle faster than in a non-nitrogen containing case.

More recently work by Holmes et. al. has developed a new theory which can be seen in Figure 11. Rather than increasing the number of internal walls causing pressure that leads to slip, they suggest the mechanism is caused by competition between the nanotube-metal bond strength and a minimization of the surface energy of the nanoparticle[84]. Using DFT, they calculated the bond energy of a carbon-nanoparticle and nitrogen-nanoparticle bond for various configurations of Co/Mo catalysts, and found the nitrogen-metal bond to be significantly stronger than the carbon-metal bond. This leads to a pinning effect where the locations of the nitrogen functionalities bond strongly to the metal catalysts. As a result, the nanoparticles are elongated inside the nanotube as they are continually stuck to nitrogen doped points. Eventually the formation of new internal walls increases pressure to the point it outweighs the energy penalty of desorbing at the nitrogen sites, leading to the slip theorized by Terrones et. al.

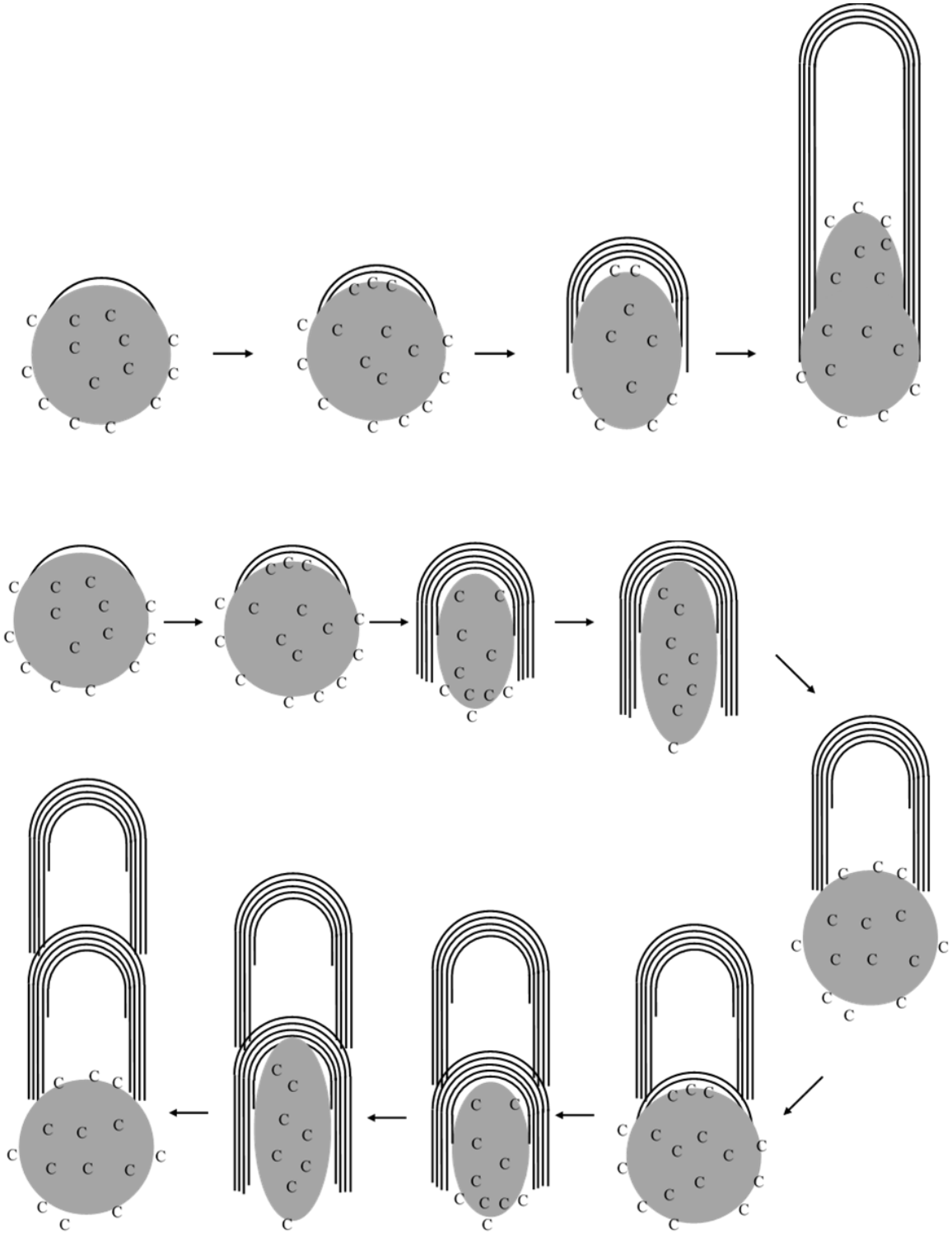

Figure 11: Top- Mechanism for growth of traditional nanotube as the catalyst nanoparticle continually moves as the nanotube walls grow. Bottom- Mechanism for CN_xNT growth proposed by Holmes showing a slipping mechanism.

and the structures seen under TEM. This theory also explains why the bamboo structures aren't observed over nickel catalysts[85], as well as the slower growth rate of the nitrogen doped nanotubes as opposed to the nanotubes grown with ethylene.

CN_xNT Characterization and Discussion

The initial test for nitrogen doping was to examine the nanotubes under TEM and attempt to identify the herringbone or bamboo like structures noted in literature. Figure 12 shows TEM images with heaving herringbone structure on the nanotubes grown with acetonitrile, indicating the nanotubes likely contained nitrogen. Nitrogen loading on the nanotubes was measured by TGA in air with the resulting gasses analyzed by an onstream MS as described in the procedure for Chapter 2. NO and NO_2 were observed coming off above 400 °C, at the same time CO2 was forming, indicating the NO and

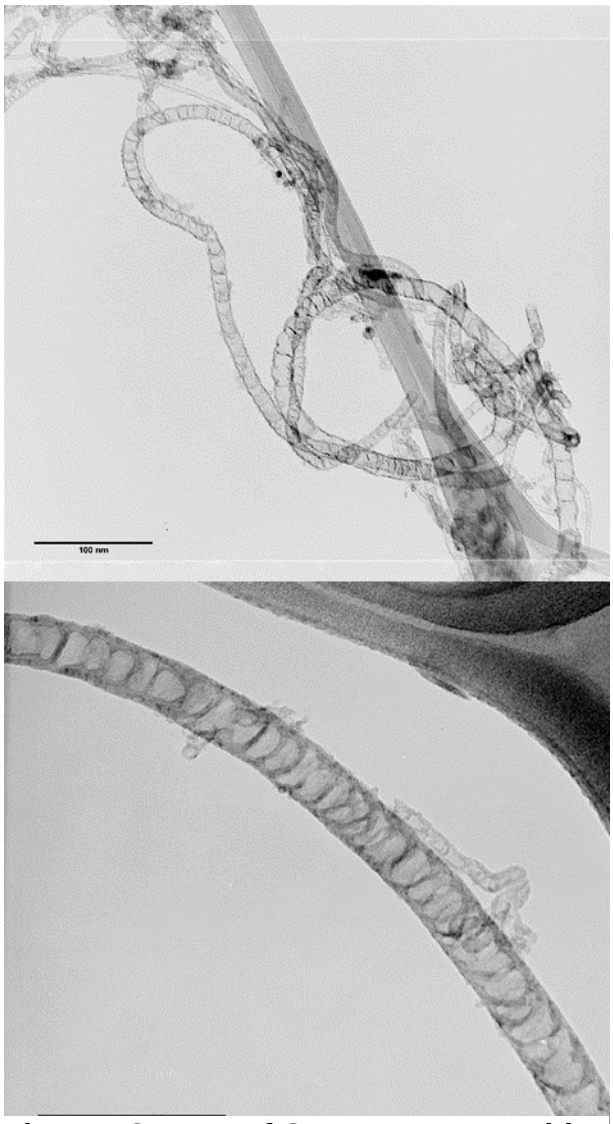

Figure 12: TEM of CNxNTs grown with acetonitrile on vermiculite support. The nanotubes exhibit a heavy herringbone structure indicating nitrogen doping has occurred during growth.

NO_2 were formed from burning of the nanotube, not desorption of nitric oxides on the surface. Using the MS area to determine the relative abundance of CO_2 to NO and NO_2, the amount of nitrogen can be calculated as 0.68 wt%. This is likely below the true value as a portion of the nitrogen will be given off as N_2, which is not possible to differentiate from the N_2 in the air supply. The presence of NO and NO_2 are conclusive proof of nitrogen doping in the nanotube, as neither was seen in a blank run or runs with non-nitrogen doped nanotubes, indicating the nitrogen came from nitrogen species contained in the nanotube. TGA results can be seen in Figure 13.

Identification of the exact nitrogen species is not possible without XPS, however a rough idea can be obtained from results in the literature. Several groups have shown that nitrogen doped tubes grown with CVD using acetonitrile as a feedstock will produce pyridine groups. If the nanotubes have sufficient number of basic groups, a difference should be seen in the point of

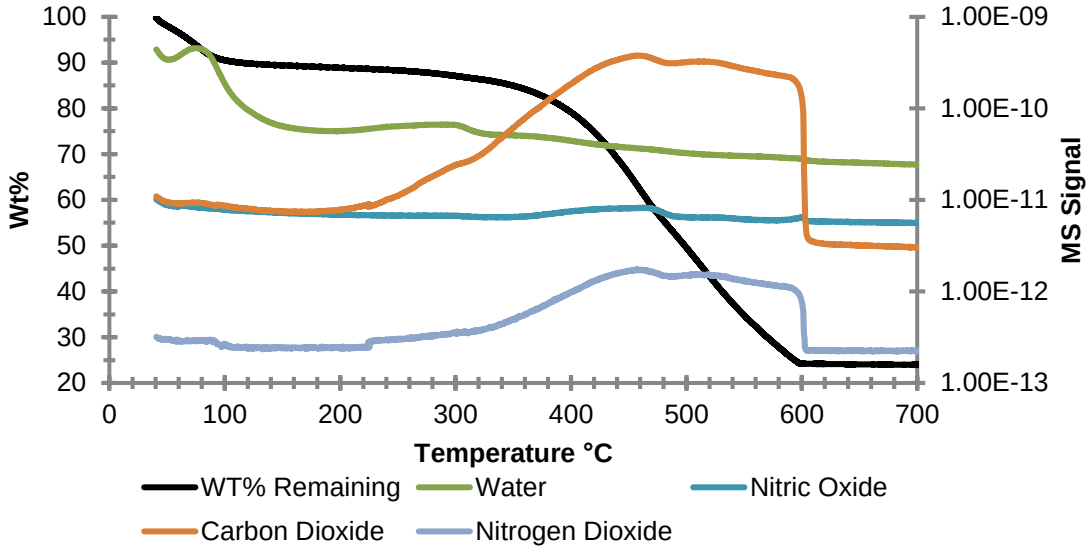

Figure 13:TGA of CNxNTs in air and mass spectrum showing NO and NO2 being formed at the time the nanotube burns

zero charge of the nanotubes. All MWCNTs have some number of carboxylic groups on the surface, which will lead to the point of zero charge being slightly acidic[86].

If the CN_xNTs are measured and found to be more basic than pristine CNTs, it can be assumed the nanotubes will contain pyridinic nitrogen on the surface, similar to what is found in literature[86] and previously discussed. Figure 14 shows the zeta potential measurements, with the pristine nanotubes having a point of zero charge that is slightly acidic, and the nitrogen doped nanotubes have a PZC that is slightly basic. This indicates the nanotubes grown should be similar to those Bulusheva produced which have pyridinic and pyrrolic nitrogen on the surface.

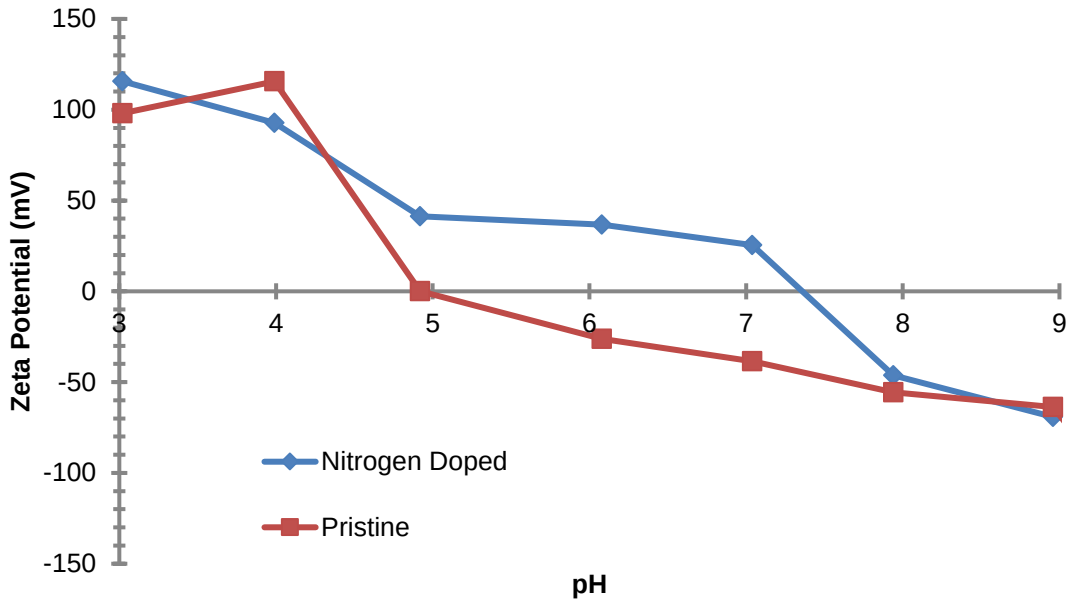

Figure 14: Zeta potential measurements for CNTs and CNxNTs demonstrating basic groups on the surface of the CNxNTs. 0.5 mg/L nanotube concentration using NaOH and HCl to control concentration

Raman spectroscopy is often used to analyze nanotubes[87-89] The D band shift occurring around 1350 cm^{-1} is the result of sp^3 hybridized carbon, which for a nanotube can be considered a defect. The G band shift, 1580 cm^{-1}, is the result of sp^2 hybridized carbon, which would correspond to the crystalline structure in an ideal nanotube. The ratio of intensities of the D/G band then gives a method for measuring the relative amounts of sp^3/sp^2 carbon in a sample, or what fraction of the nanotube contains defects in the lattice structure. The G band is actually made of several peaks, the G^+ which is based on vibrations along the nanotube axis and the G^- which is associated with vibrations of carbon atoms along the circumference of a nanotube[90]. The G^+ peak is at slightly higher wave numbers and its position can be changed by dopants in the carbon lattice, with upshifts for electron acceptors and downshifts for donors[90]. It has been seen in literature for the G^+ peak to be upshifted sufficiently to appear as a shoulder on the main G peak due to

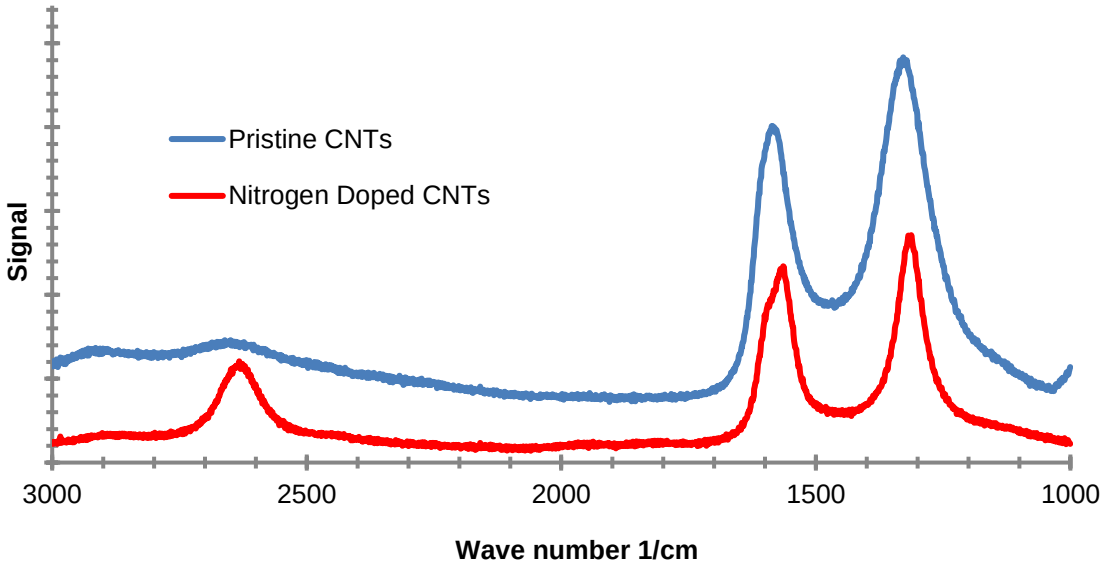

Figure 15: Raman spectroscopy of pristine and nitrogen doped carbon nanotubes. Both samples were in forests on a silicon wafer without any purification to remove amorphous carbon.

nitrogen doping[73,91], though in in samples with a sufficiently thin G band it can be seen with lower concentrations of nitrogen doping[92]. A final peak at 2650-2700 cm^{-1} is known by a variety of names but will be called the G' for this work and arises from a 2-phonon process[90].

The Raman spectra for a forest of CN_xNTs and pristine CNTs can be seen in Figure 15. The I_D/I_G peak ratios for pristine and nitrogen doped nanotubes were 1.20 and 1.15 respectively, indicating a large amount of sp^3 carbon relative to the nanotubes' ideal sp^2 carbon. As a point of reference, reports of I_D/I_G ratios as little at 0.3[87] and up to 1.3[88] occur in the literature for multiwalled carbon nanotubes after purification. It is expected for nitrogen doped nanotubes to have larger amounts of disorder[73], and therefore a worse intensity ratio than a pristine nanotube but this is not the case. The discrepancy then where the pristine nanotubes show higher disorder ratios may be due to the increased concentration of reactant gasses during the pristine growth. Ethylene is known to thermally form coke at growth conditions and may be leading to an excess of sp^3 hybridized carbon on the surface of the nanotube, while not actually being related to the defects in the nanotube. As mentioned before the presence of a peak at 1610 cm^{-1}, or in the case of a broad g band peak a shoulder, is indicative of a dopant[90-92], which is present on in the nanotubes grown with acetonitrile, which then proves the nanotubes are nitrogen doped.

If the surface of the nanotube does contain pyridine, then nitrogen doped nanotubes should have a larger binding affinity for an acid. To this end samples

of pristine and nitrogen doped nanotubes were placed in a TGA at 100°C under constant argon flow. Argon was bubbled through acetic acid and pulsed into the TGA to adsorb on the sample every 20 minutes until the TGA signal indicated a maximum loading. This process likely occurred in the physisorption rage, so the sample was allowed to equilibrate for 24 hours at which point a constant mass was obtained, <0.01 wt%/hour variance. Additionally, DSC was performed to measure the heat of adsorption. It can be assumed more acetic acid adsorbed on the surface, the more likely physisorption is to occur, so only the energy of adsorption for the first peak will be reported. Nanotubes were pretreated to 800°C in argon for 1 hour to remove amorphous carbon and decompose any carboxylic groups on the surface.

The final weight increase of the nitrogen doped nanotubes was 0.68 wt%, while the pristine nanotubes increased 0.49 wt%, showing a 39% increase in the retention of acetic acid on the nitrogen doped nanotubes. The heat of adsorption for the first pulse was found to be 9 times larger for the CN_xNTs than the CNTs, 551.3 kJ/mol and 61.9 kJ/mol respectively, indicating there may be reaction occurring, not just an adsorption step. It is possible but unlikely that amorphous carbon is coating the nanotube with carboxylic groups which would significantly skew the energy of adsorption. This adsorption study proves that adsorption of acids is preferential to the nitrogen doped nanotubes, which may lead to a semi selective functionalization route.

Conclusions

Nitrogen can be incorporated into a nanotube in several different ways and will change the properties of the nanotubes based on the chemical structure of the nitrogen groups. Literature suggests that the nanotubes grown over iron catalysts using either pure or dilute acetonitrile as a feedstock should produce pyridine rings (sp^2 hybridized) and graphitic nitrogen (sp^3 hybridized), with a higher concentration of pyridinic nitrogen on the outer wall of the nanotube. These act as p and n type dopants respectively, which can be used for further functionalization. TEM images suggest nitrogen doping is likely to have occurred, while Raman spectroscopy and TGA both confirm the presence of nitrogen incorporated into the nanotube structure. Zeta potential measurements have shown it may be the basic pyridine rings. XPS measurements will need to be performed to prove this theory.

Chapter 4: Selective Functionalization

Introduction

The purpose of this work is to create a nanotube with two different surface chemistries such that it may be thermodynamically favorable to bridge a polymer-polymer interface. The moiety that will most likely make a nanotube's surface chemistry compatible with a particular polymer is attaching the same polymer. To that end there are two methods well described in the literature regarding covalent bonding of a polymer to a nanotube, the grafting to and grafting from approach. Grafting to is the case in which a polymer strand already exists, normally with a selective functionality at the end, which can then be attached to the nanotube wall. Grafting from requires a functionality on the nanotube to allow the initiation of a polymer growth, and the strand in grown on the nanotube one monomer at a time. Both will be reviewed and were attempted.

Polymer-Grafting To

Prior to grafting a polymer to a nanotube sidewall, a functional group must be placed on the wall to facilitate a covalent bond since both single and multiwalled carbon nanotubes are generally considered stable and inert as hexagonal carbon rings are unreactive. This stability also leads to sidewall reactions requiring extreme conditions or reagents to achieve functionalization. Two methods of functionalization generally are performed on a nanotube to allow for further functionalization: oxidation of the nanotube leading to surface carboxylic groups, and direct addition of strong reagents to the nanotube wall

such as: nucleophilic carbenes[93], cycloaddition of nitrenes[93], and aryl radicals and cations[94]. All of these are likely too reactive to selectively functionalize one of the blocks. One direct addition method which may be selective is addition of radicals[93,94] such as fluorine.

Defect free nanotubes are considered inert towards fluorine near room temperature, however few nanotubes are truly defect free, and at elevated temperatures, >250°C, fluorination via radical scavenging of the nanotube occurs rapidly[79,93,95-97]. It has been proven that between 250°C-400°C, functionalization occurs, while above 400°C destruction of a single wall nanotube occurs[95]. When functionalization occurs within the appropriate temperature range, it is reversible upon treatment with hydrazine. Raman was used to demonstrate the nanotube structure before fluorination and after defluorination were identical. This suggests the possibility that the fluorine has not chemically modified the surface of the nanotube. The use of Fourier transform infrared spectroscopy, FTIR,[93] and TEM EELS[98] prove the fluorine does chemically bind to a nanotube with both covalent and ionic bonds. This suggests that further functionalization can be performed from the fluorine on the nanotube surface via reaction with a nucleophilic reagent such as alcohols, amines, Grignard reagents, and alkyl lithium compounds[93,97]. Fluorination has also been achieved at room temperature using BF_3 as the fluorinating agent for both pristine[99] and nitrogen doped[79] nanotubes, indicating selectivity for nitrogen doped nanotubes may not be possible for block functionalization. Additionally, fluorine is highly reactive and is considered dangerous, so for the

purpose of this work will not be attempted. Further radical functionalization will be discussed in the grafting from section of this chapter.

Oxidation of nanotubes is perhaps the most common route to functionalization and does not require prohibitively expensive or dangerous chemicals to form carboxylic acids on the surface, a species which naturally occurs in MWCNTs in low concentrations. Polymers terminated with hydroxyl or amino group have been used to undergo esterification or amidation reactions with the carboxylic groups on the nanotube to achieve functionalization[93,94,100,101]. Typically, the oxidized nanotubes are rinsed with a weak acid to ensure the carboxylic groups are in the protonated form, then refluxed with thionyl chloride for a period of hours to form an acryl chloride which then undergoes either the esterification or amidation reaction[93,94,100-104], which can be seen in Figure 16.

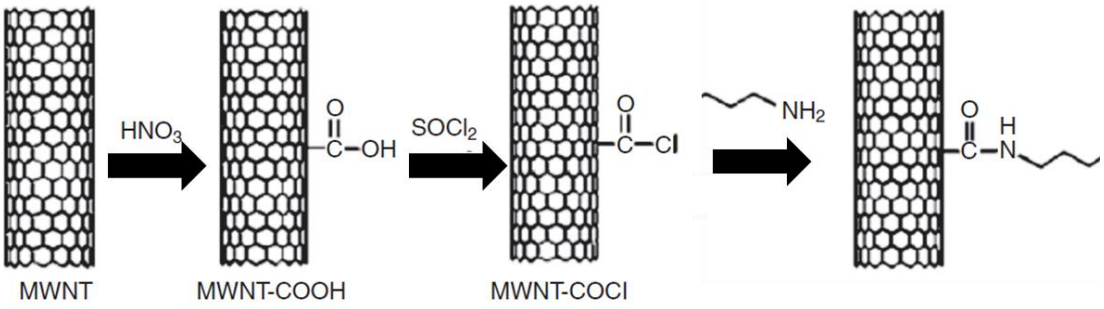

Figure 16: Reaction mechanism for sequential oxidation/ amidation reaction on a carbon nanotube.

Oxidation can occur thermally in air[105] or through the use of an oxidizing agent such as nitric acid, sulfuric acid, or hydrogen peroxide, or a mixture[5,47,105,106]. Of these, nitric acid attack is the most commonly found in literature, though a mixture of nitric and sulfuric acid has been shown to be the

most effective[105]. Interestingly flashing in air provided almost as many carboxylic groups as acid treatment, leading validity to the possibility of a 'green' treatment[105]. Work on single walled nanotubes by Miyata et. al. showed that hydrogen peroxide would act on both metallic and semiconducting nanotubes but would act faster on the semiconducting nanotubes[107]. They attributed this to the p-type doping of the nanotube by the carboxylic groups initially added by the H_2O_2 would raise the density of states for the semiconducting nanotubes above the fermi level, which induces a higher reactivity for further oxidation[107].

Nitrogen doped nanotubes can also be p-type doped, which could lead to the CN_xNTs to have a higher rate of oxidation than pristine nanotubes initially, leading to a possible block functionalization route. Indeed literature shows that the decomposition of H_2O_2 occurs more quickly on nitrogen doped nanotubes as opposed to pristine nanotubes[108] however these nanotubes were nitrogen doped post growth and contained primary rather than secondary amines. Voitko et. al. went on to measure the activation energy of H_2O_2 decomposition experimentally and theoretically and found in both cases the nitrogen containing nanotubes were lower than pristine or oxidized nanotubes, 18.9 kJ/mol, 23.9 kJ/mol, and 26.8 kJ/mol respectively. In this case decomposition refers to radical OH production, which should have the potential to oxidize the nanotube. These results indicate however the more the nanotube is oxidized the slower the reaction will be, leading to a self-poisoning reaction. If oxidation is selective,

acylation and amidation can be achieved following established protocol for grafting a polymer to a nanotube.[93,94,100]

Polymer-Grafting From

Grafting from relies on the proper placement of initiator groups for covalently anchoring the monomers to the nanotubes. The concentration of the initiator groups will determine the number of possible functionalization sites on the nanotube, as well as the rate of initiation for the polymerization reaction. As such, we can assume that if an initiator attaches selectively to a nitrogen doped nanotube and not to a pristine nanotube, polymerization will be selective. Alternatively, if adsorption isn't selective the p-type doping caused by the pyridine rings on the nanotube surface will cause easier desorption of a radical, as it will be more difficult for an already p-doped nanotube to donate an electron to form a bond with the radical.

One grafting from method is anionic-initiated polymerization, in which a carbanion is introduced on the nanotube surface by treatment with an anionic initiator dispersed in the desired monomer unit[109]. Anionic-initiated

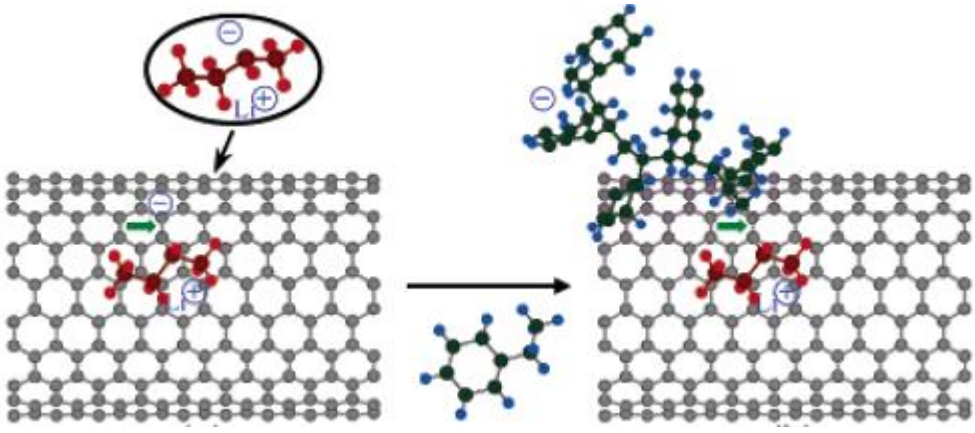

Figure 17: Anionic grafting of styrene monomers to a nanotube surface as performed by Viswanathan et. al.

polymerization can be achieved in a single step and is useful for a low level of functionalization in a single step, and seen in Figure 17[109]. Anionic-initiated polymerization has the added benefit of negatively charging the nanotube surface, which aids in overcoming the π-π stacking that causes agglomeration of nanotubes allowing them to be more easily dispersed during polymerization[109]. This reaction is known to occur on pristine nanotubes[109] however and is therefore unlikely to be selective, although it is possible the negative charge from the anionic imitator will exhibit selective adsorption.

One of the more useful techniques for grafting a polymer onto a nanotube from the monomer units is a controlled radical polymerization[104,110-113], also known as living radical polymerization. CRP is a form of polymerization which is frequently terminated in a reversible manner by a mediator group preventing other species from interfering with the polymerization and causing an irreversible termination step. CRP allows for a low level of impurities in the system, which is advantageous for nanotubes which often have residual catalysts particles or amorphous carbon attached[110]. Several groups have reported grafting from reactions using Atomic Transfer Radical Polymerization, a type of CRP, using bromine as the mediating group[94,100,104,110,114]. The bromine, which acts as both an initiator and mediator, is placed on the surface through various reactions with an acyl chloride, formed from reacting the carboxylic groups with thionyl chloride, as discussed above. A similar reaction, known as Nitroxide Mediated Radical Polymerization, NMRP, was performed using 2, 2, 6, 6-tetramethyl-1-piperidnyloxyl, TEMPO, as the mediator

group[112,113,115]. The NMRP reaction requires acyl groups on the surface to act as the initiator.

A second method for NMRP was discovered by Terrones et. al. They used the radical scavenging tendencies of CNTs to trap a benzoyl peroxide, BPO, radical on the surface. This radical is stable, and is used to trap the mediator TEMPO without a carboxylic group on the surface[111,115]. The TEMPO molecule can then desorb in the presence of styrene and allow the residual radical on the CNT from BPO to initiate polymerization, which allows the TEMPO to rebind to the now covalently bonded styrene and act as the mediator. A mechanism can be seen in Figure 17. This mechanism shows extreme promise for selectivity to nitrogen doped nanotubes and will be explored further.

Non-covalent Bonding

One non-covalent method was tried as a follow up to the adsorption of acetic acid on pyridine rings. As it was proved in Chapter 3 the CN_xNTs were capable of showing preferential adsorption, it may be possible to preferentially adsorb larger acids, potentially even polymer selectively. If that is the case, a few carboxylic acid groups could adsorb to the basic pyridine sites leaving the remainder of the carboxylic acids for potential functionalization, treating the polyacrylic acid, PAA, as an anchor binding the desired polymer to the nanotube through its selective adsorption.

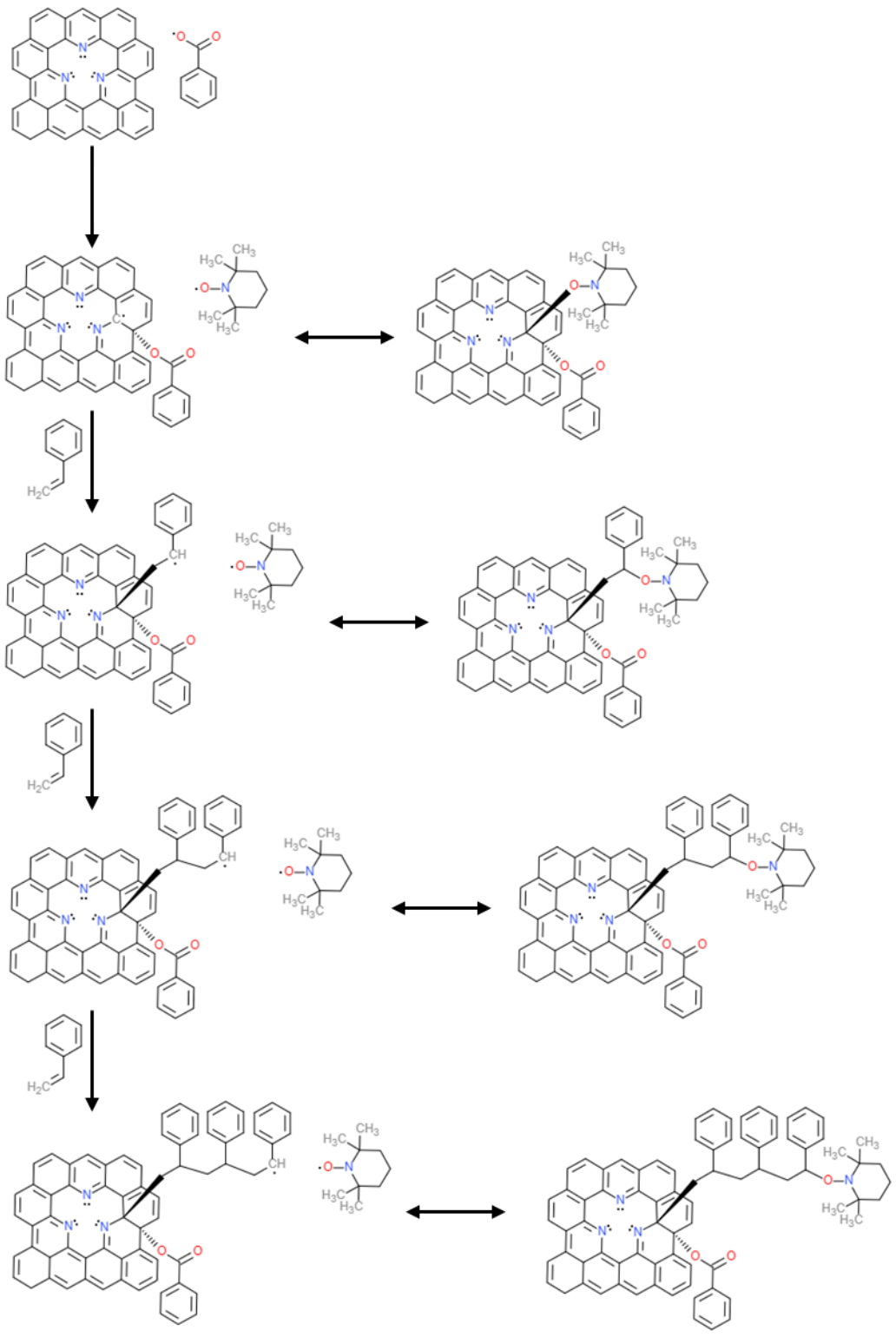

Figure 18:NMRP of styrene on a segment of nitrogen doped carbon nanotube. Note the polymer doesn't attach to the nitrogen group, but rather to a carbon near the nitrogen group.

Experimental

All chemicals were purchased from Sigma Aldrich and were of reagent grade, >98%, or higher. All gasses were ultra-high purity, or in the case of air grade zero, and were purchased form Airgas. Nanotubes were synthesized as described in Chapter 2, either on silicon wafer supports or on vermiculite support and purified. In cases where only pristine or only nitrogen doped nanotubes were used, they were grown to ½ the height of the block nanotube forests.

Selective Adsorption

To test the selectivity of the adsorption pure nitrogen doped nanotubes and pure non-nitrogen doped nanotubes were used, block tubes were not attempted with this method. Polyacrylic acid, MW 450,000 (Sigma #181285), and polyacrylic acid partial potassium salt (Sigma #435325), were used as the polymer. HCl and NaOH were used to control the pH of the nanotube, polymer solution. Nanopure water from an inhouse purification system was used as the solvent in all cases. The polymer to nanotube weight ratio was 0.5, and the nanotube concentration in solution was 0.2 g/L. Attachment of polymer to the nanotube was tested in 3 ways, by dispersion of the hydrophobic nanotubes in water after time periods of 5 minutes and 1 week to test for stability of the system, by visual observation of polymer under TEM, and by TGA in argon of the filtered sample.

Selective Oxidation

Block functionalized nanotubes were used because naturally occurring carboxylic groups at the ends of the nanotube might prevent identification of true selectivity. For this same reason nanotubes grown and functionalized on the silicon wafers were used rather than those purified after growth on vermiculite and were stored under an inert environment except during the actual oxidation process.

Four oxidation levels were tested, dilute nitric acid reflux for 1 hour, oxidation in air at 375°C for 15 minutes and oxidation at 500°C for 5 minutes, and oxidation in hydrogen peroxide. Air oxidation was carried out in a horizontal quartz tube reactor with 200 sccm grade zero air flow. The gas was passed over two water traps to prevent humidity from effecting the results. The reactor was ramped to temperature under UHP argon at a rate of 10°C/min, at which point the flow was switched to air. After oxidation air flow was ceased and argon flow returned to purge the reactor and prevent oxidation. A fast quench was performed for the sample, reaching room temperature in roughly 5 minutes to prevent continued oxidation, afterwards the sample was stored under nitrogen.

Nitric acid oxidation was performed by first refluxing the 0.1 M nitric acid until a steady temperature had been reached, then adding the nanotubes still on the silicon wafer. The nanotubes were quenched again to prevent further oxidation, this time by dumping to nitric acid solution and nanotubes into cold nanopure water then removal of the silicon wafers from the solution. The nanotubes were placed in a bath of decalin which was gently swirled for 5

minutes to remove any residual water or nitric acid. The nanotube forest was then placed under vacuum and allowed to dry overnight before returning to an inert environment.

Extent of oxidation for the air and nitric acid oxidation was determined with EDX under SEM. First surface carboxylic groups were converted into acyl chlorides by reaction with thionyl chloride for 12 hours at room temperature. The block forests still bound to the silica wafer were washed gently in decalin and dried under vacuum overnight. The wafers were then split in half and examined under EDX to determine if chlorine could be seen selectively or throughout the nanotube forest.

Hydrogen peroxide oxidation was performed on pure CNT and CN_xNTs rather than on block nanotubes in a vertical forest. Oxidation was carried out at room temperature using a 30 wt% H_2O_2 solution for 1 hour. TGA in inert was performed to measure the extend of oxidation. The issue of carboxylic groups on the nanotube was avoided by performing a calibration test with the CNTs of both nitrogen and non-nitrogen doped prior to oxidation.

Nitroxide Mediated Radical Polymerization

Nitroxide mediated radical polymerization was carried out on the pure CNTs and pure CN_xNTs as a comparison. Nanotubes used in this instance differed slightly from those produced by the procedure outlined in Chapter 2. In this case nanotubes were not allowed to dry during the filtration process to percent agglomerates from forming. During the first filtration to remove the excess sodium hydroxide and sodium silicates, the solution was allowed to filter

long enough to reach 100 mL total volume. After this point the nanotubes/MgOH mixture was added to the dilute HCl as described in Chapter 2, without weighing a portion to determine the amount of acid needed to neutralize the MgOH. Instead prior trials of growth and purification were used to see the maximum amount of acid use, and that value was used for all 'wet' trials. The second filtration was accomplished and again the nanotubes were not allowed to dry before being washed first with water, followed by 100 mL of acetone (4 times the volume of the filter funnel used) to ensure all water was removed from the system, followed by 100 mL of benzene. The nanotubes were then stored in benzene until ready for functionalization. All of this was performed to prevent the nanotubes from being dried at any point once purification started, as agglomeration during the drying process is severe.

A 10mL sample of the well dispersed nanotube solution was dried and weighted to determine the concentration of nanotubes in mg/mL of the benzene. This value was used to determine the amount of initiator, mediator, and monomer used in the functionalization attempt. In all cases 1 gram of nanotubes in solution was reacted with 0.1 g BPO. Sufficient solvent, benzene, was used to bring the total volume up to 100 mL to ensure concentration would not affect the rate when comparing CNTs with CN_xNTs. The reaction was allowed to reflux for 1 hour, at which time the mediator group, TEMPO, was added in a 1:1.3 molar ratio in accordance with the paper described by Terrones et. al. [111]. The nanotubes were filtered and washed with 100 mL of benzene to remove unbound radical pairs, but the nanotubes were not allowed

to dry out. They were then diluted to 300 mL benzene and added to 200 mL of styrene and heated to reflux under a condensing column. They were allowed to polymerize for 24 hours followed by washing with 100 mL benzene 3 times to remove unbound polymer, using centrifugation, 1000 RPM for 5 minutes, to remove the nanotubes from solution in between washings, with the supernatant being decanted off. The nanotubes were again stored wet and never allowed to dry to prevent agglomeration of the nanotubes.

A 1 mL sample of the polymerized nanotubes in benzene was diluted until with 25 mL benzene, causing the solution to be clear, sonicated for 5 minutes in a bath sonicator, and dropped onto a lacey carbon coated copper grid, mesh number 300, for TEM analysis. TEM was performed on a Zeiss 10A operating at 80 keV. Sample polymer loading was performed drying out 20 mg of the polymerized nanotubes and performing TGA in argon to decompose the polymer. Prior to the TGA the samples were dried overnight under vacuum at 40°C. The samples were heated from 50°C to 700°C using a ramp rate of 2°C/min under 60 sccm argon. Each type of nanotube, pristine, nitrogen doped, and block nitrogen doped, will have a different number of defects on the surface, therefore each one was compared to a blank run of the same type of nanotube prior to polymerization, but from the same growth batch to determine the true change in weight from decomposing polymer, not other groups on the surface.

Results

Preferential Adsorption

Initial adsorption tests were performed with the polyacrylic acid partial potassium salt, KPAA at a pH of 6.7. The starting pH was determined by the zeta potential measurements discussed in Chapter 3, with an initial pH being chosen such that the pristine nanotubes have a point of zero charge, PZC below the solution pH, meaning a negatively charged surface, and the nitrogen doped nanotubes have a PZC above the solution pH, meaning a positively charge surface. This could cause the partial salt polymer, which will have anion groups attached when the potassium dissociates in water, to be attached to the nitrogen doped nanotube, even if it doesn't undergo a selective adsorption at the pyridine site. Figure 19 shows images of the polymer coating the nanotubes after 5 minutes of stirring followed by 5 minutes of settling. The nanotubes were still dispersed after 1 week being stationary, indicating the polymer on the nitrogen doped nanotubes was strongly bound to the surface.

If the system of adsorption is as theorized, then adding an acid should titrate the basic pyridine rings on the nitrogen doped nanotubes and cause the release of the polymer. Alternatively if acid-base pairing is not causing the adsorption and selective dispersion, then adding an acid should do one of two things. Either the acid will titrate the anion groups of the partial salt polymer and release the polymer from the nitrogen doped side as it is no longer attracted to the positive surface of the CN_xNT, or acid will drop the pH low enough to allow

Figure 19: Pristine and Nitrogen doped nanotubes dispersed in water with polyacrylic acid after five minutes (Left) and 1 week (Right) showing stability of the system.

the pristine nanotubes to appear positively charged and allow dispersion of the pristine nanotubes in solution.

When HCl was added the CN_xNTs promptly dropped out of solution, indicating it may have been selective adsorption of the carboxylic acids on the basic pyridine sites, or titration of the anion polymer groups. To further test the theory the pH of the same solution was returned to 6.7 with NaOH to determine if the system was reversibly responsive with regards to pH. At the same pH there should be similar numbers of basic pyridine groups and acidic carboxylic acid groups regardless if the pH was temporarily lowered or not. When the pH was again raised to 6.7 the CN_xNTs did not disperse.

To further probe the adsorption mechanism the pH of a fresh sample was increase from 6.7 (where selective dispersion occurred) to 13, at which point both pristine and nitrogen doped nanotubes will be above the PZC, so the anions of the polymer should be released. This procedure was also attempted with PAA, which would not have anions present form the partial salt and should

then bind to both nitrogen doped and pristine nanotubes at the elevated pH, but be reversed in the selectivity of the pH 6.7 case. At neutral pH, both pristine and nitrogen doped nanotubes were dispersed, indicating adsorption on both. At high pH, the KPAA desorbed from both nanotube samples indicating a release of the anion groups from the surface, however the PAA showed the same behavior. It is possible the NaOH titrated all acid groups on the PAA leaving only anions which would then desorb from the negatively charged surface, but this wouldn't explain the PAA dispersing the CN_xNTs at neutral pH.

Nanotubes were filtered out of solution, sonicated in decalin and analyzed under TEM. At pH 1.5 and 6.7 nanotubes were coated in polymer in all cases, while no case at pH of 13 had polymer. Examples of these can be seen in Figure 20 suggesting that dispersion of the nanotubes is independent of adsorption of polymer, as no nanotubes were dispersed at low pH despite

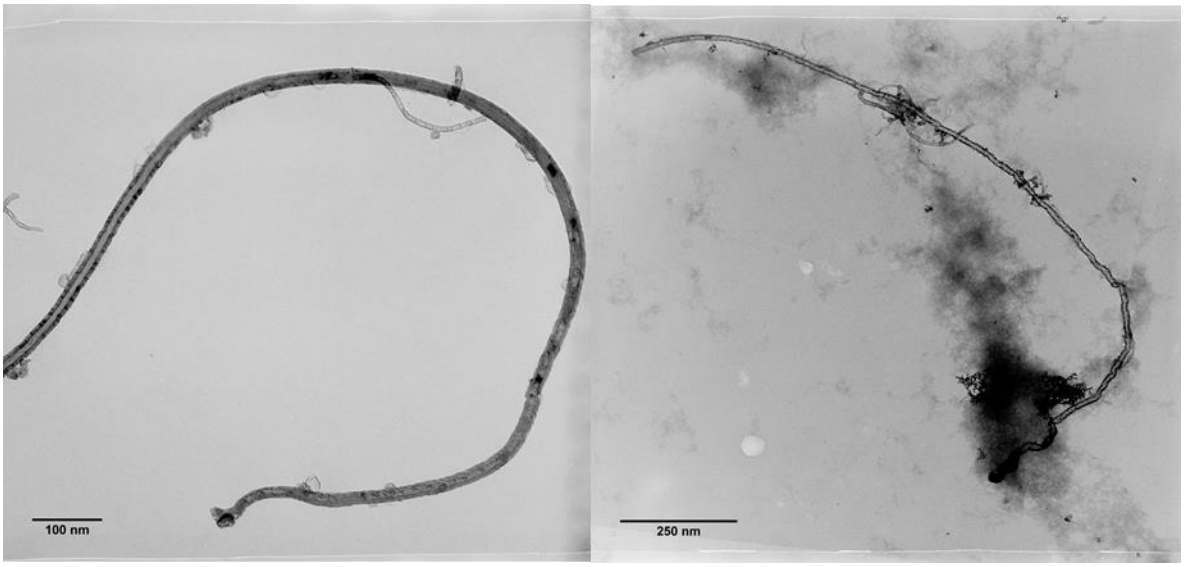

Figure 20: TEM images showing Left- Pristine nanotubes with no polymer at a pH of 13 and Right- Pristine nanotubes with KPAA polymer at a pH of 6.7, indicating polymer is present presence and dispersion are not related.

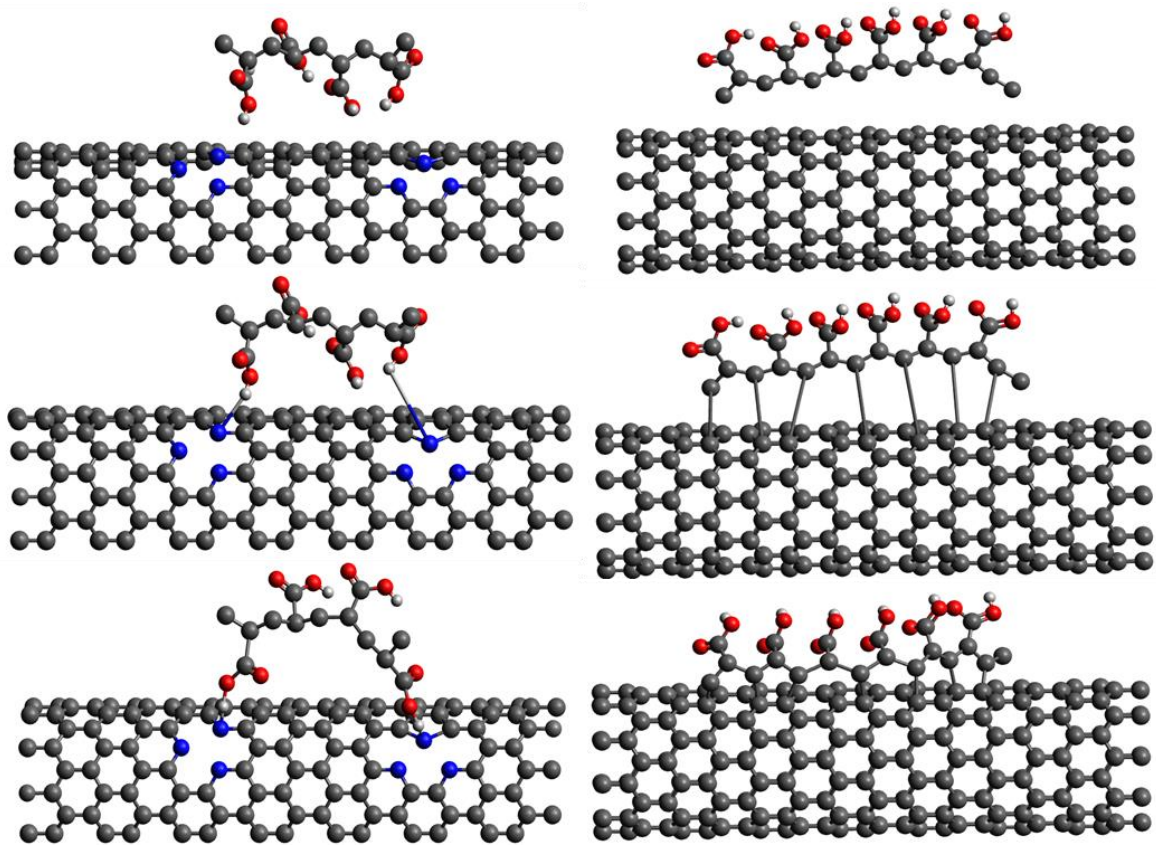

Figure 21: Diagram of PAA adsorption on CNT Left -Idealized adsorption method where carboxylic groups attach to basic pyridine groups Right- Likely actual adsorption with the hydrophobic backbone of the polymer adhering to the hydrophobic nanotube

having polymer present. Adsorption of the polymer is therefore necessary for dispersion but not sufficient.

Several reports in literature[116-118] have concluded that polymers will adsorb on unfunctionalized nanotubes, with the hydrophobic backbone of the polymer attached to the hydrophobic nanotube surface. A visual depicting this adsorption method can be seen in Figure 21, along with the selective adsorption method theorized previously.

If this backbone adsorption method is correct, the pH could act upon the exposed carboxylic acid groups. Under acid conditions the carboxylic acids should be fully protonated and able to undergo hydrogen bonding with itself,

causing the polymer to coil up[119] and pull the nanotubes with it, causing agglomeration due to the polymer hydrogen bonding. When in the deprotonated state the polymer forms a rod like structure, with the charged conjugate bases repelling each other[119], desorbing from the negatively charge nanotube surface. This allows the nanotubes to fall out of solution, but not truly agglomerate. At the neutral pH, there is a balance in the number of protonated and unprotonated carboxylic groups, based on the number of acid carboxylic acids in the polymer to start with and acidic/ basic groups on the nanotube. In both PAA and KPAA with CN_xNTs, nanotubes were well dispersed, indicating the system is near the pKa for the polymer and there is a balance between attractive hydrogen bonding and the repulsive forces of the anions, so the nanotubes are dispersible in water. In the case of KPAA, the polymer may be more prone to undergo hydrogen bonding induced coiling based on the molecular weight causing differences in the rigidity of the carbon backbone[119] allowing the pristine nanotubes to undergo hydrogen bonding and crash out of solution while coated. The nitrogen doped nanotube's basic sites could titrate some of the carboxylic acids on the polymer, shifting the forces more towards the balance point where polymer self hydrogen bonding doesn't occur. The dispersion of all cases and a illustration of the polymer wrapped nanotubes behavior can be seen in Figure 22. Polymer wrapping tests will not be continued, because it is unlikely any functional group will be energetically

favorable to adhere to the basic sites of the nitrogen doped nanotube over the adsorption of the hydrophobic backbone of the polymer onto the nanotube.

	pH=1.5	pH=6.7	pH=13
CN_xNT with KPAA	No	Yes	No
CNT with KPAA	No	No	No
CN_xNT with PAA	No	Yes	No
CNT with PAA	No	Yes	No

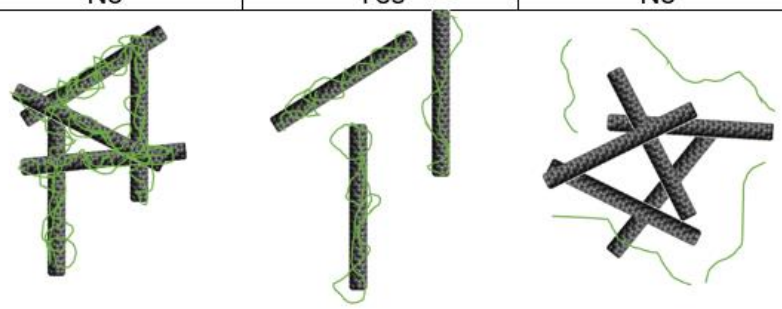

Figure 22: Dispersion results of CNTS in water with KPAA and PAA showing polymer wrapping of the nanotube with hydrogen bonding between the carboxylic groups at low pH, anion repulsion of the deprotonated polymer in the high pH region.

Selective Oxidation

Selective oxidation trials with nitric acid and air on block functionalized CNTs. Thionyl chloride treatment was used to form acyl groups from the carboxylic acids and SEM with EDX was used to determine the selectivity of the oxidation attack. Images with the elemental mapping overlay can be seen in figures 23-26, chlorine is tagged in red in all cases.

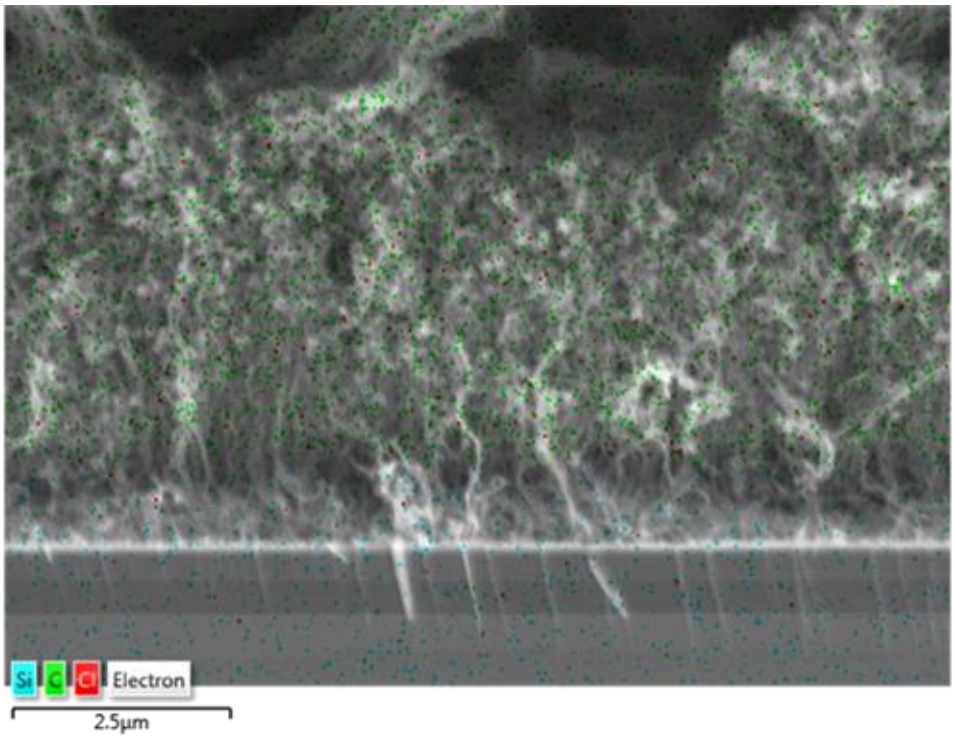

Figure 24: SEM image with EDX overlay of block CNTs grown on a silicon wafer. Nanotubes were oxidized in air at 350°C and the carboxylic groups were tagged with chlorine via reaction with thionyl chloride

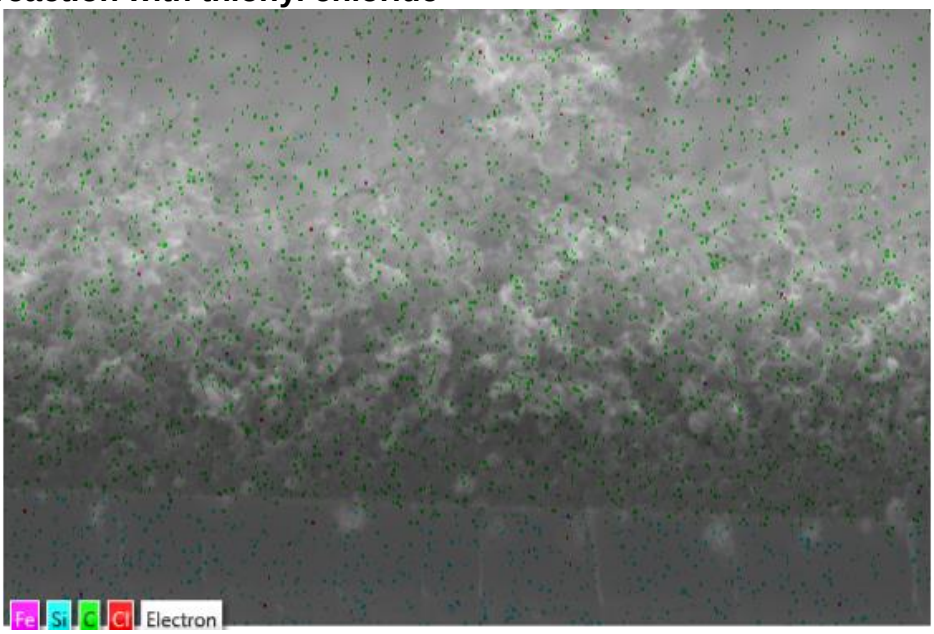

Figure 23: SEM image with EDX overlay of block CNTs grown on a silicon wafer. Nanotubes were oxidized in air at 500°C and the carboxylic groups were tagged with chlorine via reaction with thionyl chloride.

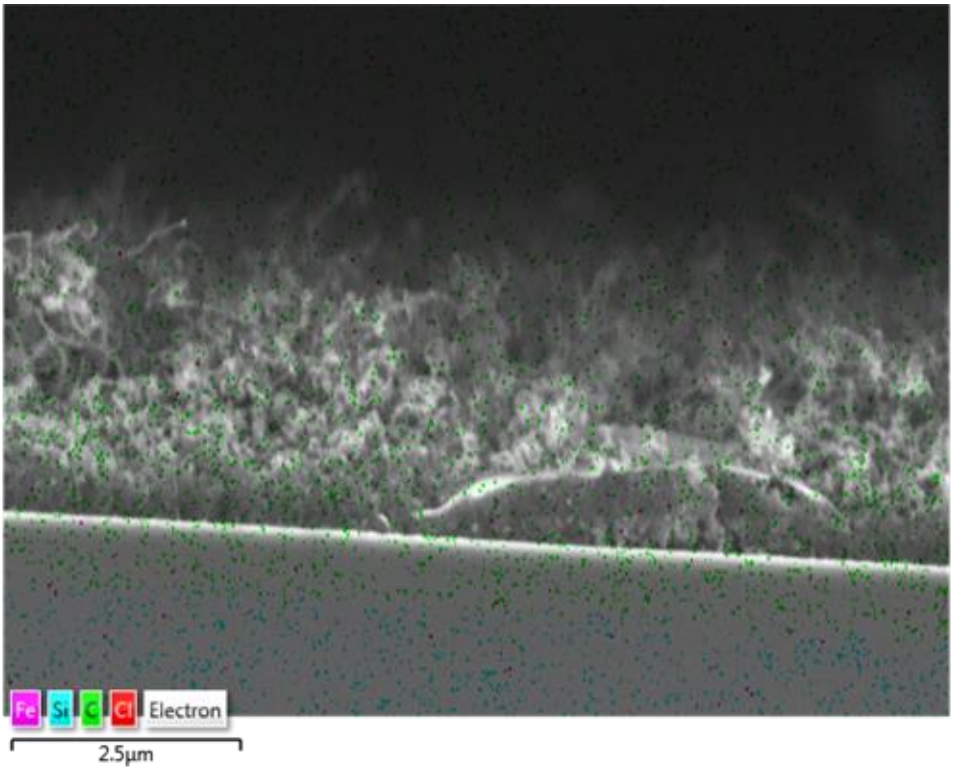

Figure 26: SEM image with EDX overlay of block CNTs grown on a silicon wafer. Nanotubes were oxidized refluxing nitric acid and the carboxylic groups were tagged with chlorine via reaction with thionyl chloride.

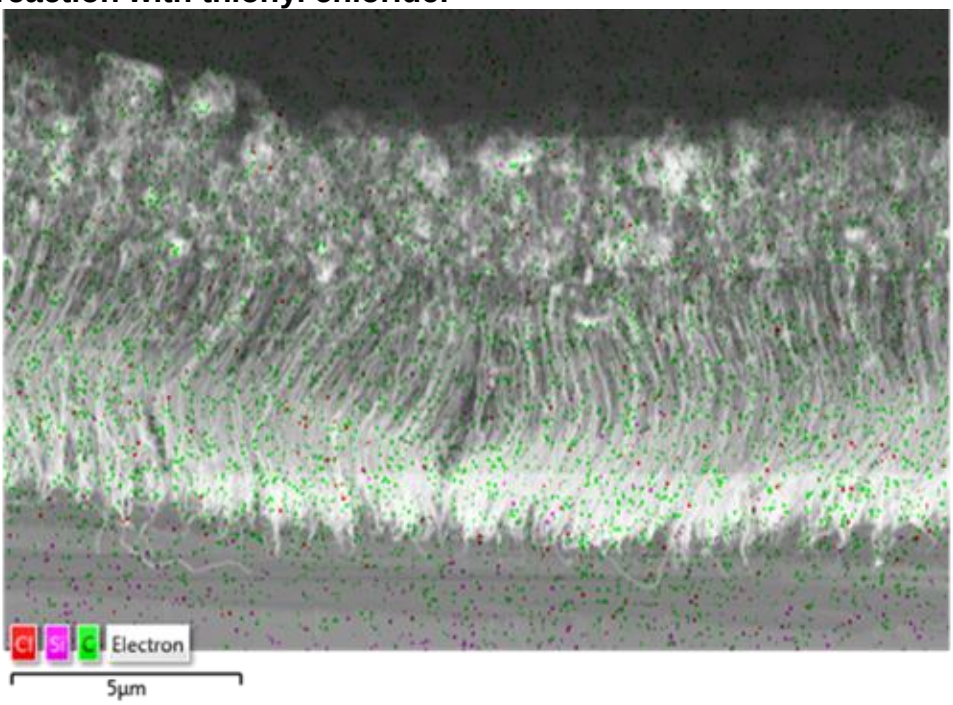

Figure 25: SEM image with EDX overlay of block CNTs grown on a silicon wafer. Nanotubes were not oxidized and the naturally occurring carboxylic groups were tagged with chlorine via reaction with thionyl chloride.

In all oxidation cases some amount of chlorine is identified, however it was not spatially selective to either the top or bottom of the forests. The amount of chlorine found was less than 0.1 atom % in all cases. A similar amount was found in a forest of nanotubes that was given the same thionyl chloride treatment without a prior oxidation step indicating chlorine tagged with EDX is likely on naturally occurring carboxylic groups that form on the defects of all multiwalled carbon nanotubes.

This method of testing for oxidation seems to have several flaws. First it appears the vertical alignment of the forest is mostly destroyed during the oxidation process. All 4 samples, (2 air oxidized, 1 acid oxidized, and 1 unoxidized) were grown at the same time in the same batch and all showed vertical alignment prior to treatment. Only the unoxidized tubes retained their alignment after the treatment, with the nitric acid treated nanotube showing the most damage. One obvious explanation is the forces from drying the nanotubes after each treatment. The acid treated nanotubes were wetted and dried twice, once for oxidation and once for the thionyl chloride treatment. Perhaps the unoxidized case had enough amorphous carbon on the surface help support the rigidity of the nanotube, but that seems unlikely as the strength of the nanotube should far outweigh any strength of the amorphous carbon. Both chlorine and carbon were tagged in locations where neither should exist from the image, above the forest in empty space as well as below the forest in the silicon wafer, caused by the large interaction volume of the beam with the sample. In general, the X-rays come from at most 5 microns deep in the

sample. As the forest is mostly empty space between nanotubes this distance can be significantly increased. While the beam is moving in its rastering pattern, it is possible for the beam to be at one point, while the xrays produced come from a much larger interaction volume, leading to an EDX resolution worse than SEM. The detector then assumes the x-ray came from the current point, and resolution is lost. It is possible the oxidation is selective but with the destruction of the forest and the resolution of the system this method was unable to identify it as selective. The TGA results in Chapter 2, Figure 7 and Chapter 3, Figure 12 both show at 500°C severe decomposition of the nanotube will occur, however literature suggests nanotubes can withstand this temperature in air for a short time but are oxidized during that time[105]. The lack of oxidation measured is then likely due to the method rather than an actual lack of oxidation, as both literature and TGA results indicate oxidation should have occurred.

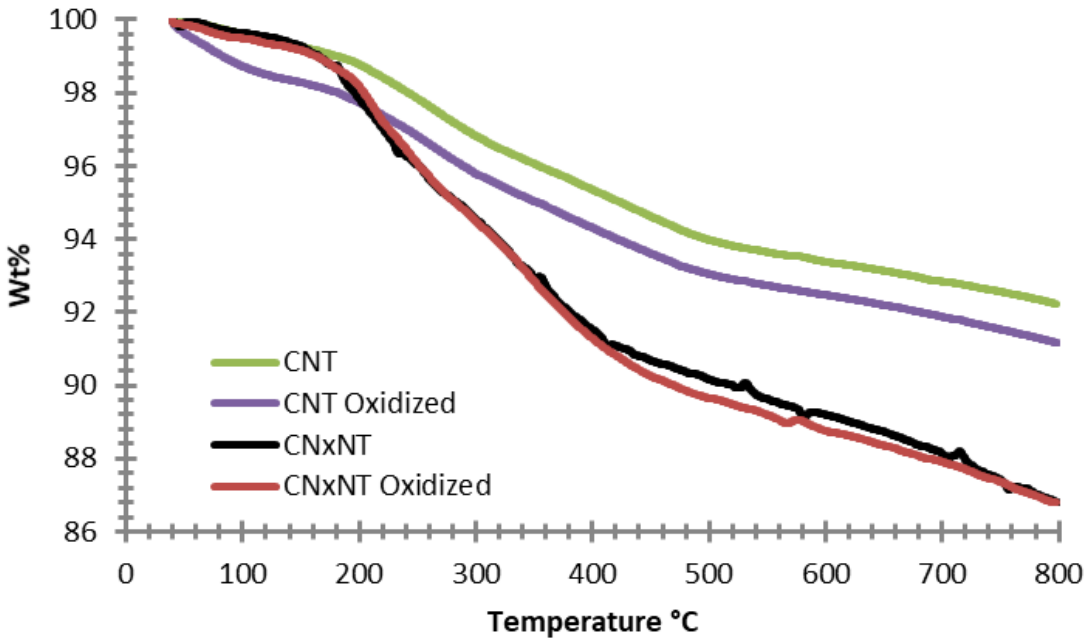

Figure 27: TGA in argon of pristine and nitrogen doped nanotubes before and after oxidation by hydrogen peroxide. A ramp rate of 2°C/min was used with 60 sccm Ar flowing.

For these reasons it was determined that the testing of the hydrogen peroxide oxidation should be performed in a different manner. TGA in argon was used, effectively a TPD, to measure the carboxylic groups by weight. Measurements were taken before and after oxidation to compare the extent of oxidation and can be seen in Figure 27. The decomposition reaction of hydrogen peroxide was vigorous for the nitrogen doped nanotubes, and nearly unobservable with the eye in the case of pristine nanotubes, though a small amount of gas and heat production was observed, indicating there was a significant difference in the reaction between the two types of nanotubes. TGA showed a difference in carboxylic groups on the surface between the pristine and nitrogen doped nanotubes, but no significant differences before and after oxidation. A slight difference in spectra can be seen in the pristine case; however, the difference occurs initially below 100°C, indicating is it water desorbing rather than a desorbed carboxylic acid group which occur at higher temperatures.

After the visible reaction had ceased, the nanotubes were filtered out of solution and reacted a second time with hydrogen peroxide. The CN_xNTs reacted equally vigorously the second time, and no visible reaction occurred on the pristine nanotubes. This was repeated a total of 5 times, and at all times the nitrogen doped nanotubes continued to act vigorously initially until the hydrogen peroxide ran out. This coupled with the fact TGA didn't detect further oxidation of the nanotube indicates the nanotubes may be acting catalytically rather than being oxidized. CNTs are natural radical scavengers[7] and as such will allow the

hydrogen peroxide to dissociate into its H^*, OH^*, and OOH^* radicals on the surface. The nitrogen doping in the CN_xNTs acts as a p-type dopant, which results in a weaker bond. If the nanotubes are on the right side of a volcano plot for the hydrogen peroxide decomposition reaction, a weakening of the nanotube-radical bond would allow the nitrogen doped nanotubes to be more catalytically active, which would explain the difference in reactivity of the nanotubes with the peroxide. The stronger binding of the OH^* and OOH^* radicals on the pristine nanotube would lead to the radicals staying on the surface longer, or potentially forming carboxylic groups, which would explain the literature results of oxidizing[107,108,120] of nanotubes with hydrogen peroxide at elevated temperatures.

Nitroxide Mediated Radical Polymerization

It was originally believed that the nitrogen doped nanotubes would exhibit a greater degree of functionalization from the initiator/mediator radical pair treatment. TGA in argon was used to determine the extent of functionalization and can be seen below in Figure 28. In this instance a correction file with pure pristine and nitrogen doped CNTs was run to differentiate between the decomposition of the radicals and any other surface species not introduced by the functionalization treatment. The final weight loss was nearly identical, indicating both types of nanotubes were functionalized to the same degree. A difference does however occur in that the weight loss from the pristine nanotubes starts significantly after the weight loss from the nitrogen doped nanotubes. While the CN_xNTs start to lose mass almost immediately

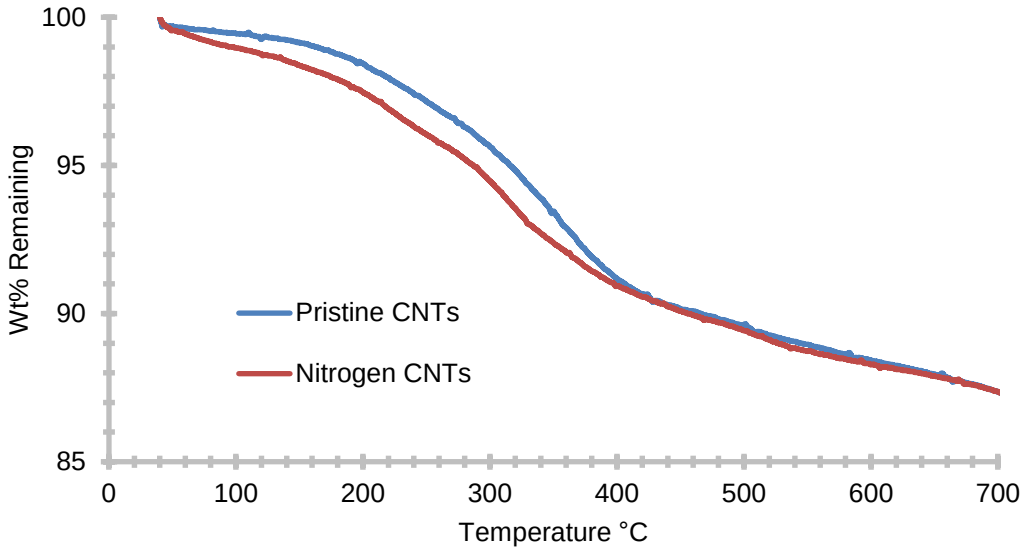

Figure 28: TGA in inert of pristine and nitrogen doped CNTs after functionalization with radical initiator/mediator pairs showing a difference in desorption temperature between the two nanotubes. TGA performed with 60 sccm Ar flowing and a ramp rate of 2°C/min

upon heating, the pristine tubes don't show mass lost until 90°C. This is in agreement with the idea that the nitrogen groups act as a p-type dopant, which would make it harder for a nanotube to give up an electron to form the bond with the radical, as proposed in chapter 3.

The sample was determined to have potential for selectivity particularly at lower temperatures where the radical pairs are more tightly bound to the pristine nanotubes than the nitrogen doped nanotubes. Polymerization was carried out at 80°C, and the results can be seen in Figure 29. Both pristine and nitrogen doped nanotubes showed a significantly large weight loss than their unpolymerized counterparts. The nitrogen doped nanotubes were 15.11 wt% polymer while the pristine nanotubes were 2.06 wt% polymer, indicating an 7.3:1 selectivity towards polymerization on the nitrogen doped nanotubes. Both polymerized nanotubes showed two distinct weight loss peaks, one which

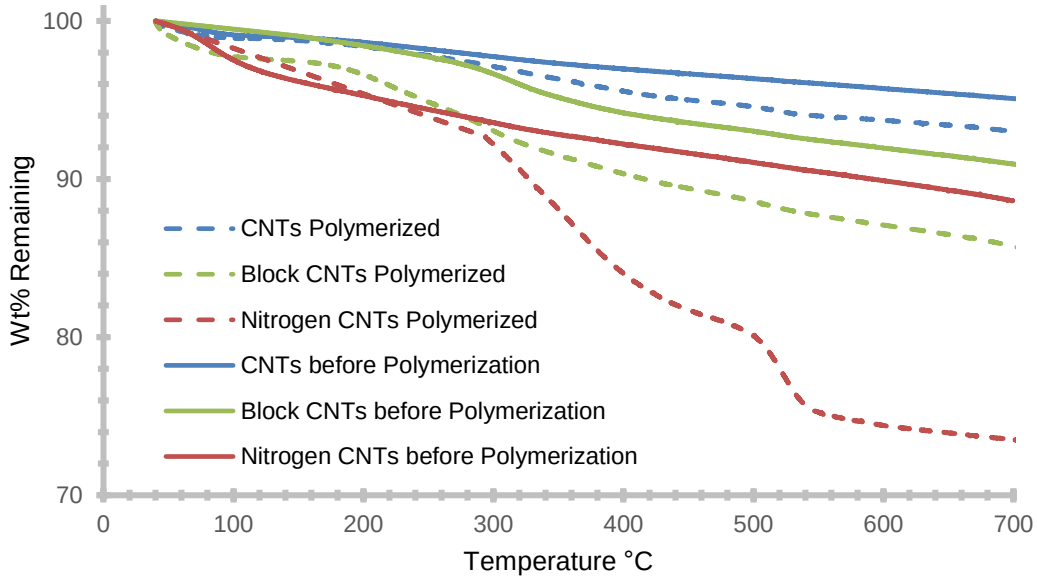

Figure 29: TGA of pristine, nitrogen doped, and block nitrogen doped nanotubes before and after polymerization using final weight changes to measure the amount of polystyrene attached to the nanotube. TGA done in 60 sccm Ar with a ramp rate of 2°C/min.

would be the thermal decomposition of polystyrene into its monomer units between 300°C-400°C and a second smaller peak above 500°C, though the pristine nanotubes second weight loss is very small. The second peak is attributed to the decomposition of heavier coke like products formed during the first decomposition stage. The same polymerization procedure was attempted with the block nitrogen grown CNTs, and can also be seen in Figure 28. The block functionalized nanotubes also showed polymerization, 9.6 wt%. Assuming each half of the nanotube is functionalized similar to what the pure component halves were then the nanotube can be assumed to be 54% nitrogen doped.

TEM was used to determine if the nanotubes were truly block functionalized. There was concern that the electronic effects of the nitrogen doping which allows for the selectivity in functionalization would be transferred

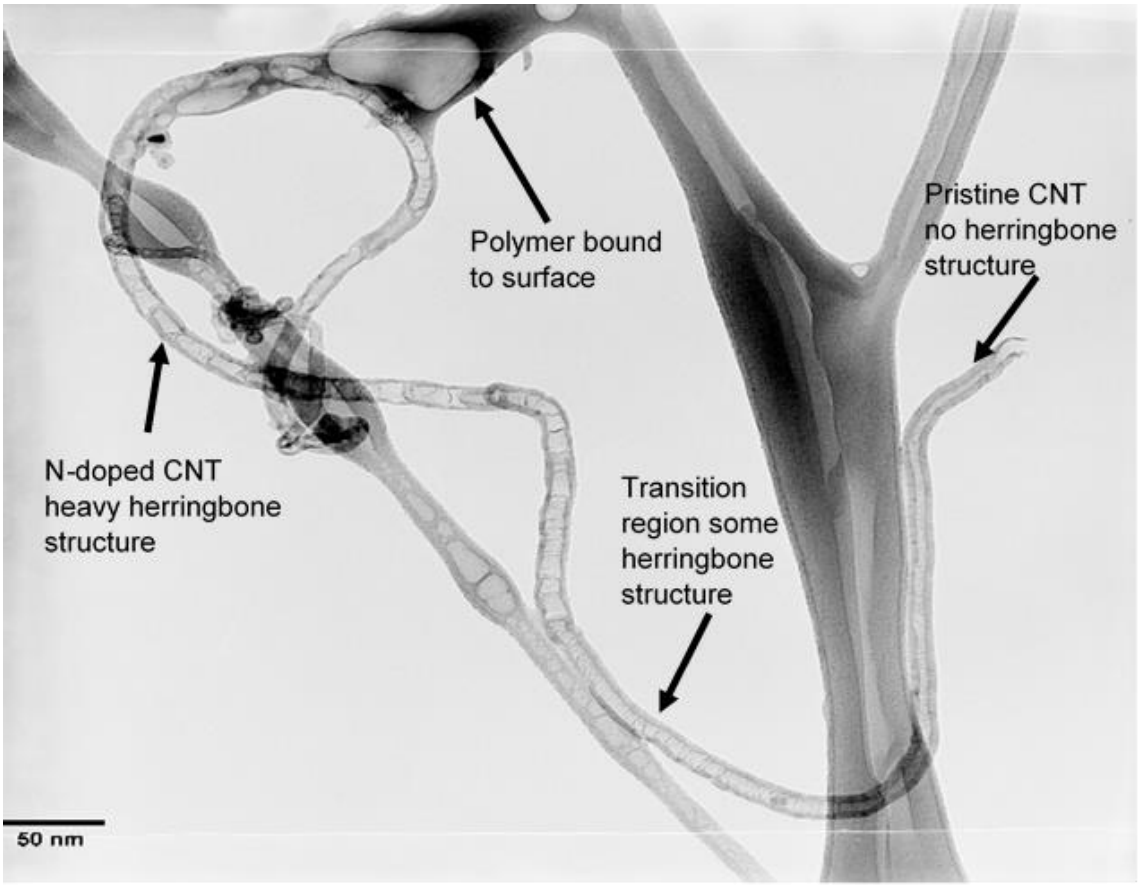

Figure 30: TEM image of a block functionalized nanotube with polymer attached selectively to the end with the nitrogen doping.

along the length of the conductive nanotube. Figure 30 shows a TEM image of a single block functionalized nanotube. The nanotube is supported on a lacy carbon grid, which can be seen in the background. Note similarly to Figure 6, a difference can be seen in the strength of the herringbone structure along the length of the nanotube, indicating a change in the nitrogen doping along the length of the nanotube. A small amount of polymer is attached to the upper portion of the nanotube, where the herringbone structure is the strongest. This polymer decomposed rapidly under the beam, indicating it is of low molecular weight. The polymer can be differentiated from the lacy carbon grid primarily by

its movement under the effects of the electron beam, and its firm attachment to the nanotube.

A second conclusion can be drawn from Figure 28, in that if the radical pairs leave the nitrogen doped nanotube surface more easily, it may be possible to functionalize a nanotube with the radical pairs, and then remove them selectively from the nitrogen doped side allowing polymerization to only occur on the pristine side. This would effectively reverse the selectivity of the nanotube polymerization step. To accomplish this, the radical pairs were washed 3 times in 100 mL of boiling benzene. The polymerization temperature was increased to 120°C and lasted for three days increase the polymerization on the pristine nanotubes.

The results can be seen in Figure 31, a clear selectivity switch to the pristine nanotubes. The pristine nanotubes ended up at 44 wt% polymer, while the CN_xNTs ended up 1.9 wt% polymer. This is slightly misleading however, when looking at the nitrogen doped tubes before and after polymerization at temperatures less than 200°C the nanotubes without polymerization show a greater mass loss than the nanotubes with polymerization. It is likely that the washing in boiling solvent removed some of the weakly bound surface groups that are known to come off the nanotubes at low temperatures, and these are not being taken into account when looking at the wt% polymer. If taken into account, then a more accurate method for determining the wt% polymer in the nitrogen doped nanotubes is to only look at the weight loss between 250°C and 400°C, which is 6.4 wt% polymer. This same phenomenon holds true with the

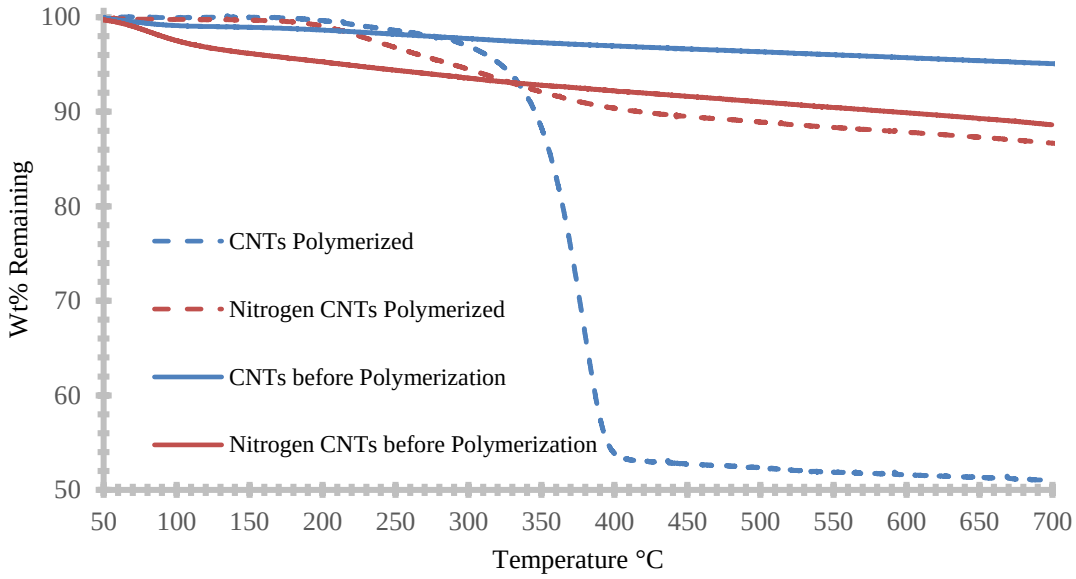

Figure 31: TGA of pristine and nitrogen doped nanotubes before and after polymerization following a heavily washing of the nanotubes in benzene to remove radical pairs weakly bound to the surface. TGA was performed in 60 sccm of Ar with a ramp rate of 2°C/min.

pristine CNTs, it appears than the wash removed surface groups ordinarily present, however in the pristine case it is less than 0.5 wt% due to the fewer surface groups on the pristine nanotubes. This leads to 6.9:1 wt% ratio of selectivity towards polymerization on the pristine half of the nanotube.

Interestingly the second weight loss observed in the first polymerization method at temperatures above 500°C is not seen in either the nitrogen doped or pristine nanotubes in the reversed polymerization case. It is possible that the MW of the polymer is lower, and as a result the polymer completely decomposes at the low temperature region, rather than partially decomposing and forming coke. With the increased temperature it is possible both to have an increased number of polymerization sites and even potentially free polymerization, which would lead to a lower MW polymer at each site assuming styrene is completely consumed during the reaction.

While the conditions for a block functionalized nanotubes have been met, namely the two halves of the nanotube have different functionalities, this reversibility of the selective polymerization leads to a potential for a block polymer functionalized nanotube, meaning each side has a different polymer functionality on it. If the nanotubes can be functionalized with a pristine selective functionalization, and then refunctionalized with the initiator/mediator radical pairs, it is possible for functionalization to occur with a different monomer species, leading to a two polymer block functionalized nanotube.

In the case of selective polymerization towards the nitrogen doped nanotube, it is the binding strength of the radical pairs to the nanotube which allows selectivity of initiation and therefore growth of the polymer. Once the mediator species is separated from the nanotube by several monomer units, the radical is shielded from the effects of the nanotube. This means in the 2-polymer block case the mediator which is terminating the polymer chains grown on the pristine half of the nanotube during the first growth phase will need to be removed. Additionally, the radical pairs used for growth on the nitrogen side will need to not be attached to a styrene ring on the pristine half of the nanotube, or branching will occur. Work is ongoing in these areas.

Conclusions

Three methods were used to try to take advantage of the selectively placed nitrogen groups on the carbon nanotubes, non-covalent adsorption of species, selective oxidation, and a living radical polymerization. Selective adsorption did not work as the hydrophobic backbone of the polymer

preferentially adsorbed on the nanotube rather than the carboxylic groups on the polymer adsorbing on the basic sites. Selective adsorption on the basic sites with small molecules is possible as describe in Chapter 3, so perhaps the acids on the polymer did bind to the pyridine groups, but this assertion was not proven. Selective oxidation was not achieved either. EDX is insufficient for detecting the oxidation because of poor resolution, though TGA showed more promise. Selective oxidation may still work with another reagent.

NMRP proved to be selective to either the nitrogen doped side or the pristine side based on the pretreatment of the nanotubes prior to polymerization. After addition of the initiator and mediator groups to the nanotube the nanotubes can either by washed heavily and then polymerized at high temperatures to selectively polymerize on the pristine half or not washed and polymerized at low temperatures to select the nitrogen doped half. This method will be used in Chapter 5 to produce the polymer functionalized nanotubes at a polymer-polymer interface. Only one side of the blocks were functionalized and studied in polymer blends.

Chapter 5: BF-CNTs at Polymer Interfaces

ADCB testing describe in this chapter was done by Fatoumata Ide Seyni. Everything else, and the words in this chapter, are the authors.

Introduction

Polymers are generally immiscible and when blended immiscible polymer will form a phase separated mixture[32,121-125]. Weak adhesion forces are known to cause a weakening of the mechanical properties of the blend[32,121,123-125]. One method of improving both the dispersion and the interfacial adhesion is to add a block copolymer which acts as a compatibilizer between the two phases[121]. This method acts to both decrease the domain size as well as strengthen the interface directly[126,127]. The copolymer is driven to the interface by thermodynamics, or as will be discussed later can be placed there directly.

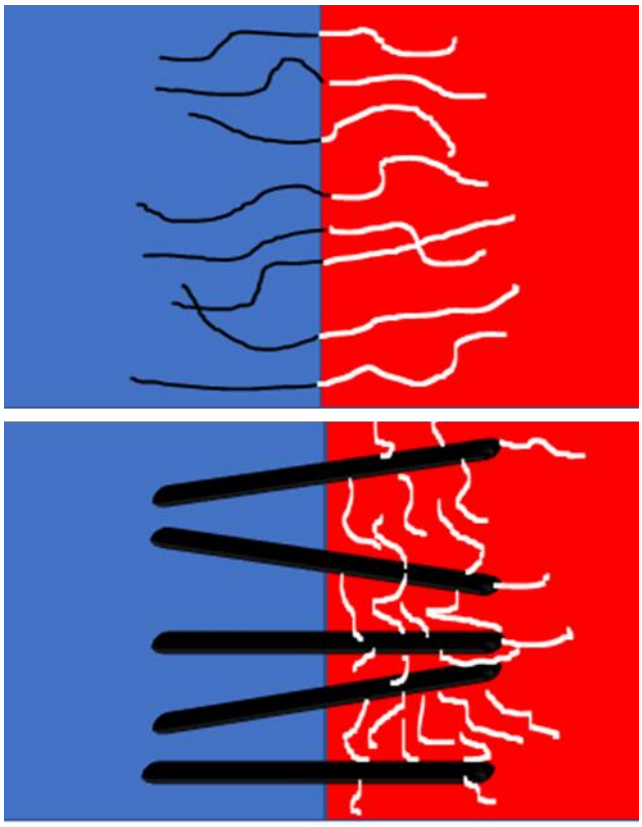

Figure 32: Diagram of: Top- polymer interface with block copolymer spanning the interface. Bottom-interface with nanotubes spanning the interfaces based on polymer attached to half the nanotube.

The copolymer can be thought of as a surfactant in the sense that it lowers interfacial tension, allowing for the smaller

minor phases to occur. Additionally, the copolymer chain will entangle with the homopolymer chains in the phase it resides in, strengthening the interface. A schematic of this can be seen in Figure 32. In this manner the copolymer acts as two connected anchors, with one being in each phase. Because the copolymer is driven to the interface by thermodynamics it should be possible to place other objects, such as a nanotube, at the interface using the same functionalities.

The issue with adding block copolymers is their tendencies to form micelles[32,123,124,128]. Micelles are entropically favorable when compared to dispersion of a block copolymer at the interface, and once formed are difficult to break. Multiblock polymers have been used to circumvent this issue[125,129], however they have a tendency to separate from the polymer blend by forming lamellar layers after undergoing shear stress[125]. As discussed in Chapter 1, Schmalz et. al. used this micelle formation to create a patchy nanotube[17,130]. Previous work by this group[5,19,35] and others[131-135] have shown that changes to the nanotubes surface chemistry can change which phase the nanotubes reside in, even showing movement from one phase to the other[19,135]. While this work is focused on covalent functionalization several interesting conclusions can be drawn from the patchy nanotube work. First the nanotubes will not form micelles themselves. This is critical for the block nanotubes to be useable in the polymer blend, and Schmalz et. al. reported not only no micelle formation, but also no agglomeration of nanotubes at all. Increases in dispersity are common in polymer functionalized nanotubes[20,94,100,118,135]. The second important

conclusion is the nanotube did reside at the blend interface. The nanotubes sat nearly parallel to the interface in this case, as it should be expected when the block functionality is organized according to the theta direction of the nanotube. The nanotubes produced in Chapter 4 have block functionality organized on the z direction, and thus should not sit parallel to the interface, but rather perpendicular to the interface, or at least significantly angled with respect to the interface, as can be seen in the bottom of Figure 32. The final conclusion is the result on the mechanical properties of the polymer blend. In the case of patchy nanotubes the domain size of the polymer blend decreased by an order of magnitude by addition of the patchy nanotubes, which Schmaltz et. al. attributed to a change in the surface tension. A solution casting of the polymers with the nanotubes will be used to determine if this is also the case for the BF-CNTs, as well as to determine the orientation of the nanotubes at the interface. A more complicated method for probing the effects a compatibilizer has on a blend is by measurement of the interfacial strength.

One method for probing the interface strength is the asymmetric double cantilever beam test, ADCB test. The ADCB test measures the energy per unit area needed to separate two polymer sheets after compression molding the sheets together. A wedge is driven in between the two sheets and a crack is allowed to propagate. The length of the crack can then be related to the stiffness of each material, as well as the energy required to separate the interface, assuming the crack lays on the interface[136]. Compatibilizer is typically

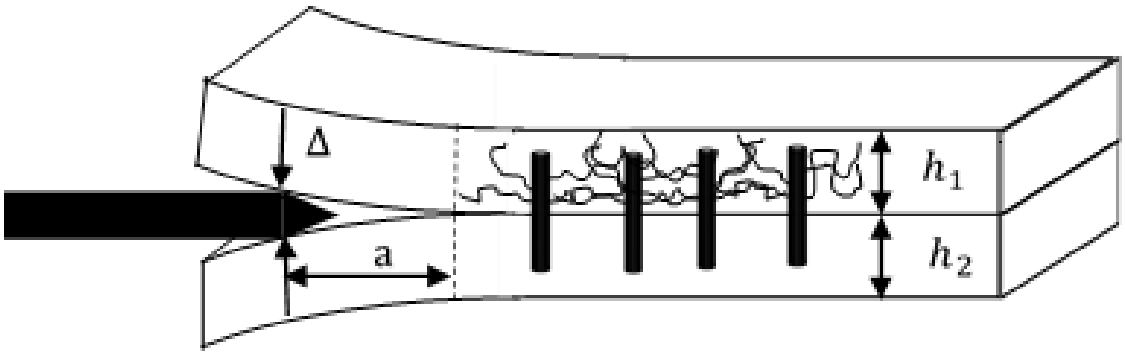

Figure 33: Diagram of an ADCB test using block functionalized CNTs as a compatibilizer.

applied to the top of one or both of the sheets prior to molding. A diagram of the ADCB test using BF-CNTs as a compatibilizer is shown in Figure 33.

If cracks enter into the bulk polymer, they will contribute significantly to the measured interfacial toughness[121,137]. Crazing is a particular type of behavior that represents the formation of microcracks and can dissipate significant amounts of energy. The growth of crazes will increase the measured strength of the interface by alleviating stress in each material, so the crack does not propagate as far as it would in the absence of crazing. The measured interfacial toughness, G_c, is proportional to the inverse of the crack length, so the decrease in crack length due to crazing or any cracking propagating into the polymer will lead to a toughness value that is higher than the actual interfacial toughness.

The equation for calculating the interfacial toughness can be seen in Equation 1[121,138]. By making the stiffness (i.e. absolute stiffness, not the stiffness/area) of the two components equal, chances of propagation can be minimized. Hence, the thickness of the polymer wafers is such than the stiffer

material is thinner than the more pliable polymer proportional to the ratio of moduli leading to the asymmetric in the ADCB test.

Equation 1: Interfacial toughness measurement between two polymer wafers where G_c is the interfacial toughness, E is the Youngs moduli for a material, h is the height of the material, Δ is the thickness of the razor, and "a" is the length of the crack.

$$G_C = \frac{3\Delta^2 E_1 E_2 h_1^3 h_2^3 \left(\left(1 + \frac{0.64h_1}{a}\right)^2 E_2 h_2^3 + \left(1 + \frac{0.64h_2}{a}\right)^2 E_1 h_1^3 \right)}{8a^4 \left(\left(1 + \frac{0.64h_1}{a}\right)^3 E_2 h_2^3 + \left(1 + \frac{0.64h_2}{a}\right)^3 E_1 h_1^3 \right)^2}$$

The final method considered for measuring the strengthening effect of the nanotubes at the polymer blend interface is by melt mixing the nanotubes into the polymer blend and measuring its tensile strength. Most melt mixing methods break nanotubes to an average length of 500 to 1000 nm[139]. This is 1/5th to 1/20th the size of the nanotubes grown in the block functionalized manner, indicating the nanotubes would break into somewhere between 5 and 20 sections. This would cause a loss of the block functionality, resulting in either no effect or a false effect of the true block functionalized nanotubes on the polymer blend. For this reason, this method will not be attempted, and we will stick with the ADCB test and measuring the size of the domain under TEM for analysis of the effects of BF-CNTs on the polymer blend.

Polystyrene, PS (Sigma #43010) MW 192,000, and poly(methyl methacrylate), PMMA (Sigma #182230) MW 120,000 were chosen as the two polymers for several reasons. They are immiscible in each other and have similar viscosities which allows for direct comparison the two types of dispersed

blends, and most importantly the nanotubes grown in the lab were shown to be most easily dispersed in the PMMA phase without any functionalization or with oxidation, and favored the PS phase when functionalized with PS[19]. These polymers will be used both for the ADCB testing, as well as solution casting tests to measure the domain size of the minor phase under TEM.

Experimental

Solution Casting

Solution casting was used to create samples of the BF-CNTs for TEM. Samples containing a 80/20 and 20/80 wt% ratio of the PMMA to PS were produced by dissolving a total of 1 gram of polymer in 40 mL of THF. The polymer was allowed to dissolve under stirring for 1 hour, after which 0.1 g of the BF-CNTs were added. The solution was sonicated 1 minute to disperse the nanotubes and was allowed to settle for 1 hour so than any agglomerates were able to fall out of solution. 2 µL of solution was placed on a lacey carbon coated copper TEM grid, mesh size 300 and the solvent was allowed to evaporate off under an atmosphere saturated with THF. This was done to slow the drying process and allow the system to come closer to a thermodynamic equilibrium rather than being kinetically limited. To assist the system in reaching an equilibrium state the sample was annealed at 120°C for 4 hours, which is above the glass transition temperature for both polymers. The samples were analyzed by a Zeiss 10A TEM operating at 60 keV. Images were analyzed with ImageJ software to measure the size of the minor phase droplets.

Asymmetric Double Cantilever Beam Testing

Nanotubes were dispersed in toluene via sonication in a bath sonicator at a concentration of between 1.5 g/L for 20 minutes. The dispersed nanotube solution as deposited onto a 40mm x 120 mm x 2.1 mm PMMA wafer and spin coated at 2,000 RPM to leave a small film of nanotubes behind after the solvent evaporated. The wafer was then compression molded with a 2.3 mm thick PS wafer at 120°C for 2 hours.

The samples were cut down to 8 mm in width with a band saw using a blade with 14 TPI and the edges squared with a belt sander. A single bevel razor was inserted between the two phases using a servo motor to ensure an even force across all samples. The crack was allowed to propagate for 24 hours to ensure the forces were at an equilibrium and the crack length would be stable. Crack lengths were measured with an optical microscope for the bare interface with no nanotubes, pristine CNTs without functionalization, pure CN_xNTs with PS functionalization via NMRP, block pristine/CN_xNTs without polymer functionalization, a physical mixture of CN_xNTs with and without polymerization, and the nanotubes that were block functionalized with the polymer on the nitrogen doped half. All nanotubes were grown to the same total length, meaning nanotubes containing only one phase are twice as long as the corresponding phase in the block nanotubes, but are otherwise grown, purified, and functionalized in accordance with the procedure described in Chapters 2 and 4.

Results

Solution Casting

Images were obtained with the both 80/20 and 20/80 wt% PMMA/PS. Minor phase size was measured across 40 pictures both with and without nanotubes. In all cases the average size of the minor phase was significantly smaller than half the nanotube. This indicates the nanotube cannot reside as theorized, half in each phase. In all cases a select few globules were observed which were capable of containing a nanotube. An image of a block nanotube at the interface can be seen in Figure 34.

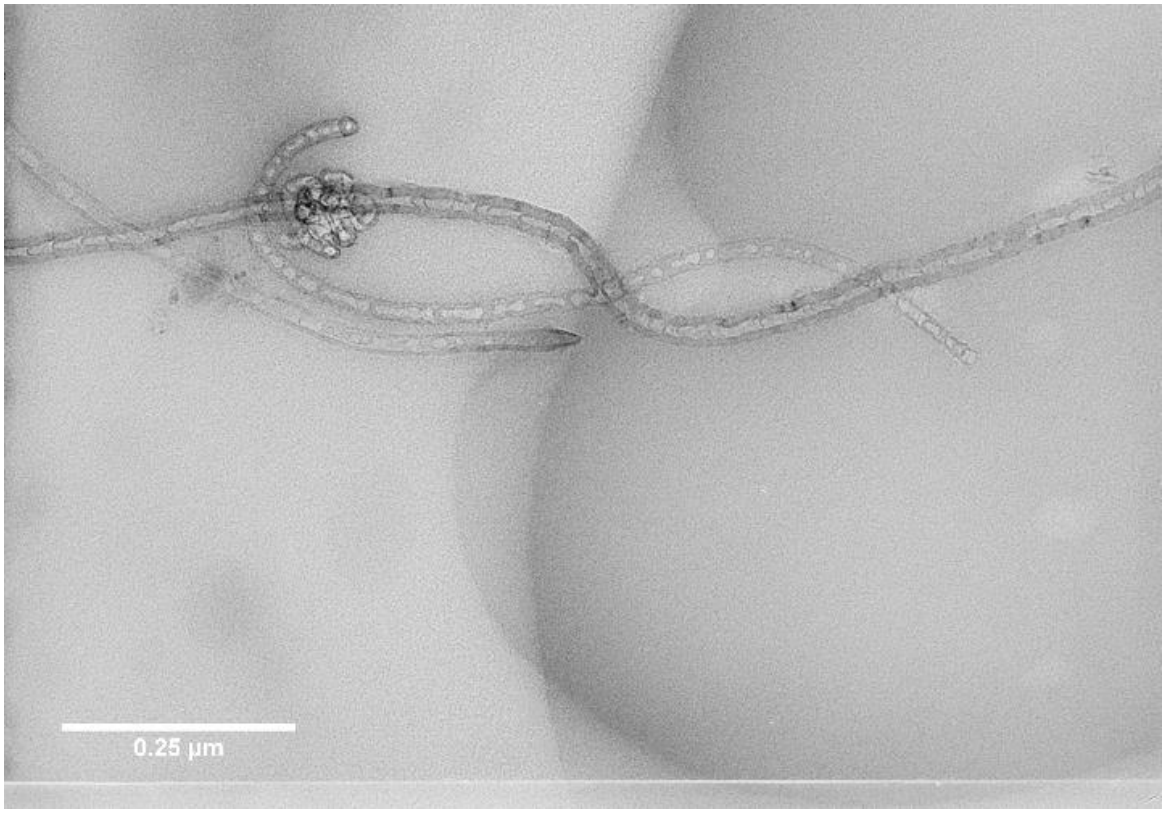

Figure 34: Block functionalized nanotube at a PMMA/PS interface, using a 80 wt% PS, 20 wt% PMMA blend. The bamboo like structure of the nanotube can be seen preferentially in the lighter PS phase, and the pristine nanotube can be seen preferentially in the darker PMMA phase.

The lighter phase is the PS and the darker phase is the PS. The herringbone structure of the nanotube can be used to determine the likely location of the grafting PS groups on the nanotube, though as Figure 24 in Chapter 4 shows, the entire nitrogen doped section may not contain PS groups grafted to the surface. In Figure 34, in can be seen that the nanotube lays almost perpendicular to the interface, with the interface residing roughly at the pristine/nitrogen doped transition region. This is one of the few samples which

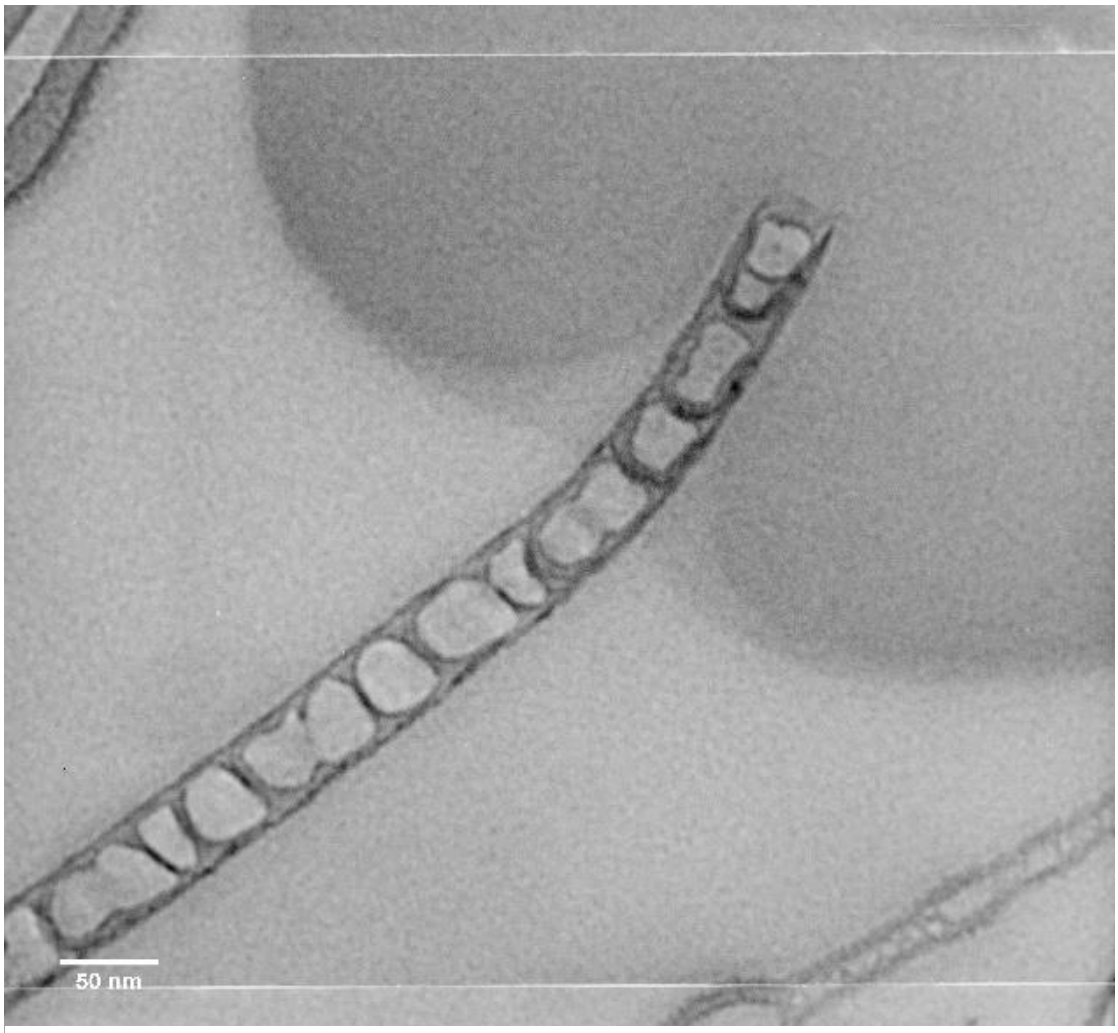

Figure 35: Nitrogen doped nanotube at a PMMA/PS interface, using a 80 wt% PS, 20 wt% PMMA blend. The bamboo like structure of the nanotube can be seen preferentially in the lighter PS phase, but is being forced into the darker PMMA phase, likely through drying effects. This distorts the shape of the minor phase, as the surface is incompatible with the polymer.

exhibited a minor phase large enough to contain half a full sized BF-CNT, approximately 2.5-5 microns. Interestingly a second nanotube, which is entirely n-doped can be seen overlapping with the BF-CNT. Where this nanotube lays a distortion in the darker PMMA phase can be seen, indicating it was forced through the interface, likely from the drying effects. A second example of this can be seen in Figure 35.

The minor phase was measured with image J and the results are shown in Figure 36. It can be seen that when the PMMA is the minor phase the size is much smaller. This is possibly an artifact of the drying rate, or the surface tension of the minor phase being different between the two polymers. The presence of nanotubes had differing effects on the two sets of blends. The PS in PMMA showed significantly larger minor phase regions, and the size of them increased with the presence of nanotubes, while the inverse is true of the

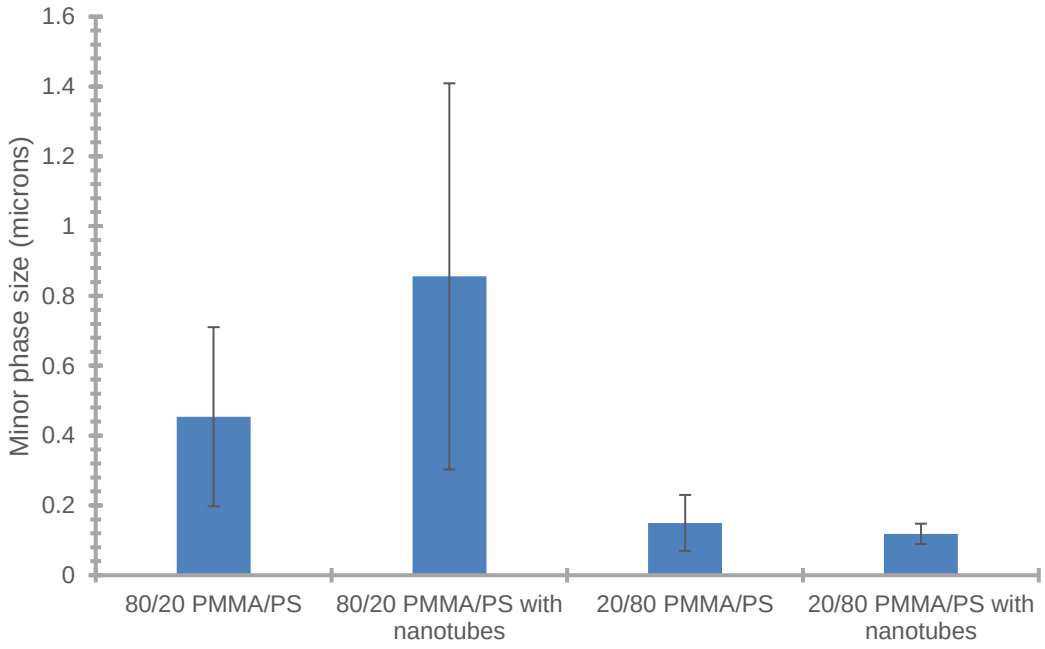

Figure 36:Minor phase size of PMMA/PS blends from solution drying, measured by TEM and shown with standard deviation.

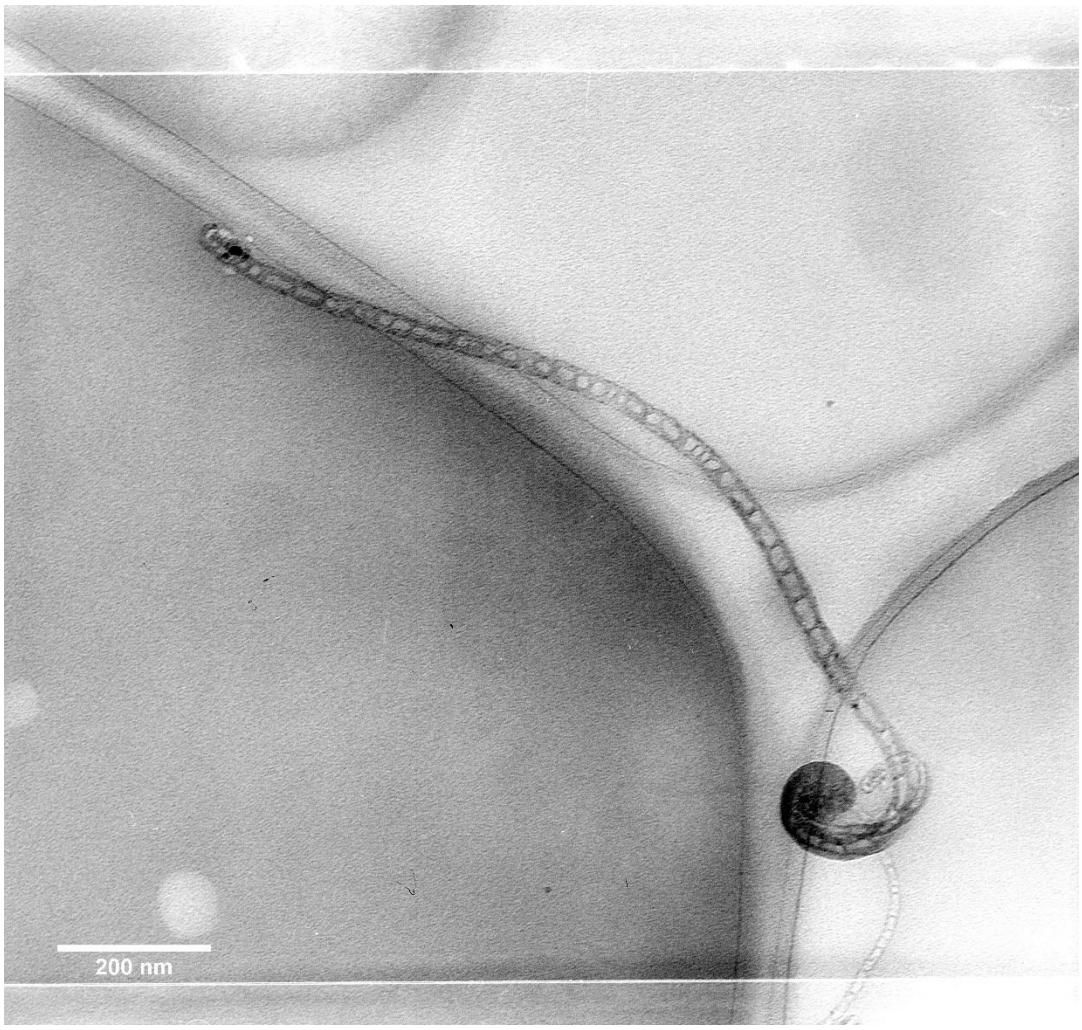

Figure 37: TEM image of a nanotube fragment skirting the PS/PMMA blend interface demonstrating the system is kinetically limited.

PMMA in PS. Even though the phases were smaller, only the PS in PMMA was found to have any nanotubes at the interface. It is likely kinetic effects limited the placement of the nanotube during drying, and the subsequent annealing was insufficient to overcome them. Figure 37 shows a nanotube skirting the interface of a minor phase, indicating it is not thermodynamically driven through the interface as expected, indicating the solution casting method may be kinetically limited. Figure 38 shows an example of the PS in PMMA images without nanotubes used to calculate the minor phase dispersion size.

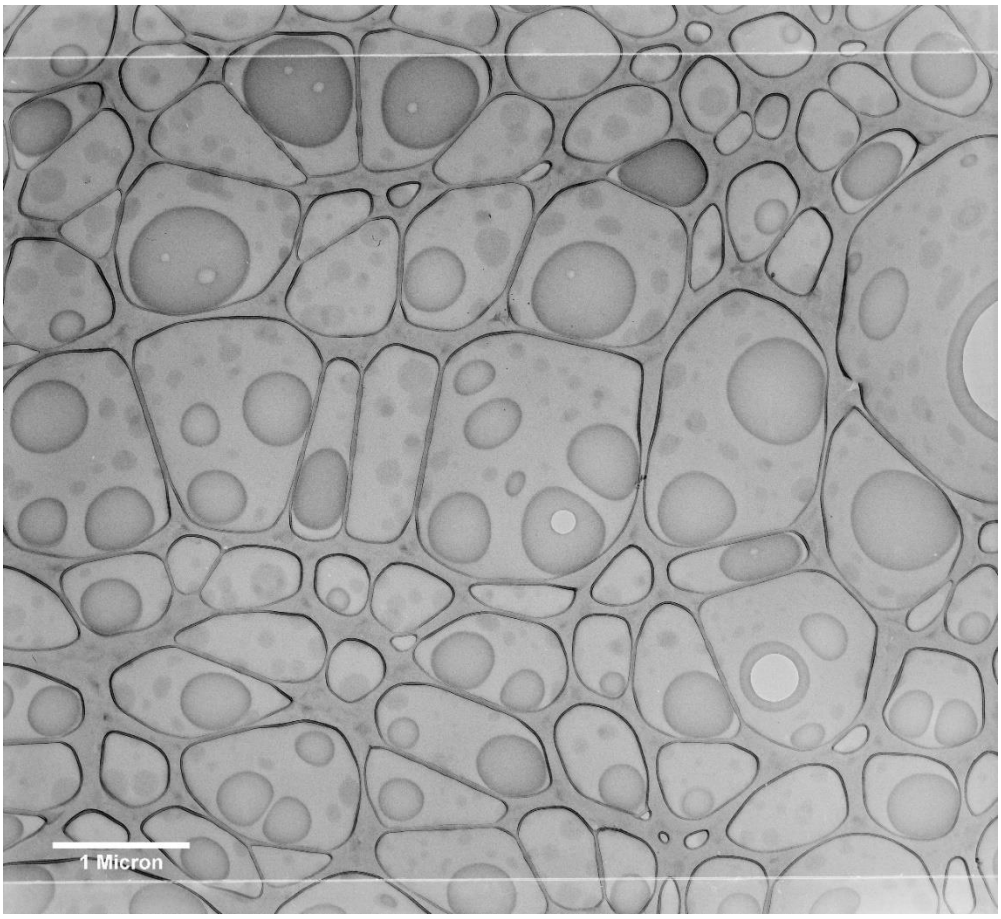

Figure 38: TEM image showing an example of the dispersion measurements for the minor phase. This is the 20 wt% PMMA phase blend without nanotubes.

ADCB Testing

A series of different types of blank runs were used to identify the effects of only the nanotubes at the interface. It is likely that a nanotube that is unfunctionalized will increase the toughness of the interface even if it is not block functionalized, so long as it resides at the interface. Its also possible a nanotube with or without functionalization in an non-block manner will penetrate into the phase it's surface chemistry is most compatible with, in which case it

will likely change the Young's modulus of the polymer, which would lead to inaccuracies in the toughness measurement. For this reason, the surface toughness was measured without nanotubes, with pristine nanotubes without functionalization, with a single phase nitrogen doped nanotube which had been functionalized via NMRP, and with a physical mixture of functionalized and unfunctionalized nanotubes as controls. The results can be seen in Figure 39.

All control tests did show an increase in the surface toughness measurements above the bare interface and are all within one standard deviation of each other. The bare interface value was found to be1.5 j/m^2, 3.5 J/m^2 less than the reported literature value for ACDB using very similar polymers[122]. There are two potential explanations of this, in the literature the ratio of thickness of the wafers had a strong effect on the bare interfacial toughness. Measurements were taken at a ratio of 1 and 1.2, which corresponds to approximately a 25 J/m^2 difference with 1 being higher than 1.2. The authors claim the minimum is at 1.2, as the values increase after this point while the value used in these experiments was 1.09. It is possible the true minimum energy lies at a ratio between 1 and 1.2. It is also possible that the significant difference in MW of the PS, 330,00 in literature, 192,000 in lab, cause this difference. Lastly the literature samples underwent compression molding at 165°C rather than the 120°C used in this experiment, leading to higher entanglement of the polymer chains and a higher toughness.

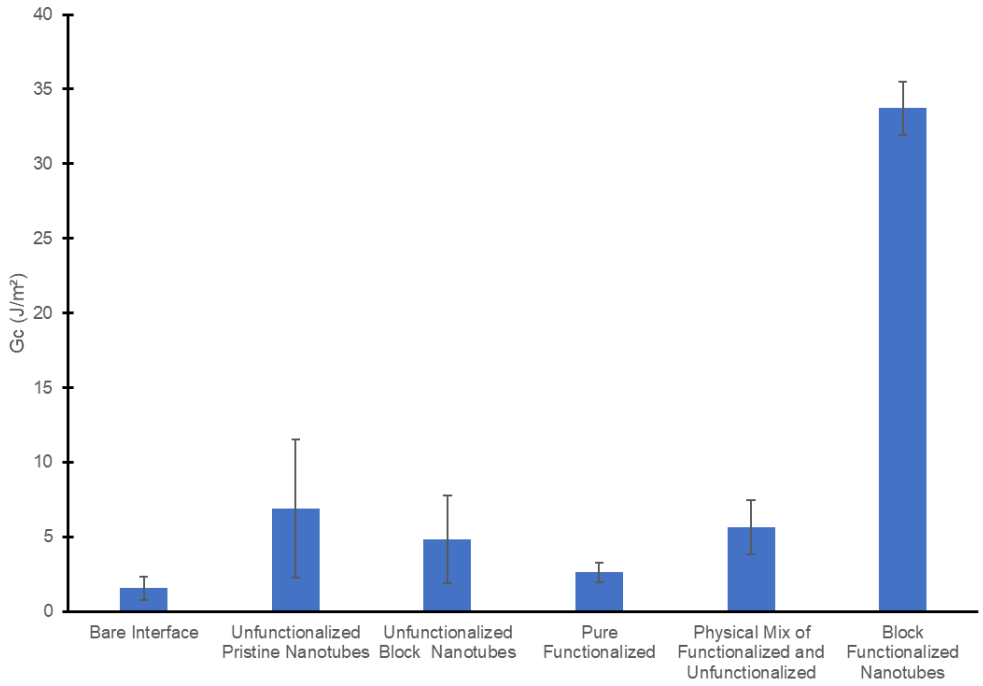

Figure 39: Interfacial toughness values for nanotubes at a PS/PMMA interface based on surface chemistry. All nanotubes were the same length and dispersed on the PMMA wafer using a concentration of 1.5 g/L, and an annealing with a PS wafer of 1 hour at 120°C

The block nanotubes were found to increase the interfacial strength to 33.7 J/m^2, 21 times the strength of the bare interface. This is also 4.8 times larger than the highest value of the control nanotubes, the unfunctionalized pristine nanotubes at 6.9 J/m. This increase on par with the literature values for di and triblock copolymers, namely 20-40 J/m^2 [122]. A large uncertainty is visible in all trials, likely due to dispersion issues of the nanotubes as well as end effects of the samples and defects introduced by the cutting and sanding methods.

Conclusions

Block nanotubes were placed at a polymer-polymer interface and the surface toughness was measured with asymmetric double cantilever beam

testing. The surface toughness was found to be in line with increases shown in block copolymer experiments, but the nanotubes do not form micelles, which means a larger percentage of the nanotubes can be used at the interface. Further work will be done to optimize annealing conditions and nanotube concentration to maximize the effect of the nanotubes. Blending the nanotubes into a polymer will be difficult due to breakage of the nanotube, which effectively removes their block functionality, but the results should show a significant increase in the mechanical strength of the blend. Solution casting of the nanotube to determine the orientation of the nanotube at the interface is ineffective as it is kinetically limited even after an annealing process.

Chapter 6: BF-CNT for Catalytic Studies

The following chapter is a result of collaboration between 4 students, Nick Briggs, who developed the initial procedure for the metal block functionalization of nanotubes and performed portions of the characterization the BF-CNTs and produced some of the tubes used for reactions, Leidy Herrera and Laura Gomez who performed the probe reactions, and myself who produced the nanotubes for reaction and hydrogen spillover experiments and completely the characterization of the nanotubes.

Introduction

Bifunctional Catalysts

Catalysts with multiple active functionalities have been increasingly popular in industry to do enhancements in both conversion and selectivity of products[30,140], and as such are an important area of research. One of the primary areas of work regarding catalysts with multiple active components is identifying the source of the increase in activity and selectivity. A bifunctional catalyst can allow for sequential reactions on the two separate active sites, allow a synergy between the active sites in which one promotes the other to become more active, can create a completely new site where the two functionalities join together, or can have some combination thereof to change the reaction products. This issue of identification of the active site(s) is multiplied when one or both of the bifunctional catalyst components have more than one active site, or multiple ways it can affect the other component. For instance, reducible oxides are often used as a support for a metal catalyst, and

together they show enhanced activity for C-C cleavage, C-O cleavage, C-O oxidation, and ring rearrangement reactions.

The activity of the metal functionality in the above described system can be affected by electronic or geometric effects from the support, with the active site solely on the metal, but with a heavy reliance on the oxide supports presence. The support material can affect the position of the d-band center of the metal with relation to the fermi level. When the d-band center becomes closer to the fermi level a greater number of the antibonding states exist above the fermi level , leaving them unoccupied, leading to a stronger bonding of the adsorbate to the metal[141,142]. This will result in a rightward shift in the standard volcano plot and will thus result in higher or lower activity based on the initial starting point. The possible geometric effects are due to size, shape, and orientation of the metal dispersed on the support and can include the ensemble effect, the template effect and the coordination effect[140,143,144]. The ensemble effect is the where the adsorbate requires a specific number of adjacent surface atoms to adsorb at a site, the template effect is where an adsorbing molecule requires a site of a specific size and shape, and the coordination effect is where multiple adsorption sites must be within a proximity to one another for the reaction to occur. If a support facilitates a near single atom dispersion or complete sintering of the metal it is easy to see a reaction controlled by geometric effects could not have the active sites needed. If multiple reactions are occurring and one is geometrically controlled, it is then obvious that selectivity would shift even with the same loading of metal.

The oxide can contain metal cations which accept electrons and are thus Lewis acids as well as oxygen ions which behave as a Bronsted base[145,146]. In the case of reducible oxides, hydrogen can spill over from the metal a short distance to produce OH groups, oxygen vacancies, and surface/subsurface defects[147-151]; or an oxide layer can form on the metal[140], all of which become new potential active sites.

The variety of effects the metal and oxide have on each other can be divided into two categories, long range promotor effects and short range effects. Short range effects are where the metal and oxide must be physically touching at or near the active site. Such effects would include the geometric and electronic effects on the metals, vacancies formed in the oxide immediate adjacent to the metal, formation of a thin oxide coating on the metal surface, and creation of new active sites at the interface. Promotor effects then are where the active site is found on the support and is the result of hydrogen spillover from the metal[151]. These sites would include the OH groups, surface and subsurface defects, and Bronsted acids or bases. The litany of potential causes for the catalytic increase leads to conflicting literature reports[152], as current methods for identification are not definitive, but rather suggestive of the active site.

One of the more popular methods for determining the active site in such a metal supported on an oxide case is to change the particle size of the metal. If this is done in a manner that does not change the number of active sites on either the metal or the oxide, and the metal is distributed sufficiently to allow

spillover to the same area of support in all cases, then a direct comparison of the activity to the number of interfacial sites can be seen. A lack of correlation between the rate and the number of sites then attributes the active site to the promotor effects. Partial decoration and full encapsulation of the metal with the oxide will change the actual metal-oxide interfacial site population[150,153-156], and it is unlikely metal particles of different sizes will generate promotor effects evenly across a surface, yielding a potential observed change in reactivity from changing the particle size that is based on promotor effects. A second technique is in situ spectroscopy of the sample during reaction to study the surface species and their binding locations. In a simple model with few reactants and single component catalyst this can be strait forwards and fairly helpful, however when the reaction requires multiple species of reactant, has long lived intermediates, multiple reactions occur, or the catalyst becomes more complex little information can be gleaned from spectroscopy. Not every adsorption occurs at a catalytically active site, so many adsorbed species can be spectroscopically observed, and yet not play a role in the reaction. Lastly kinetic models and DFT studies can be performed to identify which site is the most active or selective for a particular reaction, however these are foiled by the complex nature of the bifunctional catalyst system. A new method is therefor needed which can easily differentiate the active site in the multicomponent catalyst systems.

Block Nanotubes for Active Site Determination

This work is focused on a new method to identify active sites using block functionalized carbon nanotubes. The BF-CNTs are created such than physical separation of the metal and oxide particles occur, with each one on opposite ends of a carbon nanotube and compares the reaction results to a catalyst in which the metal and oxide are stack on the same side of the nanotube. In this manner a direct relation can be seen between the presence and absence of interfacial sites and the activity of the catalyst. The production of the BF-CNTs will not be in the same manner as described in Chapter 4. Rather than introduce 1 functionality selectively with the second half of the nanotube remaining unfunctionalized, both halves will need to be functionalized. As particle sintering is a valid concern for metal nanoparticles, particularly at elevated reaction temperatures, a large space will be to be maintained between the metal and oxide in the separated case to ensure they remain separated. This will in effect require then a 3 phase block functionalized nanotubes; a section on one end with only metal A, a large unfunctionalized section in the middle, and a section on the opposite end functionalized with metal B, which can then be oxidized to form the reducible oxide.

One way to achieve this would be to mimic the polymer masking work of Dai et. al. in which they embed a vertically aligned forest of MW-CNTs in a molten polymer a known distance. They then coated the exposed half of the nanotube with platinum nanocubes. The exposed half was then imbedded in a polymer with a difference miscibility and the first polymer was washed away.

Platinum nanospheres were then coated onto the now exposed first half of the nanotube. The second polymer was washed away and a block metal functionalized nanotube was created[28]. If a thin layer of the second polymer was added on top of the first polymer prior to penetration of the forest into the polymer layers, the thin layer of the second polymer would be in place during both the first and second functionalization and would then enable a barrier to exist where neither metal nor oxide existed to prevent sintering of the two catalytic species towards one another. Polymer masking has the disadvantage however of requiring precise manipulation of the forest into the polymer. If the polymer is too viscous the nanotube forest will break rather than enter, if the polymer is not viscous enough the liquid will climb the forest from capillary effects and coat more of the forest than intended. This difficulty is increased when considering two polymers of different miscibility at the same time, as proposed above. This technique was disregarded in the previous chapters as it is not scalable in the same way wet chemistry functionalization is and could therefore only produce lab scale quantities, however this study is only concerned with research purposes, so lab scale quantities are sufficient.

Shortly after the idea of masking, Dai et. al. developed another technique which showed greater promise for the purpose of block metal functionalization, namely sputter coating[18]. Dai et. al. used sputter coating on a forest of vertically aligned CNTs to place electrodes on a forest which had been previously polymer masked. Sputter coating has the advantage of not requiring embedding of the forest in a polymer. If the nanotube forest is dense enough, sputter

coating will only functionalize the top portion of the nanotube. The evaporated metal atoms in a vacuum will move in a straight line, meaning only the portion of the nanotube which can been seen by the metal source will be functionalized. The forest can then be flipped, and the second metal evaporated onto the opposite end.

Hydrogen Spillover

The theorized technique of block functionalization is only useful for identification of promotor/short range effects if hydrogen is able to spillover from the metal, across the nanotubes length to the oxide, onto the oxide and create the various defects on the oxide that have catalytically active potential. It is well documented in literature that carbon materials can be used for hydrogen storage[157-165]. This is particularly true on nanotubes when a metal is present to dissociate the hydrogen which can then spill over onto the nanotube[157-159,161,164]. This is further enhanced when a bridge exists between the nanotube and metal, such as oxygen defects on the nanotube or through the shuttling of hydrogen by another species[157,159,161,163,166-168]. Mechanistically spillover on a nanotube occurs both through chemisorption[160,162,164,169] or physisorption[157,158,163]. Chemisorption in this instance refers to the dissociated hydrogen atom forming C-H bonds, which requires an sp^2 hybridized carbon to change to sp^3 hybridized. This method is likely to be slow, as transfer of the hydrogen beyond one carbon away from the metal requires the formation of a new C-H bond and a breaking of the old one. Chemisorption is assisted by oxygen groups on the surface, particularly alcohols[161,162,167], indicating a hydrogen shuttling may be

occurring. Physisorption occurs with weakly bound hydrogen atoms moving over the surface of the nanotube and is energetically favorable[163], but is also easily recombined to form H2 on the surface due to the lack of C-H bonds to stabilize the hydrogen atoms[158].

With this literature evidence there is no question if hydrogen spillover will occur, so the questions become (1) over what distance can it occur, (2) can the oxide be reduced from the hydrogen on the nanotube, and (3) will the spillover be sufficiently fast to not limit the reaction excessively. It can be imaged that the reducing metal will assist in oxidizing the nanotube while converting the second metal to the oxide form. The oxygen groups may then be focused primarily near the metal end, and if the primary mechanism of hydrogen spillover is through shuttling between oxygen groups, the spillover rate may slow near the oxide end of the nanotube. If the only mechanisms left are chemisorption by the C-H bond formation or physisorption it is possible the C-H bonds will not break in favor of spilling the hydrogen onto the oxide to create the active sites and any physiosorbed hydrogen will have recombined to form molecular hydrogen by the time it has traversed the distance of the nanotube. Even if the spillover occurs ideally and the active site defects are generated on the oxide it is possible a reaction which consumes the defects will occur fast enough compared to the rate of spillover to limit the extent of the reaction to an imperceptible level, resulting in a false negative reaction test in the separated case. A perfectly idealized case of spillover across a block metal functionalized carbon nanotube can be seen in figure 40.

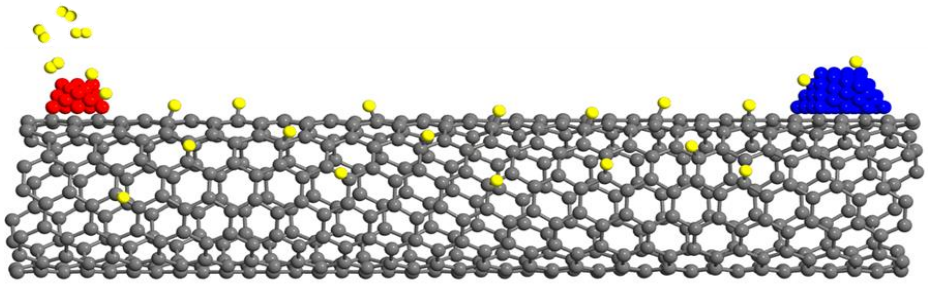

Figure 40: Block functionalized carbon nanotube showing a noble metal (red) allowing adsorption and dissociation of H_2 to atomic hydrogen which transfers across the nanotube via the chemisorption method and spilling over onto the oxide (blue) enabling reduction.

Reactions

Assuming the spillover occurs ideally, a series of reactions will be needed to show the system's ability to identify active sites, at least one which uses the promotor effect and one which uses the short-range effects. Additionally, a reaction which can be used to measure the defect sites on the titania will be of use for proving the stability of the spillover in the separated case. The ketonization of acetic acid will be used to monitor the population of titania defects, as the rate of ketonization has been shown to relate directly to the number of Ti^{3+} sites in the titania[170-172], without consuming the defects. Literature suggests furfural can undergo decarbonylation to furan and CO or hydrogenolysis, specifically selective C-O cleavage to methyl furan and H_2O over a noble metal catalyst, with selectivity shifting toward methyl furan, the more valuable product, when the metal is supported on TiO_2. Somorjai et. al. attributed this selectivity increase to spillover from the metal to the oxide to create defects, which he claimed are the active sites[173]. Medlin and Nikolla attributed this selectivity shift to defects in the titania at the metal/oxide

interface[174], claiming the defect allows the strong adsorption of the oxygen group, while the metal was then responsible for hydrodeoxygenation, requiring both sites to be in close proximity. This conflict allows for the perfect opportunity to test the block functionalized CNT catalyst system.

A second reaction which is known to occur selectively on the defect sites is the transalkylation of guaiacol to methyl catechol and cresol products over Ru/TiO_2[175,176]. A similar reaction will be tested, anisole conversion to cresol and phenol over copper supported titania to see if the active site is also the titania defects, which is expected. The final reaction to be testing will be a ring rearrangement of furfural. Furfural ring rearrangement to cyclopentanone and 2-cyclopenteneone has been known to occur in the aqueous phase over metals on various supports[177-180]. Recent work by our group has shown the ring rearrangement can also occur in the vapor phase if water is cofed with the furfural over Pd and Ru supported on TiO_2. While this reaction is known to occur on several supports, the TiO_2 is used to suppress the decarbonylation reaction. Because the reaction occurs on various supports it is not believed that the active site will be a promotor effect induced site. All of the proposed probe reactions will involve some form of C-O bond cleavage and use model compounds of a biomass conversion. The primary purpose of these reactions is to prove the viability of the BF-CNT active site identification method, not the optimization of the catalyst, which would come later as a result of the active site identification.

Experimental

The experimental section is taken from the paper “Identification of active sites on supported metal catalysts with carbon nanotube hydrogen highways” and can be found using the citation Nature Communications, 2018 vol. 9 article 3827. Nick Briggs performed the TPR and parts of the SEM and TEM. Liedy Herrera performed the acetic acid and some furfural reactions. Laura Gomez performed the anisole and furfural ring rearrangement reactions. Evan Wegner assisted with the XAS measurements and analysis.

Block Metal Functionalized Nanotube Production

The nanotubes were grown on silicon wafers supported catalysts which were prepared and reduced in accordance with the procedure set forth in Chapter 2. The growth was carried out using a 50/50 mixture by volume of ethylene and argon at 675° for a total growth time of 20 minutes. The nanotubes were then calcined to remove amorphous carbon and weaken the attachment of the nanotubes to the substrate to facilitate the flipping required in the block functionalization procedure. The nanotubes were placed in a horizontal quartz tube and heated to 480°C under 150 sccm of air at a rate of 10°C/min, before being held there for 2 hours before being cooled to room temperature.

The silicon wafers were taped in to a metal plate and placed inside a custom metal evaporation unit. A 1 mm tungsten wire was used as the filament for evaporation and was suspended 5 cm above the nanotube forests between two 1” copper electrodes. The metal to be evaporated was wrapped around the

tungsten filament, Pd wire of 0.5mm diameter and 5 cm length, Cu wire of 0.1 mm diameter and 10 cm length, and Ti wire of 0.25 mm and 10 cm in length. The sample area was pumped to a vacuum of 1E-9 Torr to facilitate the evaporation of the metal, which is accomplished by flowing 10 amps through the tungsten filament. Deposition thickness was monitored by a quartz crystal monitor place in the middle of all the nanotube covered wafers.

In all cases the metal that became the oxide was evaporated first. In the stacked case the second metal was evaporated onto the forest immediately after the first metal. In the separated case, the nanotubes were attached to an aluminum tape with a carbon based adhesive, which allowed the forest to be removed from the silica wafer while keeping its structure. The tape was placed nanotube side up in the metal evaporation unit and the second metal was evaporated onto the surface. The outer 1-2 mm of the aluminum tape was cut off from the bulk of the sample to ensure any nanotubes which could contain the metal and oxide in contact was removed. The tape sample was submerged in isopropyl alcohol for 1 hour to solubilize the adhesive and release the nanotube forests. The forests were recovered from the IPA via vacuum filtration.

Both the stacked and separated nanotube samples were calcined in the same system used to assist in the release of the nanotubes from the substrate, this time using 100 sccm of air at 350°C for 1 hour. This was done to remove any residual adhesive from the tape as well as convert the titanium and copper to the oxide form.

Characterization of the BF-CNTs

Scanning electron microscopy of the BF-CNTs was done using a Zeiss Neon 40 EsB with an accelerating voltage of between 1 and 30 keV, with higher voltages used when performing energy dispersive X-ray spectroscopy. Transmission electron microscopy was performed on a Jeol 2000 FX operating at 200 keV.

TPR of the catalyst was carried out using a vertical 0.25” quartz tube packed with quartz wool and 10 mg of sample. 30 sccm of 5% hydrogen in argon was passed over the catalyst and through a TCD. The catalyst best was ramped from room temperature to 800°C at 5°C/min.

X-ray adsorption spectra were collected on the bending magnet beamline of the Materials Research Collaborative Access Team at the Advanced Photon Source, Argonne National Laboratory. Measurements were performed at the Cu K edge (8.979 keV) and Ti K edge (4.966 keV) in step-scan transition mode. Catalysts samples were packed into a steel sample holder with ½ lb. of force to prevent breakage of the nanotubes or compression of the separated metals. The sample holder was placed in a quartz reactor tube, sealed with Kapton windows by two Ultra-Torr fittings, and through which gasses could be flowed. Measurement on the fresh samples were performed at room temperature after purging the reactor with He. A 3 mol% H_2/He mixture flowing at 100 sccm was used to reduce the samples, which were held at the treatment temperature for 30 minutes. Following reduction, the reactor was

purged with He until it reached room temperature and measurements were performed at room temperature under the inert atmosphere.

XAS data was processed using WinXAS v 3.2 and a standard normalization and background subtraction procedures[181]. For the Ti K edge, the oxidation state of Ti was determined by comparison of the sample edge energy to Ti foil, TiO_2, and Ti_2O_3 reference compounds. A least-squares fit in R-space of the K^2-weighted Fourier transformed EXAFS was performed to obtain coordination numbers and bond distances. The anatase phase of TiO_2 (6 Ti-O bonds at 1.96 Å) was used as an experimental reference for backscattering phase and amplitude fitting functions. A similar procedure was used to determine with EXAFS coordination parameters at the Cu K edge and experimental phase and amplitude fitting functions were constructed from NiO (6 Ni-O bonds at 2.09 Å) and Cu foil (12 Cu-Cu bonds at 2.55 Å). The quantities of Cu(II) and Cu(I) in each sample were estimated from the fractional coordination numbers obtained from fitting (i.e., the fitted value is the weighted average of the coordination numbers of Cu(II) (4 Cu-O bonds) and Cu(I) (2 Cu-O bonds) present in the sample).

TGA experiments were performed with the Cu/CNT samples described above as well as CuO powder physically mixed with nanotubes in a Netzsch STA 449F1 equipped with a pin thermocouple and a Netzsch nanobalance. Outlet gasses were analyzed by mass spectroscopy on an Aeolos QMS. All data was taken with a correction file to account for gas viscosity changes during nonisothermal operation. Prior to pretreatment of the sample, the crucible was

treated temperature at 1000°C under ultra dry air followed by argon to ensure an accurate zero measurement. Zeroing of the scale was done at 100°C under 40 sccm hydrogen to match the initial reduction conditions. The samples were pretreated by oxidation in air at 350°C for 2 hours as per the standard procedure for the catalyst to be used in reactions. Surface groups on the CNT were then removed by pretreatment for 1 hour at 375°C under 40 sccm. The samples were then cooled to 100°C under inert Ar flowing at 20 sccm. One the sample reached 100°C, the gas was switched to a flow of 40 sccm hydrogen until the mass stabilized. the TPR was performed from 100°C to 400°C under 40 sccm hydrogen with a ramp rate of 3°C/min.

Reactions

Catalytic activity for the different catalysts was tested in a quartz tube reactor (0.25” OD) at atmospheric pressure and 400°C. Catalyst particles were mixed with inert acid washed glass beads (Sigma #G1277) with a particle size range of 212-300 μm and packed between two layers of quartz wool inside the reactor. The quartz tube was placed in a furnace oriented vertically and connected to an inlet gas line at the top and an outlet gas line at the bottom. The catalyst was reduced by flowing 100 sccm of hydrogen through the quartz tube and heating the furnace up to 400°C and then holding at the same temperature for 1 hour.

Anisole, distilled furfural, acetic acid, and water were introduced to the reactor as noted in experiments at a flow rate of 0.16 ml/h for anisole, 0.1 ml/h furfural, 0.2 ml/h for acetic acid, and 0.25 ml/h for water. Ten milligrams of

catalyst was added in each case (with the exception of the physical mix samples, where 20 mg of material was added to the reactor to maintain consistent Pd, Ti, and Cu loadings, and the ring rearrangement case were 5 mg of sample was loaded). The outlet stream of the reactor was heated to 250 °C to prevent condensation of compounds in the transfer liens and then flowed through a six-port valve to allow for injection into a gas chromatography unit equipped with a flame ionization detector, Agilent 6890, using a HP-INNOWAX column (30 m, 0.25 μm) for product quantification. Identification of products was confirmed using a Shimadzu QP-2010 GCMS and standards were used to quantify the various products in the flame ionization detector.

Results

Block Nanotube Production

SEM showed the carbon nanotube forest to be on average 100 microns long with the designated growth conditions. TEM determined the nanotubes to be roughly 10 nm in diameter. Literature reports indicate the curvature of the nanotube surface will affect the energy of the C-H bond[158,182], which means if chemisorption is the primary mechanism of spillover the diameter of the nanotube is very important to the potential rate of spillover. Additionally the number of walls can have an effect on the spillover, not just because of the relationship between number of walls and diameter[140], but also for the potential of hydrogen transferring through defects in the outer walls to inner walls[167] and have a greater area and more mechanisms through which to diffuse[168]. The TEM images showed between 5 and 10 walls.

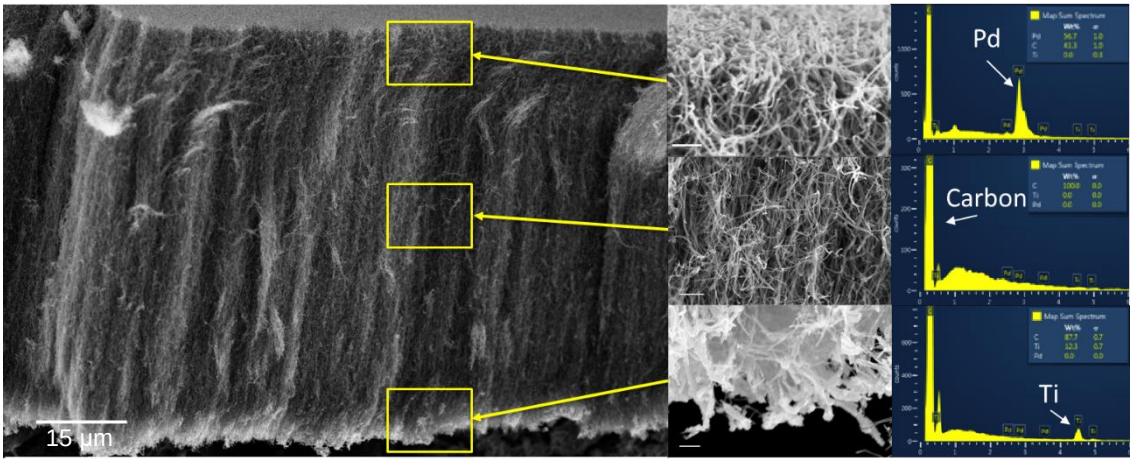

Figure 41: SEM image of nanotube forest with Pd and TiO2 deposited on opposite ends with the evaporation deposition method. Left shows close up of portions of the nanotube with EDX indicating Pd on the top, Ti on the bottom and negligible metal in the middle.

EDX showed significant evidence of block functionalization, as can be seen in Figure 41. The top of the forest shows a strong peak of Pd, exceeding even the carbon signal of the EDX, but no Ti. The bottom is the inverse, showing a strong Ti signal but no measurable Pd. The tips of the nanotubes exhibit a slight increase in the diameter, indicating a metal coating over the carbon. It should be noted the wt% recorded with EDX is not a total sample wt%. It is calculated by the number of X-rays detected from each atom, and the molecular weight of each species is used to convert the signal into a wt%. This method is heavily weighted towards the surface species over the bulk sample, with an undetermined interaction volume. Actual metal loading is calculated from a quartz crystal microbalance calibrated to the amount of metal laid down

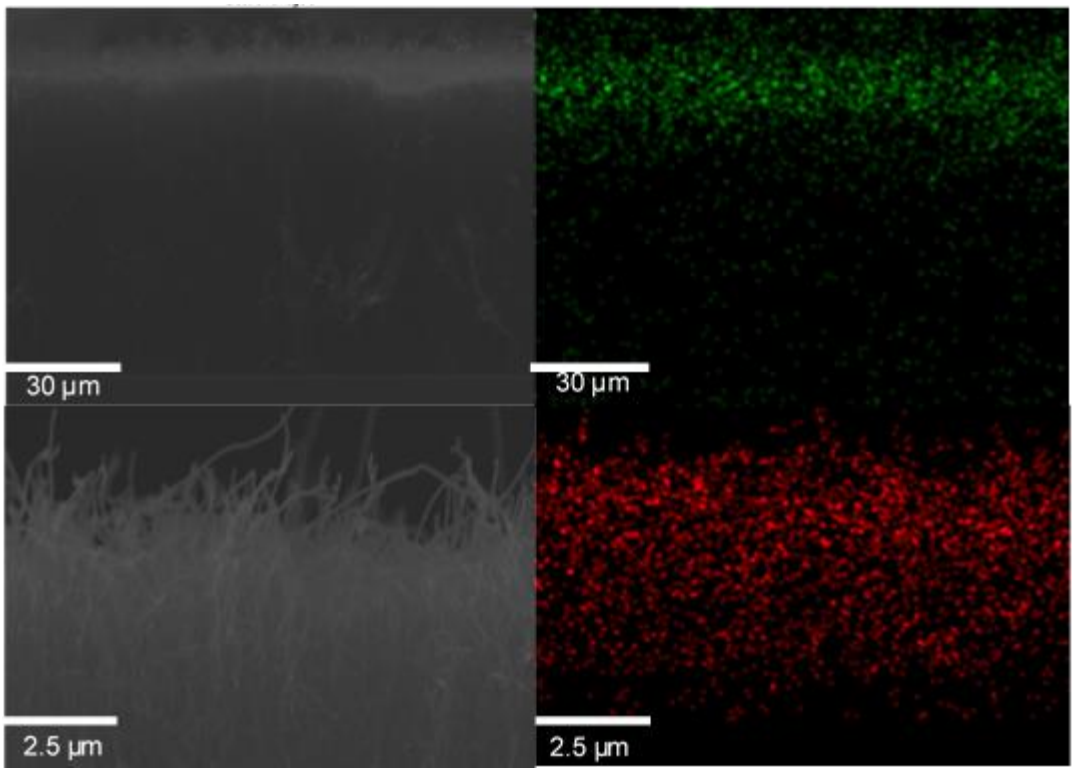

Figure 42:SEM (left) and EDX map (right) of copper evaporated onto the top of the nanotube forest, supported on a silica wafer. Top is the entire forest, with the bottom showing a close up of the tip of the forest.

on a blank silica wafer. EDX is however useful for providing mapping of the sample and identifying location of the products.

Copper was deposited onto one side of the forest for use as the oxide in hydrogen spillover studies, as well as the reducing metal in the anisole reactions. The EDX of copper was used to determine the penetration depth of a metal into the forest. The top of Figure 42 shows being identified in a strong band near the top of the forest, similar to the Pd and Ti study which identified metal only near the tip. A small amount of bremsstrahlung can be observed throughout the forest in the zoomed out image. No Cu was identified when the window was focused on the middle or base of the forest. When focused on the top of the forest the mapping indicate a heavy copper presence at the very tip,

which almost completely tapers off within about 6 microns, indicating the penetration depth of the metal is less than 10% of the forest height for the block functionalized nanotubes. This shows satisfactorily minimal penetration of the metal into the forest, meaning the two metals will not come in contact with each other initially. Reactions were performed at 400°C in hydrogen which could allow significant sintering of the particles. Pd and Cu were placed on opposite sides of the nanotube for spillover studies and reduced for 1 hour at reaction conditions, the results can be seen in Figure 43. Similar to Figure 41, when the Pd and Cu were placed on opposite sites EDX identified no discernable levels of metal in the middle of the nanotube forest, with high concentrations of copper and palladium at the top and bottom of the forest respectively. This shows the block functionalized CNTs were stable, leaving only the question of hydrogen

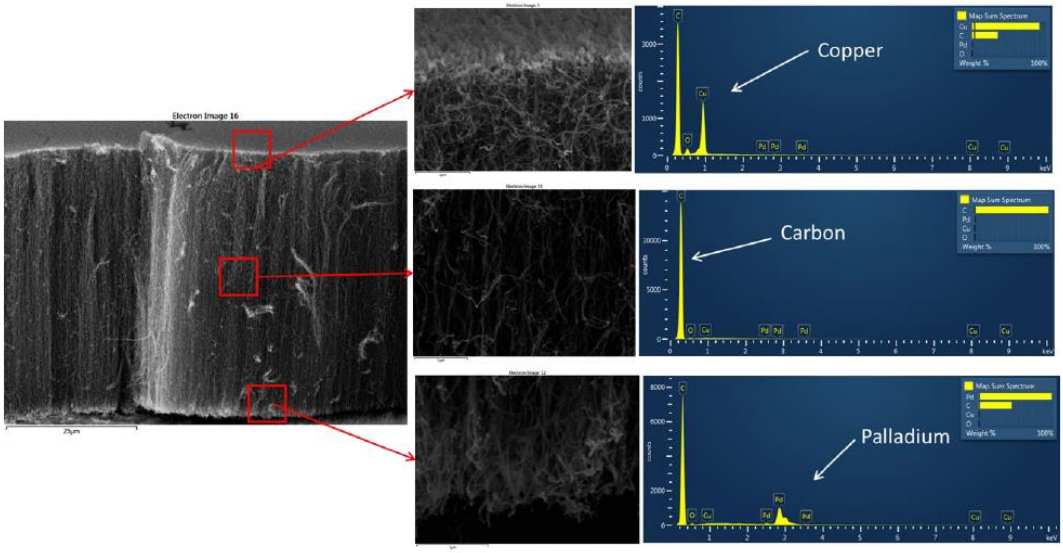

Figure 43: SEM with EDX of a Pd/CNT/CuO forest after treatment in hydrogen for 1 hour at 400°C.

spillover before they could be used for reactions. Catalyst loadings can be seen in Table 1.

Table 1: Metal loading on BF-CNT samples

Sample	Wt% Pd	Wt% Ti	Wt% Copper
Pd/CNT	0.29	N/A	N/A
TiO_2/CNT	N/A	0.60	N/A
CuO/CNT	N/A	N/A	1.01
Pd/TiO_2/CNT	0.29	0.76	N/A
Cu/TiO_2/CNT	N/A	0.69	1.05
Pd/CNT/TiO_2	0.24	0.66	N/A
Cu/CNT/TiO_2	N/A	0.67	1.00
Pd/CNT/CuO	0.26	N/A	1.01

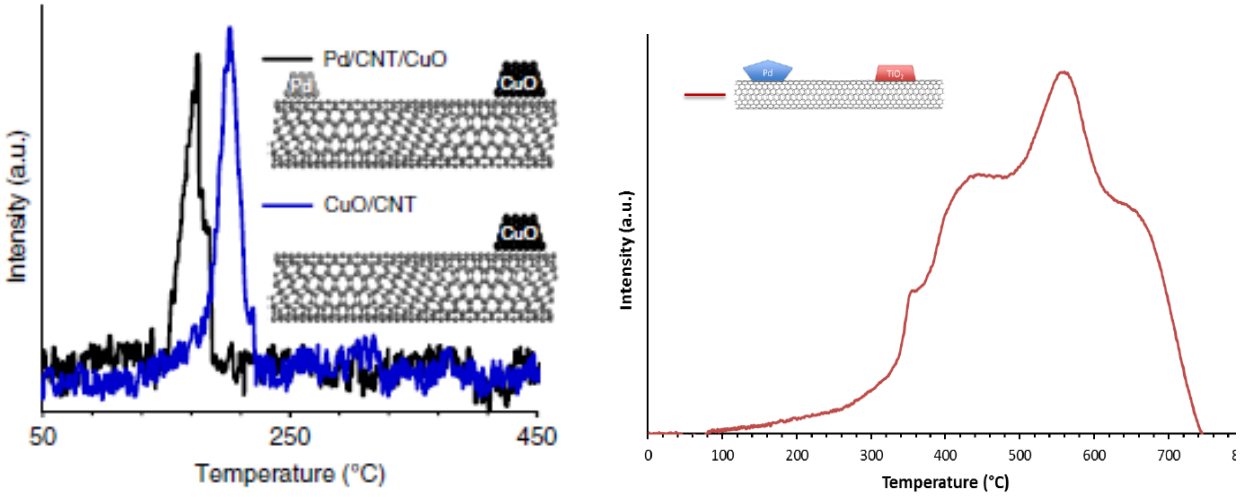

Figure 44: Top-TPR of CuO/CNT and Pd/CNT/CuO showing a clear shift to a lower temperature reduction in the palladium assisted case. Bottom- TPR of Pd/CNT/TiO2 Showing an onset of reduction near 300°C, 200°C before literature values.

Hydrogen Spillover

The first method used to show hydrogen spillover is a TPR of the nanotubes with a coper oxide and palladium reducing sites. This will be compared to a nanotube with only coper oxide deposited, no reducing metal assistance. The results of this test can be seen in Figure 44. The palladium assisted catalyst showed a 30°C shift in the temperature of reduction. This shift is more pronounced in titania which won't reduce until 500°C[176,183], and then will only reduce a small fraction. By comparison the palladium assisted case begins a clear reduction at 300°C. The 200 °C shift shows a clear spillover occurring to assist in the reduction of titania. It should be noted that TiO_2 only partially reduces, becoming a maximum of $TiO_{1.995}$[183].

XAS was performed on the Pd/CNT/CuO to determine the initial oxidation state of the copper, as well as the size of the particles before and after the reduction. Figure 45 Shows the results for copper, palladium was reduced in all cases. The samples were reduced at sequentially higher temperatures

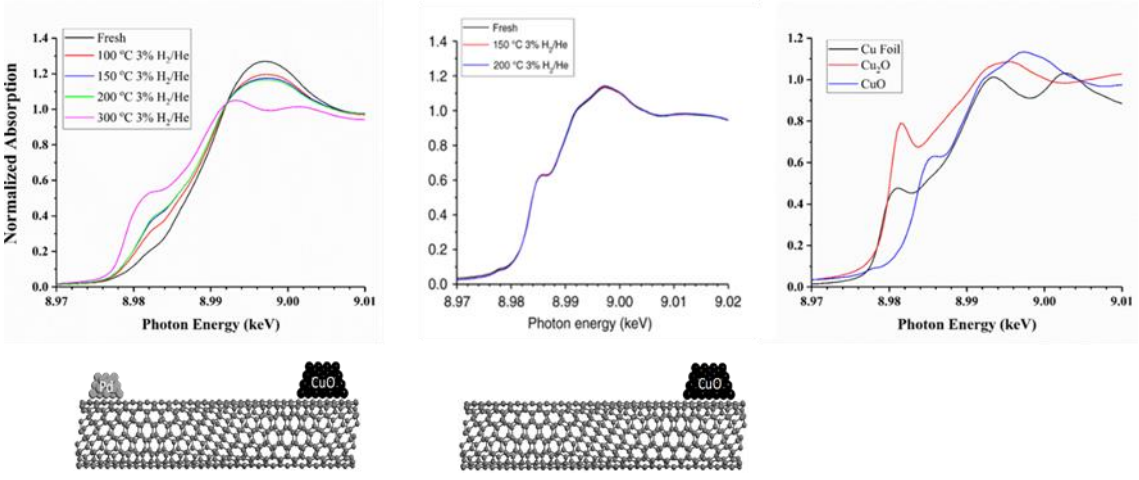

Figure 45: XAS of Left- palladium assisted copper reduction on BF-CNTs, Middle- unassisted copper and carbon nanotubes, Right- references for Cu(II), Cu(I), and Cu metal.

between measurements in a dilute hydrogen stream. Initially the copper was 75 at% Cu(II) 25 at% Cu(I) showing the calcination step used to convert the metal to an oxide was successful. In the palladium assisted case reduction started almost immediately, increasing the Cu(I) amount and eventually converting the sample to pure metal. The unassisted case showed no change up to 200°C. The lack of reduction below 200°C was confirmed by TGA of the copper sample using copper deposited on the nanotube through the evaporation method as well as physically mixed copper particles mixed with nanotubes in 3 mol% hydrogen, Figure 46. The final particle size for copper after reduction at 300°C was 1.5 nm.

Similar XAS tests were run with assisted and unassisted reduction of titania, but it was found the amount of titania that reduces is below the detection limit for Ti^{3+} of the equipment. It was found the initial sample was completely oxidized to Ti^{4+} and was entirely anatase nanoparticles, which were stable up to

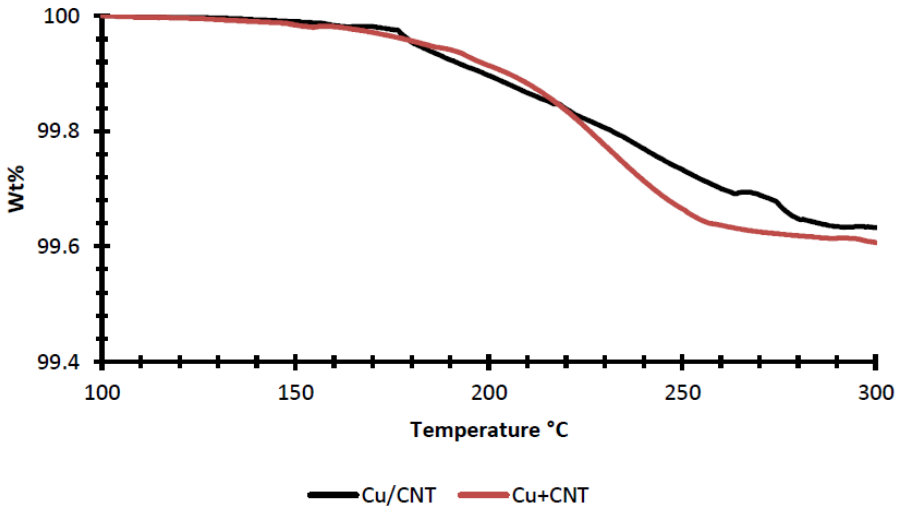

Figure 46: TGA in 3 mol% hydrogen in argon of Cu/CNT, with copper deposited on the nanotube forest via metal deposition and a physical mixture of copper (II) particles and nanotubes.

400°C. Upon further heating to 600°C a conversion to rutile was observed, with slightly larger nanoparticles.

The last proof of hydrogen spillover is the acetic acid ketonization reaction. This reaction is known to occur on the Ti^{3+}defects[170-172]. Furfural hydrodeoxygenation reactions do consume defects, so be cofeeding acetic acid and furfural across the separated Pd/CNT/TiO_2 catalyst, the acetone production can be used as a measure of the defects in the titania. This reaction can be seen in Figure 47. When the catalyst is composed of only TiO_2 on nanotubes some conversion is seen with an immediate drop off in reactivity as the Ti^{3+} sites are consumed. The Pd assisted case showed 5 times the initial rate for ketonization, with a much smaller drop in activity over lifetime of the reaction. The same total load of TiO_2 was used in both cases, and this reaction is not known to occur over Pd. This means the spillover of hydrogen from the Pd generated 5 times the number of active sites as the un assisted case, and these sites were continually regenerated as the furfural reaction consumed them.

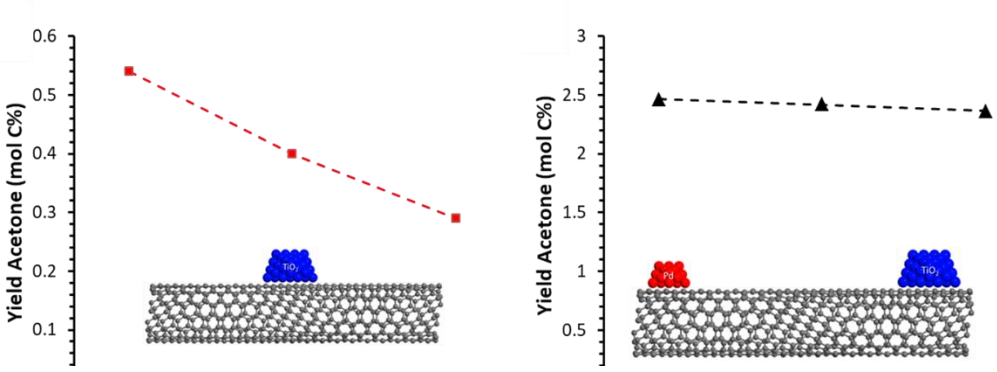

Figure 47: Acetic acid ketonization to acetone reaction results showing product yield as a function of time on stream (TOS). Left-TiO_2 supported on CNTs and Right Pd/CNT/TiO_2 showing an increased number of active sites for the ketonization reaction. Reaction at 400°C and 1 atm H_2

There are then three proofs that the hydrogen spillover can occur across the 90 microns of the nanotube and reduce the metal oxide. This is sufficient evidence for us to move onto the reactions and attempt to identify the active sites using the separated (metal/CNT/oxide) and stacked (metal/oxide/CNT) cases.

Active Site Identification

As discussed in the introduction of this chapter, there is debate as to the active site for the hydrodeoxygenation and decarboxylation reaction for furfural. It is known that placing a reducing metal on titania will increase the selectivity to the hydrodeoxygenation reaction, which yields a more valuable product, however some believe it is the interface between the metal and oxide[174] while others believe it is spillover which results in titania defects which are the active site[173]. Three catalysts were used in this method: palladium supported on

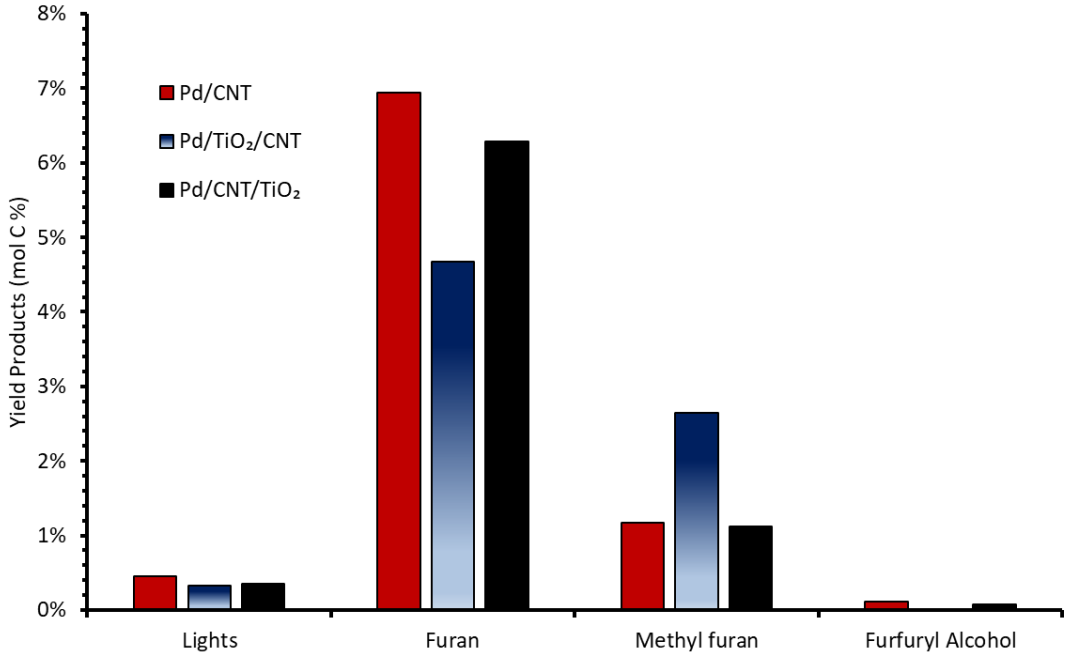

Figure 48: Furfural conversion over palladium, separated palladium titania, and stacked palladium titania all with CNT supports. Reaction conditions were 400°C, 1 atm H_2 flow, 30 minute TOS.

CNTs, Pd/CNT, palladium and titania on the opposite sides of a BF-CNT, Pd/CNT/TiO_2, and palladium and titania on the same side of the CNT, Pd/TiO_2/CNT. The results can be seen in Figure 48, the Pd/CNT and Pd/CNT/TiO_2 cases show almost identical selectivity to both furan and methyl furan. The separated case however shows nearly twice the methyl furan, indicating the active site for the hydrodeoxygenation reaction is the interfacial sites. It is still conceivable the number of defects generated in the TiO_2 is low enough to not show the increase in selectivity to the hydrodeoxygenation reaction, even though the acetic acid reaction showed a significant presence of the defects.

A second test using anisole conversion over Cu/TiO_2 based catalyst is used to test the ability of the catalyst to identify the active sites as a result of the promotor effects. In this case anisole converts through transalkylation to cresol or through dealkylation to phenol and methane. Again, three catalysts were used, though this time the control was a physical mixture of Cu on CNTs and TiO_2 on CNTs, along with the stacked and separated case. This was done to test the possibility that the metal could reduce the oxide despite being on a different tube, if the tubes or the metal and oxide were forced into contact in the packed bed. The results of the reaction can be seen in Figure 49. In this case the active site is strongly susspected to be the defect sites due to a similar reaction of guaiacol over titania[175,176]. The reaction occurs in both the seperated and stacked case as expected, however in the seperated case the reaction yields significantly higher conversion. This is thought to be due to the number of

Ti^{3+} sites which are covered up by the Pd in the stacked case. If spillover across the nanotube is sufficiently fast, the same general number of Ti^{3+} defects should be expected in the stacked and separated cases. With some of the stacked case's active sites covered by the Pd particles, the results would be expected as observed, with a higher conversionin the seperated case. This shows the ability of the system to idenify active sites due to promotor effects, and validates the results from the furfural reaction, as hydrogen spillover is shown to not be the limiting case. It should be noted that for this reaction the reducing metal was

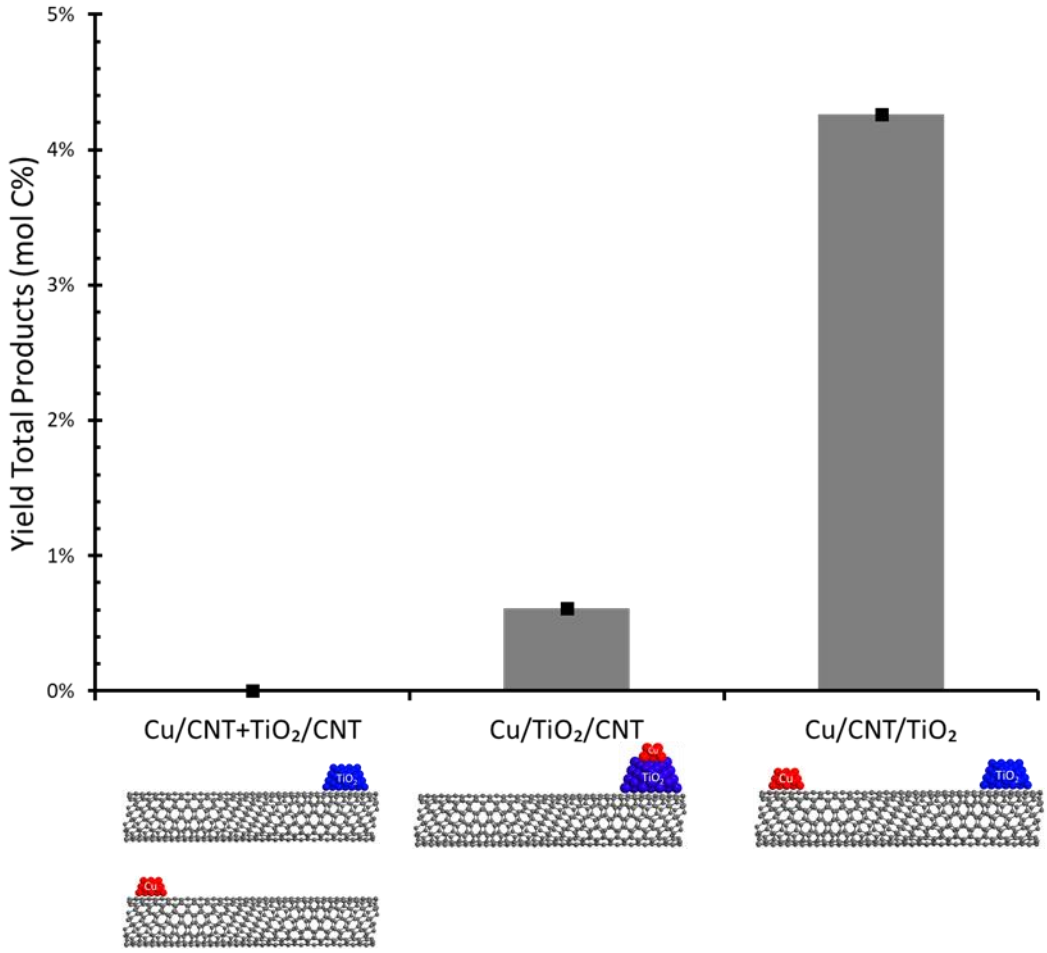

Figure 49: Anisole conversion over catalysts containing Cu and TiO2. Sum quantifiable products (cresol & phenol) resulting from anisole conversion over catalyst supported on CNTs in configurations shown. Reaction conditions were 400°C, 1 atm H2 flow, 30 minute TOS

changed from palladium to copper as palladium showed significant activity towards benzene production, at the detriment of other products.

The last reaction attempted is the ring rearrangement of furfural to cyclopentenone over Pd/TiO_2 catalyst supported on CNTs. This reaction is shown in Figure 50. Just like before the selectivity of furan and methyl furan exhibited a change when the catalyst was separated vs stacked, but more interestingly for this reaction no ring rearrangement products (cyclopentanone, 2-cyclopentenone) were observed in the separated case. If the results from the previous trial hold true, and there are more Ti^{3+} active sites in the separated case than the stacked case then the active site must be created by a physical contacting of the two species. Additionally, we know that the Pd isn't the active site itself by the absence of the ring rearrangement products on the separated case, so the active site must be in interface.

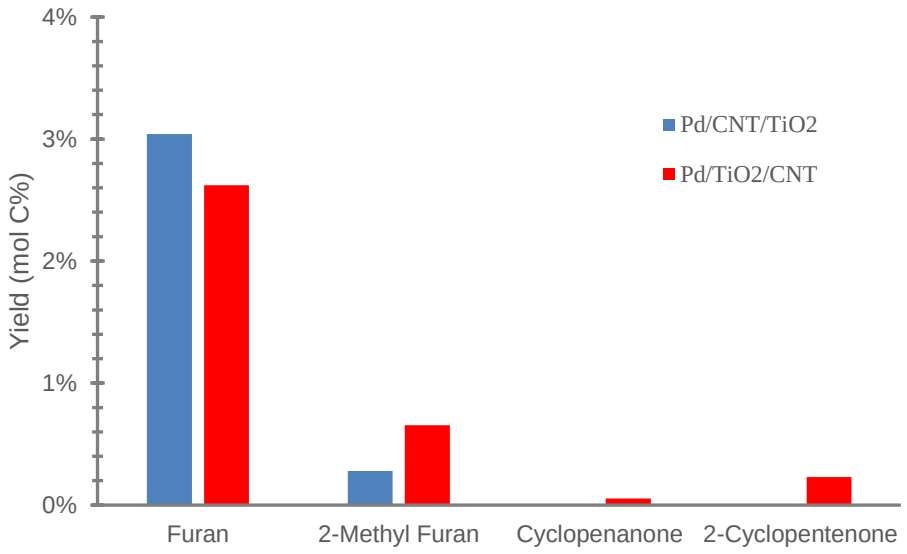

Figure 50: Furfural with water conversion over separated palladium titania and stacked palladium titania with CNT supports. Reaction conditions were 400°C, 1 atm H_2 flow, 30 minute TOS. Water to furfural ratio was 12:1.

Conclusion

The block functionalized nanotubes with the two components of a bifunctional catalyst have shown great promise for the identification of active sites in a minimal number of steps. Characterization of the nanotubes with TPR and XAS shows the nanotubes do exhibit hydrogen spillover across their substantial length, 90 microns, far larger than the spillover across non-conductive supports. The acetic acid ketonization reaction indicated the spillover was substantial enough to maintain a constant population of reduced sites on the oxide in the presence of a reaction which consumes defects. The anisole reaction actually showed the number of defects on the titania was greater in the separated case than the stacked case, indicating the spillover isn't a rate limiting step. The active site for all reactions was located, with the furfural hydrodeoxygenation and ring rearrangement reactions occurring at the Pd/TiO_2 interface, while the anisole dealkylation/transalkylation reactions occurred on the titania defects as expected. The block metal functionalized nanotube shows great promise as a method for determining the active site of various reactions on bifunctional catalysts, as well as being an interesting probe for the mechanism of hydrogen spillover across the nanotube. Further work will need to be done to study the rate of spillover as a function of surface defects and length to determine what effects the spillover has on the observed reaction rate.

Chapter 7: Conclusions

Nanotubes are a growing area of materials research, with recent work in anisotropic functionalized nanotubes. Nanotube forests were grown in between sheets of mica, allowing for a high surface area to weight ratio for the catalyst. These nanotubes were then purified by dissolving the mica into water soluble products, resulting in small forests of vertically aligned nanotubes separate from the catalyst being produced in a scalable manner for the first time. This can allow future work in mass production of highly uniform nanotubes without the need for HF acid. By changing the feedstock from acetonitrile to ethylene it was found the nanotube composition can be changed to be block functionalized with pyridine rings in the outer wall.

The pyridine rings allow for an NMR polymerization selective to either the pristine or nitrogen doped half of the nanotube by controlling the bond strength of the mediator group. Further tests will need to be performed but it may be possible to polymerize on both halves in a sequential manner to form a diblock nanotube, if the polymers can be terminated to prevent growth when exposed to the next monomer. The block functionalized nanotubes were able to increase the interfacial toughness of a PS/PMMA blend as determined by ADCB testing. By functionalizing both halves with the different polymers could further increase this interfacial toughness value by increasing the dispersion of the nanotubes as well as increasing the nanotubes affinity for each phase. Future work will take these measurements from a flat plane to being used in a polymer blend. The issue will be shortening the nanotubes such that they will not be subject to

significant breakages during the blending process. To this end work is being done on lower temperature growth temperatures and changing the nitrogen source from acetonitrile to ammonia to facilitate growth at the lower temperatures. Additional optimization should be done by controlling the concentration of nanotubes at the interface and changing the annealing temperatures.

A second type of BF-CNT was produced using two metals rather than polymer. This allowed the probing of a bifunctional catalyst by allowing the reaction to occur when the catalyst components are in direct contact and when they are spatially separated but electronically linked. Some reactions such as anisole dealkylation and transalkylation was found to occur in the defects of titania, which were produced by hydrogen spillover. This presents a unique opportunity, if a reaction which consumes the defects more quickly than they can be produced is used, then the hydrogen spillover becomes rate limiting and the effect of length, surface species, and diameter on spillover rate can be studied quantitatively.

An additional method to produce block functionalized nanotubes in a scalable manner being considered is to form an emulsion with nanotubes residing at the interface. By coalescing the drops the nanotubes may be ‘jammed’ into a smaller space so that they partially extend into each phase, where different chemistries can be done in each phase to functionalize the nanotubes. This has to potential to produce even shorter BF-CNTs and will be studied further.

References

1 Melissa Paradise, T. G. Carbon Nanotubes- Production and Industrial Applications. *Materials and Design* **28**, 1477-1489 (2007).

2 Iijima, S. Helical Microtubules of Graphitic Carbon. *Nature* **354**, 56-58 (1991).

3 Golnabi, H. Carbon nanotube research developments in terms of published papers and patens, synthesis and production. *Scientia Iranica* **19**, 2012-2022 (2012).

4 Kenneth K. S. Lau, J. B., Kenneth B. K. teo, Manish Chhowalla, Gehan A. J. Amaratunga, William I. Milne, Gareth H. McKinley, Karen K. Gleason. Superhydrophobic Carbon Nanotube Forests. *Nano Letters* **3** (2003).

5 K. ESUMI, M. I., A. NAKAJIMA, K. S AWADA, H. HONDA Chemical treatment of carbon nanotubes. *Carbon* **34**, 279-281 (1995).

6 Nadka Dintcheva, R. A., Rosalia Teresi, Bartolomeo Megna, Cristian Gambarotti, Salvatore Marulllo, Franscesca D'Anna. Tunable radical scavenging activity of carbon nanotubes through sonication. *Carbon* **107**, 240-247 (2016).

7 Ivana Fenoglio, M. T., Dominique Lison, Julie Muller, Antionio Fonseca, Janos Nagy, Bice Fubini. Reactivity of Carbon Nanotubes: Free radical generation or scavenging activity. *Free radical biology and medicine* **40**, 1227-1233 (2006).

8 Bumsu Kim, H. P., Wolfgang Sigmund. Electrostatic Interactions between shortened multiwalled carbon nanotubes and polyelectrolytes. *Langmuir* **19**, 2525-2527 (2003).

9 Scott Miller, V. Y., Charles Martin. Electroosmotic Flow in template-prepared carbon nanotube membranes. *JACS* **123**, 12335-12342 (2001).

10 Yu Zhao, M. H., Nadege Bonnet Mercier, Guihua Yu, He Cheul Choi, Hey Ryung Byon. a 3.5 V Lithium Iodine hybrid redox battery with vertically aligned carbon nanotube current collector. *Nano Letters* **14**, 1085-1092 (2014).

11 Min-Feng Yu, O. L., Mark Dyer, Katerina Moloni, Thomas Kelly, Rodney Rouff. Strength and Breaking Mechanism of Multiwalled Carbon Nanotubes Under Tensile Load. *Science* **287**, 637-640 (2000).

12 Chenyu Wei, K. C., Deepak Srivastava. Tensile strength of carbon nanotubes under realistic temperature and strain rate. *Physical Review B* **67**, 115407-115412 (2003).

13 Zhong Hu, X. L. in *Carbon Nanotubes and Graphene* (ed Elsevier) Ch. 8, 165-199 (2014).

14 M. Reibold, P. P., A. Levin, W. Kochmann, N. Patzke, D. Meyer. Carbon Nanotubes in Ancient Damascus Sabre. *Nature* **444**, 286 (2006).

15 Rodney Ruoff, J. T., Donald Lorents, Shekhar Subramoney, Bryan Chan. Radial Deformation of Carbon Nanotubes by van der Waals forces. *nature* **364**, 514-516 (1993).

16 I. Palaci, S. F., H. Brune, C. Klinke, M. Chen, E. Riedo. Radial Elasticity of Multiwalled Carbon Nanotubes. *Physical Review Letters* **94** (2005).

17 Thomas Gegenhuber, M. K., Judith Schöel, Andre Gröschel, Holger Schmalz. Patchy Carbon Nanotubes as Efficient Compatibilitiy for Polymer Blends. *ACS Macro Letters* **5**, 306-310, doi:10.1021/acsmacrolett.6b00033 (2016).

18 Chen Wei, L. D., Ajit Roy, Tia Benson Tolle. Multifunctional Chemical Vapor Sensors of Aligned Carbon Nanotube and Polymer Composites. *JACS Communications* **128**, 1412-1413 (2006).
19 Jiaxi Guo, N. B., Steven Crossley, Brian P. Grady. Morphology of Polystyrene/Poly(methyl methacrylate) Blends: Effects of Carbon Nanotubes Aspect Ratio and Surface Modification. *AIChE Journal* **61**, 3500-3510, doi:10.1002 (2015).
20 K. Lau, C. G., D. Hui. A critical review on nanotube and nanotube/nanoclay related polymer composite materials. *Composites: Part B* **37**, 425-436 (2006).
21 E. Bekyarova, Y. N., E. Malarkey, V. Montana, J. McWilliams, R. Haddon, V. Parpura. Applications of Carbon Nanotubes in Biotechnology and Biomedicine. *Journal of Biomedical Nanotechnology* **1**, 3-17 (2005).
22 Z. Hu, M. A., X. Yan, Q. Fan. Mechanical property characterization of carbon nanotube modified polymeric nanocomposites by computer modeling. *Composites: Part B* **56**, 100-108 (2014).
23 Y. Jung, S. K., S. Talapatra, C. Soldano, G. Viswanathan, X. Li, Z. Yao, F. Ou, A. Avadhanula, R. Vajtai, S. Curran, O. Nalamasu, P. Ajayan. Aligned carbon anotube polymer hybrid architectures for diverse flexible electronic applications. *Nano Letters* **6**, 413-418 (2005).
24 B. Hinds, N., Chopra, T. Rantell, R. Andrews, V. Gavalas, L. Bachas. Aligned multiwalled carbon nanotube membranes. *Science* **303**, 62-67 (2004).
25 J. Li, H. N., A. Cassell, W. Fan, H. Chen, Q. Ye, J. Koehne, J. Han, M. Meyyappan. Carbon Nanotube nanoelectrode array for ultrasensitive DNA detection. *Nano Letters* **3**, 597-602 (2003).
26 Kyung Min Lee, L. L., Liming Dai. Asymmetric End-Functionalization of Multi-Walled Carbon Nanotubes. *Journal of the American Chemical Society* **127**, 4122-4123 (2004).
27 Zhong Wei, M. K., Le H. Dao, Dmitrii F. Perepichka. Rectifying Diodes from Asymmetrically Functionalized Single-Wall Carbon Nanotubes. *JACS Communications* **128**, 3134-3135 (2005).
28 Liangti Qu, L. D. Polymer-masking for controlled functionalization of carbon nanotubes. *Chemical Communications* **2007**, 3859-3861, doi:10.1039/b707698c (2007).
29 Liangti Qu, L. D., Eiji Osawa. Shape/Size-Controlled Syntheses of Metal Nanoparticles for Site-Selective Modification of Carbon Nanotubes. *Journal of the American Chemical Society* **128**, 5523-5532 (2006).
30 N. Briggs, L. B., E. Wegener, L. Herrera, L. Gomez, J. Miller, S. Crossley. Identification of active sites on supported metal catalysts with carbon nanotube hydrogen highways. *Nature Communications*, 9:3827 (2018).
31 J. Dealy, J. W. *Melt Rheology and its applications in the plastics industry*. 2nd edn, (Springer Science, 1990).
32 H. R. Brown, K. C., V. R. Decline, P. F. Green. Effects of Diblock Copolymer on Adhesion between Immersible Polymers. 1. PS-PMMA Copolymer between PS and PMMA. *Macromolecules* **26**, 4155-4163 (1993).

33 B. Binks, P. F. Particles adsorbed at the oi-water interface- a theroetical comparison between spheres of uniform wettability and janus particles. *Langmuir* **17**, 4708-4710 (2001).
34 A. Walther, A. M. Janus Particles. *Soft Matter* **4**, 663-668 (2008).
35 Nicholas M. Briggs, J. S. W., Brian Li, Deepika Venkataramani, Clint P. Aichele, Jeffrey H. Harwell, Steven P. Crossley. Multiwalled Carbon Nanotubes at the Interface of Pickering Emulsions. *Langmuir* **31**, 13077-13084 (2015).
36 S. Crossley, J. F., M. Shen, D. Resasco. Solid Nanoparticles that Catalyze Biofuel Upgrade Reactions at the Water-Oil Interface. *Science* **327**, 68-74 (2010).
37 Min Shen, D. E. R. Emulsions Stabilized by Carbon Nanotube-Silica Nanohybrids. *Langmuir* **25**, 10843-10851 (2009).
38 Rajesh Purohit, K. P., Saraswati Rana, R. S. Rana, Vivek Patel. Carbon Nanotubes and Their Growth Methods. *Procedia Materials Science* **6**, 2014 (2014).
39 Mildred Dresselhaus, G. D., Phaedon Avouris. *Carbon Nanotubes synthesis, structure, properties, and applications*. (Springer, 2001).
40 N. Briggs, S. C. Rapid growth of vertically aligned multi-walled carbon nanotubes on a lamellar support. *RSC Advances* **5**, 83945-83953 (2015).
41 M. Glerup, M. C., M. Holzinger, G. Hug, A. Loiseau, P. Berneir. synthesis of highly nitrogen doped multiwalled carbon nanotubes. *Chemical Communications*, 2542-2543 (2003).
42 Dai, H. Carbon nanotubes: opportunities and challenges. *Surface Science* **500**, 218-241 (2008).
43 E. Nxumalo, N. C. Nitrogen doped carobn nanotubes from organometallic compounds: A review. *Materials and Design* **3**, 2141-2171 (2010).
44 A. Goheir, C. P. E., T. M. Minea, M. A. Djouadi. Carbon Nanotube growth mechanism switches from tip to base growth with decreasing catalysts particle size. *carbon* **46**, 1331-1338 (2008).
45 Hisashi Araki, H. K., Katsumi Yoshino. Growth of carbon nanotubes on quartz plats by chemical vapor deposition using (Ni, Fe)- Phthalocyanines. *Journal of Applied Physics* **38**, 836-838 (1999).
46 M Yudaska, R. K., Y. Ohki, S. Yoshimura. Nitrogen Containing carbon nanotube growth from Ni Phthalocyanine by chemical vapor deposition. *Carbon* **35**, 195-201 (1997).
47 V. Datsyuk, M. K., K. Papagelis, J. Parthenios, D. Tasis, A. Siokou, I. Kallitsis, C. Galiotis. Chemical Oxidation of Multiwalled Carbon Nanotubes. *Carbon* **46**, 833-840 (2008).
48 M. Zhao, Q. Z., J. Juang, F. Wei. Large scale intercalated growth of short aligned carbon nanotubes among vermiculite layers in a fluidized bed reactor. *Journal of Physics and Chemical Solids* **71**, 624-627 (2010).
49 Q. Zhang, M. Z., Y. Liu, A. Cao, W. Qian, U. Lu, F. Wei. Energy adsorbing hybrid composites based on alternate corbon nanotube and inorganic layers. *advanced materials* **21** (2009).

50 Q. Zhang, M. Z., J. Huang, Y. Liu, Y. Wang, W. Qian, F. Wei. vertically aligned carbon nanotube arrays grown on a lamellar catalyst by fluidied bed catalytic chemical vapor deposition. *carbon* **47**, 2600-2610 (2009).
51 C. Bower, A. K., Y. Wu, O. Zhou. Intercalation and partial exfoliation of single-walled carbon nanotubes by nitric acid. *Chemical Physics Letters* **288**, 481-486 (1998).
52 Birgitta E. Kalinowski, P. S. Rates and nonstoichiometry of vermiculite dissolution at 22°C. *Geoderma* **142**, 197-209 (2007).
53 Aoki, Y. K. Y. Dissolution process of phlogpite in ace solutions. *clays and clay minerals* **43**, 39-50 (1995).
54 Marta Valaskova, G. S. M. in *Clay Minerals in Nature- Their Characterization, Modification and Application* Ch. 11, 211-238 (2012).
55 E. Raymundo-Pinero, P. A., T. Cacciaguerra, D. Cazorla-Amoros, A. Linares-Solano, F. Beguin. KOH and NaOH activation mechanism of multiwalled carbon nanotubes with different structural organisation. *Carbon* **43**, 786-795 (2005).
56 Roman Brukh, S. M. Mechanism of carbon nanotube growth by cvd. *Chemical Physics Letters*, 126-132 (2006).
57 B. Stohr, H. B., R. Schlogl. Enhancement of the catalytic activity of activated carbons in oxidation reactions by thermal treatment with ammonia or hydrogen cyanide and observation of a superoxide species as a possible intermediate. *Carbon* **29**, 707-720 (1991).
58 C. Mangun, K. B., J. Economy, K. Foster. Surface chemistry, pre sizes and adsorption properties of carbon fibers and precoursors treated with ammonia. *Carbon* **39**, 1809-1820 (2001).
59 A. villa, J. T., O. Majoulet. D. Su, R. Schlogl. Transesterification of triglycerides using nitrogen functionalized carbon nanotubes. *chemsuschem* **3**, 241-245 (2010).
60 L. Mabena, S. R., S. Mhlanga, N. Coville. Nitrogen-doped carbon nanotubes as a metal catalysts support. *Applied Nanoscience*, 67-77 (2011).
61 Stephen Maldonado, S. M., Keith J. Stevenson. Structure, composition and chemical reactivity of carbon nanotubes by selective nitrogen doping. *Carbon* **44**, 1429-1437 (2006).
62 M. Santos, F. A. Nitrogen substitution of carbon in graphite, struture evolution towards molecular forms. *Physical Review B* **58**, 13918-13924 (1998).
63 S. Souto, M. P., M. C. dos Santos, and F. Alvarez. electronic structure of nitrogen-carbon alloys determined by photoelectron spectroscopy. *Physical Review B* **57**, 2536-2541 (1998).
64 Andriy H. Nevidomskyy, G. b. C. n., Michael C. Payne. Chemically Active Substitutional Nitrogen Impurity in Carbon Nanotubes. *Physical Review Letters* **91** (2003).
65 Q. Wei, X. T., G. Zhang, J. Qiao, Q. Gong, S. Sun. Nitrogen doped carbon nanotube and graphene materials for oxygen reduction reacions. *catalysts* **5**, 1574-1602 (2015).
66 Rongqing Yu, M. Z., Dadian Cheng, Shiyao Yang, Zhaoyang Liu, Lansun Zheng. Simultaneous synthesis of carbon nanotubes and nitrogen-doped

fullerenes in nitrogen atmosphere. *Journal of Physical Chemistry* **99**, 1818-1819 (1995).

67 K. Suenaga, M. Y., C. Colliex, S. Iijima. Radially Modulated Nitrogen Distribution in CNx nanotubular structures prepared by CVD using Ni phthalocyanine. *Chemical Physics Letters* **316**, 365-375 (2000).

68 L. G. Bulusheva, A. V. O., Yu. V. Fedoseeva, A. G. Kurenya, I. P. Asanoc, O. Y. Vilkov, A. A. Koos, N. Grobert. Controlling pyridinic, pyrrolic, graphitic, and molecular nitrogen in multi-wall carbon nanotubes using precursors with different N/C ratios in aerosol assisted chemical vapor deposition. *Phys. Chem. Chem. Phys.* **17**, 23741-23747 (2015).

69 Z. Ismagilov, A. S., O. Podyacheva, A. Ischenko, L. Kibis, A. Boronin, Y. Chesalov, D. Kochubey, A. romanenko, O. Anikeeva, T. Buryakov, E. Tkachev. Structure and electrical conductivity of nitrogen doped carbon nanofibers. *Carbon* **47**, 1922-1929 (2009).

70 G. Bepete, Z. T., S. Lindner, M. Rummeli, Z. Chiguvare, N. Coville. The use of aliphatic alcohol chain length to control the nitrogen type and content in nitrogen doped carbon nanotubes. *Carbon* **52**, 316-325 (2013).

71 H. Liu, Y. Z., R. Li, X. Sun, S. Desilets, H. About-Rachid, M. Jaidann, L. Lussier. Structural and morphological control of aligned nitrogen-doped carbon nanotubes. *Carbon* **48**, 1498-1507 (2010).

72 Antal A. Koos, M. D., Kerstin Jurkschat, Alison Crossley, Nicole Grobert. Effect of the experimental parameters on the structure of nitrogen doped carbon nanotubes produced by aerosol chemical vapour deposition. *Carbon* **47**, 30-37 (2009).

73 C. Ewels, M. G. A review of Nitrogen Doping in Carbon Nanotubes. *Journal of Nanoscience and Nanotechnology* **5**, 1345-1363 (2005).

74 M. Sacardamaglia, M. A., B. Llorente, P. Mudimela, J. Colomer, J. Ghijsen, C. Ewels, R. Snyder, L. Gregoratti, C. Bittencourt. Nitrogen ion casting on vertically aligned carbon nanotubes: Tip and sidewall chemical modification. *Carbon* **77**, 319-328 (2014).

75 T. Sharifi, F. N., H. Barzegar, C. Tai, M. Mazurkiewicz, A. Malolepszy, L. Stobinski, T. Wagberg. Nitrogen Doped muliwalled carbon nanotubes produced by CVD-correlating XPS and Raman spectroscopy for the study of nitrogen inclusion. *Carbon* **50**, 3535-3541 (2012).

76 Rosa Arrigo, M. H., Robert Schlogl, Dang Sheng Su. Dynamic surface rearrangement and thermal stability of nitrogen functional groups on carbon nanotubes. *Chemical Communications*, 4891-4893 (2008).

77 Bin Wang, L. T., Sokrates T. Pantelides. Introduction of nitrogen with controllable configuration into graphene via vacancies and edges. *Journal of Materials Chemistry A* **1**, 14927-14934 (2013).

78 I. Matanovic, K. A., M. Strand, M. Dzara, S. Pylypenko, P. Atanassov. Core level shifts of hydrogenated pyridinic and pyrrolic nitrogen in the nitrogen containing graphene based electrocatalysts: in plane vs edge defects. *Journal of Physical Chemistry* **120**, 29225-29232 (2016).

79 L. Bulusheva, A. O., A. Kudashov, N. Yudanov, E. Paxhetnov, A. Boronin, O. Abrosimov, N. Rudina. Flourination of multiwall nitrogen doped carbon nanotubes. *Russian Journal of inorganic chemistry* **51**, 613-618 (2006).

80 D. Srivastava, M. M., C. Daraio, S. Jin, B. Sadanadan, A. Rao. Vacancy-mediated mechanism of nitrogen substitution in carbon nanotubes. *Physical Review B* **69**, 153414 (2004).

81 T. Schiros, D. N., L. Palova, D. Prezzi, L. Zhao, K. Kim, U. Wurstbauer, C. Gutierrez, D. Delongchamp, C. Jaye, D. Fischer, H. Ogasawara, L. Pettersson, D. Reichman, P. Kim, M. Hybertsen, A. Pasupathy. Connecting dopant bond type with electronic structures in N-doped graphene. *Nano Letters* **12**, 4025-4031 (2012).

82 M. Endo, K. T., S. Igarashi, K. Kobori, M. Shiraishi, H. Krotos. The production and structure of pyrolytic carbon nanotubes (PCNTs). *Journal of Physics and Chemical Solids* **54**, 1841-1848 (1993).

83 M. Terrones, A. B., C. Mateca-Diego, W. Hsu, O. Osman, J. Hare, D. Reid, H. Terrones, A. Cheetham, K. Prassides, H. Kroto, D. Walton. Pyrolytically grown BxCyNz nanomaterials: nanofibres and nanotubes. *Chemical Physics Letters* **257**, 576-582 (1996).

84 J. O'Byrne, Z. L., S. Jones, P. Fleming, J. Larsson, M. Morris, J. Holmes. Nitrogen-doped carbon nanotubes: growth, mechanism and structure. *ChemPhysChem* **12**, 2995-3001 (2011).

85 D. Ganguly, R. S., K. Ramanujam. chemical vapor deposition grown nickel encapuslated n-doped carbon nanotubes as a highly active oxygen reduction reaction catalysts without direct metal-nitrogen coordination. *ACS Omega* **3**, 13609-13620 (2018).

86 N. Perez, E. M.-S., , P. Diaz-Flores, J. Rangel-Mendez. Adsorption of cadmium and lead onto oxidized nitrogen-doped multiwall caron nanotubes in aqueous solutions: Equilibruim and kinetics. *Journal of Nanoparticle Research* (2009).

87 R. Dileo, B. L., R. Raffaelle. Purity assesment of multiwalled carbon nanotubes by raman spectroscopy. *Journal of Applied Physics* **101** (2007).

88 L. Bokobza, J. Z. Raman spectroscopic characterization of multiwall carbon nanotubes and of composites. *Polymer Letters* **6**, 601-608 (2012).

89 M. Zdrojek, C. J., W. Gebcki. Studies of multiwall carbon nanotubes using raman spectroscopy and atomic force microscopy. *Solid state phenomenon* **99** (2004).

90 M. Dresselhaus, G. D., R. Satio, A. Jorio. Raman spectroscopy of carbon nanotubes. *Physics Reports* **409**, 47-99 (2005).

91 Z. Zafar, Z. N., X. Wu, Z. Shi, H. Nan, J. Bai, L. Sun. Evolution of raman spectra in nitrogen doped graphene. *Carbon* **61**, 57-62 (2013).

92 R. Droppa, C. R., A. Zanatta, M. dos Santos, F. alvarez. Comprehensive spectroscopic study of nitrogenated carbon nanotubes. *Physical Review B* **69**, 045405 (2004).

93 L. Qu, L. D. *Chemistry of Carbon Nanotubes*. Vol. 2 (American Scientrific publishers, 2008).

94 S. Qin, D. Q., W. Ford, D. Resasco, J. Herrera. Functionalization of single-walled carbon nanotubes with polystyrene via grafting to and grafting from methods. *Macromolecules* **37**, 752-757 (2004).
95 E. Mickelson, C. H., A. Rinzler, R. Smalley, R. Hauge, J. Margave. Fluorination of single-wall carbon nantoubes. *Chemical Physics Letters* **296**, 188-194 (1998).
96 A. Hamwi, H. A., S. bonnamy, F. Beguin. Fluorination of carbon nanotubes. *Carbon* **35**, 723-728 (1997).
97 K. Balasubramanian, M. B. Chemically functionalized carbon nanotubes. *small* **1**, 180-192 (2005).
98 T. Hayashi, M. T., C. Scheu, Y. Kim, M. Ruhle, T. Nakajima, M. Endo. Nanoteflons: Structure and EELS Characterization of fluorinated carbon nanotubes and nanofibers. *Nano Letters* **2**, 491-496 (2002).
99 N. Yudanov, A. O., Y. Shubin, L. Yudanova, L. Bulusheva. Fluorination of arc produced carbon material containing multiwall nanotubes. *Chemistry of Materials* **14**, 1472-1476 (2002).
100 Liu, P. Modification of carbon nanotubes with polymers. *European Polymer Journal* **41**, 2693-2703 (2005).
101 C. Dwyer, M. G., M. Falvo, S. Washburn, R. Superfine, D. Erie. DNA-functionalized single-walled carbon nanotubes. *Nanotechnology* **13**, 601-604 (2002).
102 B. Hosangadi, R. D. An efficient general method for esterification of aromatic carboxylic acids. *Tetrahedron Letters* **35**, 6375-6378 (1996).
103 Grady, B. P. *Carbon Nanotub-Polymer composites: Manufacture, Properties, and Applications*. (Wiley, 2011).
104 D. Baskaran, J. M., M. Bratcher. Polymer-grafted multiwalled carbon nannotubes through surface initiated polymerization. *Angewandte Chemie* **43** (2004).
105 S. Osswald, M. H., Y. Gogotsi. Monitoring oxidation of multiwalled carbon nanotubes by Raman spectroscopy. *Journal of Raman Spectroscopy* **38**, 728-736 (2007).
106 F. Aviles, J. C.-R., L. Moo-Tah, A. May-Pat, R. Vargas-Coronado. Evaluation of mild acid oxidation treatments for MWCNT functionalizaiton. *Carbon*, 2970-2975 (2009).
107 Y. Miyata, Y. M., H. Kataura. Selective Oxidation of Semiconducting Single-Wall Carbon Nanotubes by Hydrogen Peroxide. *Journal of Physical Chemistry B* **110**, 25-29 (2005).
108 K. Voitko, R. W. V. G. k., O. Bakalinska, M. Kartel, K. Laszlo, A. Cundy, S. Mikhalovsky. Morphological and chemical features of nano and macroscale carbons affecting hydrogen peroxide decomposition in aqueous media. *Journal of Colloid and Interface Science* **361**, 129-136 (2011).
109 G. Viswanathan, N. C., H. Yang, B. Wei, H. Chung, K. Cho, C. Ryu, P. Ajayan. Single-Step in Situ Synthesis of Polymer-Grafted Single-Wall Nanotube Composites. *Journal of the American Chemical Society* **125** (2003).
110 J. Albuerne, A. B.-d.-F., V. Abetz. Modification of multiwall carbon nanotubes by grafting from controlled polymerization of styrene: effect of the

characteristics of the nanotubes. *Journal of Polymer Science: Part B: Polymer Physics* **48**, 1035-1046 (2010).
111 M. Dehonor, K. M.-V., A. Gonzalez-Montiel, C. Gauthier, J. Y. Caville, H. Terrones, M. Terrones. Nanotube brushes: polystyrene grafted covalently on CNx nanotubes by nitroxide-mediated radical polymerization. *Chemical Communications*, 5349-5351 (2005).
112 X. Zhao, X. F., X. Chen, C. Chai, Q. Zhou. Surface modification of multiwalled carbon nanotubes via nitroxide-mediated radical polymerization. *Wiley Interscience* (2006).
113 J. Chang, Y. L., B. Kim, H. Kim, I. Choi, H. Paik. Covalent attachment of polystyrene on multi-walled carobn nanotubes via nitroxide mediated polymerization. *Composites Interfaces* **14**, 493-504 (2012).
114 H. Kong, C. G., D. Yan. Controlled Functionalization of multiwalled carbon nanotubes by in situ atom transfer radical polymerization. *Journal of the American Chemical Society* **126**, 412-413 (2003).
115 J. Nicolas, Y. G., C. Lefay, D. Bertin, D. Gigmes, B. Charleux. Nitroxide-mediated polymerization. *Progess in Polymer Science* **38**, 63-235 (2013).
116 M. O'Connell, P. B., L. Ericson, C. Huffman, Y. Wang, E. Haroz, C. Kuper, J. Tour, K. Ausman, R. Smalley. Reversible water solubilization of single walled carbon nanotubes by polymer wrapping. *Chemical Physics Letters* **342**, 265-271 (2001).
117 A. Liu, I. H., M. Ichihara, H. Zhou. Poly(acrylic acid)- wrapped multi walled carbon nanotubes composite solubilization in water: definitve spectroscopic properties. *Nanotechnology* **17**, 2845-2849 (2006).
118 T. Gujigaya, N. N. Non-covalent polymer wrapping of carbon nanotubes and the role of wrapped polymers as functional dispersants. *Science and Technology of Advanced Materials* **16**, 24802-24823 (2015).
119 T. Swift, L. S., M. Geoghegan, S. Rimmer. The pH-responsive behaviour of poly(acrylic acid) in aqueous solution is dependent on molar mass. *Soft matter* **12**, 2542-2550 (2016).
120 Y. Peng, H. L. Effects of oxidation by hydrogen peroxide on the structures of multiwalled carbon nanotubes. *Industrial Engineering Chemistry research* **45**, 6483-6488 (2006).
121 Costantino Creton, E. K., Chung-Yuen Hui, Hugh Brown. Failure mechanisms of polymer interfaces reinforced with block copolymers. *Macromolecules* **25**, 3075-3088 (1992).
122 Brian Bernard, H. B., Craig Hawker, Andrew Kellock, Thomas Russell. Adhesion of Polymer Interfaces Reinforced with Random and Diblock Copolymers as a Function of Geometry. *Macromolecules* **32**, 6254-6260 (1999).
123 C. W. Macosko, P. G., Ashish K. Khandpur, Akinari Nakayama, Philippe Marechal, Takashi Inoue. Compatibilizers for Melt Blending: Premade Block Copolymers. *Macromolecules* **29**, 5590-5598 (1996).
124 Sabu Tomas, R. E. P. h. Compatibilizing effects of block copolymers in heterogeneous polystyrene/poly(methylmethacrylate) blends. *Polymer* **33**, 4260-4268 (1991).

125 Yoichiro Mori, L. S. L., Frank S. Bates. Consequences of molecular bridging in lamellae-forming triblock/pentablock copolymer blends. *Macromolecules* **36**, 9879-9888 (2003).
126 R. Fayt. R. Jerome, P. T. Molecular design of multicomponent polymer systems. Comparative behavior of pure and tapered block copolymers in emulsification of blends of low density polyethylene and polystyrene. *Journal of Polymer Science: Part B: Polymer Physics* **20**, 2209-2217 (1982).
127 P. Knaub, Y. C., J. Gerard. New reactive polymer blends based on poly(urethane-ureas) (PUR) and polydisperse polydimethylsiloxane (PDMS) and polydisperse polydimethylsiloxane (PDMS): control of morphology using a PUR-b-PDMS block copolymer. *Polymer* **29**, 1365-1378 (1988).
128 K. Letchford, H. B. A review of the formation and classification of amphiphilic block copolymer nanparticulate structures: micelles, nanospheres, nanocapsules and polymersomes. *European Journal of Pharmaceutics and BioPharmaceutics* **65**, 259-269 (2007).
129 M. E. Vigild, C. C., M. Sugiyama, K. A. Chaffin, F. S. Bates. Influence of shear on the alignment of a lammelae-forming pentablock copolymer. *Macromolecules* **34**, 951-964 (2000).
130 Thomas Gegenhuber, A. G., tina Lobling, Markus Drechsler, Sascha Ehlert, Stephan Forester, Holger Schmalz. Noncovalent Grafting of Carbon Nanotubes with Triblock Terpolymers: Toward Patchy 1D Hybrids. *Macromolecules* **48**, 1767-1776 (2015).
131 Z. Wang, M. S., S. Meikle, R. Whitby, S. Mikhalovsky. The surface acidity of acid oxidised multi-walled carbon nanotubes and the influence of in-situ generated fulvic acids on their stability in aqueous dispersions. *Carbon* **47**, 73-79 (2009).
132 D. Yang, X. Z., C. Wang, Y. Tang, J. Li, J. Hu. Preparation of water soluble multiwalled carbon nanotubes by Ce(IV)-induced redox radical polymerization. *Natural Sciences* **19**, 991-996 (2009).
133 P. Dubey, D. M. S. D., R. Mukhopadhyay, S. Sarkar. Synthesis and characterization of water-soluble carbon nanotubes from mustard soot. *Journal of Physics* **65**, 681-698 (2005).
134 H. Zhang, H. L., H. Cheng. Water-soluble multiwalled carbon nanotubes functionalized with sulfonated polyaniline. *Journal of Physical Chemistry B* **110**, 9095-9099 (2006).
135 FangFang Tao, B. N., Anne-Christine Baudouin, Jean-Michel Thomassin, Daniela Vuluga, Christophe Detrembleur, Christian Bailly. Influence of nanoparticle-polymer interactions on the apparent migration behavior of carbon nanotubes in an immiscible polymer blend. *Polymer* **52**, 4798-4805 (2011).
136 P. Charalambides, H. C., J. Lund, A. Evans. Development of a test method for measuring the mixed mode fracture resistance of mibaterial interfaces. *Mechanics of Materials* **8**, 269-283 (1990).
137 Brown, H. Mixed-mode effects on the toughness of polymer interfaces. *Journal of Materials Science* **25**, 2791-2794 (1990).
138 Kanninen, M. An augmented double cantileaver beam model for studying crack propagation and arrest. *International Journal of Fracture* **9**, 83-93 (1973).

139 J. Guo, Y. L., R. Prady-Silvy, Y. Tan, S. Azad, B. Krause, P. Potschke, B Grady. Aspect ratio effects of multi-walled carbon nanotubes on electrical, mechanical, and thermal properties of polycarbonate/MWCNT composites. *Journal of Polymer Science: Part B: Polymer Physics* **52**, 73-83 (2014).
140 Briggs, N. *Carbon Nanotubes as Catalyst Supports in Biphasics Systems* PhD thesis, University of Oklahoma, (2016).
141 B. Hammer, J. N. Why gold is the noblest of all metals. *Nature* **376**, 23-240 (1995).
142 J. Norskov, F. A.-P., F. Studt, T. Bligaard. Density functional theory in surface chemistry and catalysis. *Proceedings of the National Academy of Sciences of the United States of America* **108**, 937-943 (2010).
143 Held, G. The interplay bewteen geometry, electronic structure, and reactivity of the Cu-Ni bimetallic (111) surfaces. *Applied Physics A* **76**, 689-700 (2003).
144 Sachtler, W. The Second Rideal Lecture. What makes a catalyst selective? *Faraday Discussions of the Chemical Society* **72**, 7-32 (1981).
145 H. Idriss, M. B. Active sites on oxides: From single crystals to catalysts. *Advances in Catalysis* **45**, 261-331 (2000).
146 I. Chorkendorff, J. N. *Concepts of Modern Catalysis and Kinetics*. (John Wiley & Sons, 2006).
147 M. Cargnello, V. D.-N., T. Gordon, R. Diaz, E. Stach, R. Gorte, P. Fornasiero, C. Murray. Control of Metal Nanocrystal Size Reveals Metal-Support Interface Role for Ceria Catalysts. *Science* **341**, 771-773 (2013).
148 T. Komaya, A. B., Z. Wengsieh, T. Gronsky, F. Engelke, T. King, M. Pruski. Effects of Dispersion and Metal-Metal Oxide Interactions on Fischer-Tropsch Synthesis over Ru/TiO2 and TiO2-Promoted Ru/SiO2. *Journal of Catalysis* **150**, 400-406 (1994).
149 T. Omotoso, B. B., L. Grabow, S. Crossley. Experimental and First-Principles Evidence for Interfacial Activity of Ru/TiO2 for the Direct Conversion of m-Cresol to Toluene. *ChemCatChem* **9**, 2642-2651 (2017).
150 D. Resasco, G. H. A model of metal-oxide support interaction for Rh on TiO2. *Journal of Catalysis* **82**, 279-288 (1983).
151 G. Kennedy, L. B., G. Somorjai. Selective Amplification of C=O Bond Hydrogenation on Pt/TiO2: Catalytic Reaction and Sum-Frequency Generation Vibrational Spectroscopy Studies of Crotonaldehyde Hydrogenation. *Angewandte Chemie* **53**, 3405-3408 (2014).
152 M. Primet, M. M., W. Sachtler. Infrared spectra of carbon monoxide adsorbed on silica-supported PdAg alloys. *Journal of Catalysis* **44**, 324-327 (1976).
153 G. Haller, D. R. Metal–Support Interaction: Group VIII Metals and Reducible Oxides. *Advances in Catalysis* **36**, 173-235 (1989).
154 E. Zhao, H. Z., K. Ludden, Y. Xin, H. Hagelin-Weaver, C. Bowers. Strong Metal–Support Interactions Enhance the Pairwise Selectivity of Parahydrogen Addition over Ir/TiO2. *ACS Catalysis* **6**, 974-978 (2016).
155 S. Tauster, S. F., R. Garten. Strong metal-support interactions. Group 8 noble metals supported on titanium dioxide. *Journal of the American Chemical Society* **100**, 170-175 (1978).

156 Tauster, S. Strong Metal-Support Interactions. *Accounts of Chemical Research* **20**, 87-93 (1987).
157 Prins, R. Hydrogen Spillover. Facts and Fiction. *Chemical Reviews* **112**, 2714-2738 (2012).
158 X. Sha, M. K., A. Cooper, G. Pez, H. Cheng. Dynamics of hydrogen spillover on carbon-based materials. *The Journal of Physical Chemistry C* **112**, 17465-17470 (2008).
159 P. Singh, M. K., S. Gokhale, S. Chikkali, C. Kulkarni. Enhancing the hydrogen storage capacity of Pd-functionalized multi-walled carbon nanotubes. *Applied Surface Science* **258**, 3405-3409 (2012).
160 A. Nikitin, X. L., Z. Zhang, H. Ogasawara, H. Dai, A. Nilsson. Hydrogen storage in carbon nanotubes through the formation of stable C-H bonds. *Nano Letters* **8**, 162-167 (2008).
161 L. Wang, F. Y., R. Yang. Effect of surface oxygen groups in carbons on hydrogen storage by spillover. *Industrial Engineering Chemistry research* **48**, 2920-2926 (2009).
162 G. Psofogiannaki, G. F. DFT Study of Hydrogen Storage by Spillover on Graphite with Oxygen Surface Groups. *Journal of the American Chemical Society* **131**, 15133-15135 (2009).
163 L. Chen, A. C., P. Guido, H. Cheng. Mechanistic Study on Hydrogen Spillover onto Graphitic Carbon Materials. *Journal of Physical Chemistry: C* **111**, 18995-19000 (2007).
164 R. Bhowmick, S. R., D. Friebel, C. Beasley, L. Jaio, H. Ogasawara, H. Dai, B. Clemens, A. Nilsson. Hydrogen Spillover in Pt-Single-Walled Carbon Nanotube Composites: Formation of Stable C−H Bonds. *Journal of the American Chemical Society* **133**, 5580-5586 (2011).
165 A. Cao, H. Z., X. Zhang, X. Li, D. Ruan, C. Xu, B. Wei, J. Liang, D. Wu. Hydrogen storage of dense-aligned carbon nanotubes. *Chemical Physics Letters* **342**, 510-514 (2001).
166 S. Han, H. K., N. Park. Effect of shuttling catalyst on the migration of hydrogen adatoms: a strategy for the facile hydrogenation of graphene. *The Journal of Physical Chemistry C* **115**, 24696-24701 (2011).
167 J. Achtyl, R. U., J. Xu, Y. Cai, M. Raju, W. Zhang, R. Sacci, I. Vlassiouk, P. Fulvio, P. Ganesh, D. Wesolowski, S. Dai, A. van Duin, M. Neurock, F. Geiger. Aqueous proton transfer across single-layer graphene. *Nature Communications* **6** (2015).
168 A. Lachawiec, G. Q., R. Yang. Hydrogen storage in nanostructured carbons by spillover: bidge-building enchancement. *Langmuir* **21**, 11418-11424 (2005).
169 P. Mitcchell, A. R.-C., S. Parker, J. Tomkinson, D. Thompsett. Hydrogen spillover on carbon-supported metal catalysts studied by inelastic neutron scattering. Surface vibrational states and hydrogen riding modes. *Journal of physical Chemistry B* **107**, 6838-6845 (2003).
170 T. Pham, T. S., S. Crossley, D. Resasco. Ketonization of Carboxylic Acids: Mechanisms, Catalysts, and Implications for Biomass Conversion. *ACS Catalysis* **3**, 2456-2473 (2013).

171 T. Pham, D. S., D. Resasco. Kinetics and Mechanism of Ketonization of Acetic Acid on Ru/TiO2 Catalyst. *Topics in Catalysis* **57**, 706-714 (2013).
172 T. Pham, D. S., T. Sooknoi, D. Resasco. Aqueous-phase ketonization of acetic acid over Ru/TiO2/carbon catalysts. *Journal of Catalysis* **295**, 169-178 (2012).
173 L. Baker, G. K., M. Spronsen, A. Hervier, X. Cai, S. Chen, L. Wang, G. Somorjai. Furfuraldehyde Hydrogenation on Titanium Oxide-Supported Platinum Nanoparticles Studied by Sum Frequency Generation Vibrational Spectroscopy: Acid–Base Catalysis Explains the Molecular Origin of Strong Metal–Support Interactions. *Journal of the American Chemical Society* **134**, 14208-14216 (2012).
174 J. Zhang, B. W., E. Nikolla, J. Medlin. Directing Reaction Pathways through Controlled Reactant Binding at Pd–TiO2 Interfaces. *Angewandte Chemie* **56**, 6594-6598 (2017).
175 T. Omotoso, S. B., S. Crossley. Understanding the role of TiO2 crystal structure on the enhanced activity and stability of Ru/TiO2 catalysts for the conversion of lignin-derived oxygenates. *Green Chemistry* **16**, 645-652 (2014).
176 S. Boonyasuwat, T. O., D. Resasco, S. Crossley. Conversion of guaiacol over supported Ru catalysts. *Catalyst Letters* **143** (2013).
177 M. Hronec, K. F., M. Micusik. Influence of furanic polymers on selective furfural rearrangement to cyclopentanone. *Applied Catalysis A: General* **468** (2013).
178 M. Hronec, K. F., T. Liptaj. Effect of catalyst and solvent on the furan ring rearrangement to cyclopentanone. *Applied Catalysis A: General* **437**, 104-111 (2012).
179 M. Hronec, K. F. Selective transformation of furfural to cyclopentanone. *Catalyst Communications* **24**, 100-104 (2012).
180 M. Hronec, K. F., I. Vavra, T. Sotak, E. Dobrocka, M. Micusik. Carbon supported Pd-Cu catalysts for highly selective rearrangment of furfural to cyclopentanone. *Applied Catalysis B: Enviornmental* **181**, 210-219 (2016).
181 Ressier, T. WinXAS: a Program for X-ray Absorption Spectroscopy Data Analysis under MS-Windows *Journal of Synchrotron Radiation* **5**, 118-122 (1998).
182 A. Nikitin, Z. Z., A. Nilsson. Energetics of C-H bonds formed at single-walled carbon nanotubes. *Nano Letters* **9**, 1301-1306 (2009).
183 J. Rekoske, M. B. Isothermal Reduction Kinetics of Titanium Dioxide-Based Materials. *Journal of Physical Chemistry: B* **101**, 1113-1124 (1997).
184 Jimmy Faria, M. P. R., Daniel Resasco. Phase-Selective Catalysis in Emulsions Stabilized by Janus Silica-Nanoparticles. *Advanced synthesis and catalysis* **352**, 2359-2364 (2010).
185 santiago Drexler, J. F., M. Pilar Ruiz, Jeffrey Harwell, Daniel Resasco. Amphilic nanohybrid catalysts for reactions at the water oil interface in subsurface reservoirs. *Energy and Fuels* **26**, 2231-2241 (2012).
186 Shan Jiang, S. G. Controlling the Geometry of amphiphilic colloidal particles. *Langmuir* **24**, 2438-2445 (2008).

187 Adeline Perro, S. R., Serge Ravaine, Elodie Bourgeat-Lami, Etienne Duguet. Design and synthesis of Janus micro- and nanoparticles. *Journal of materials Chemistry* **15**, 3745-3760 (2005).
188 J. Giermanska-Kahn, V. L., S. Arditty, V. Schmitt, and F. Leal-Calderon. Particle-Stabilized Emulsions Comprised of Solid Droplets. *Langmuir* **21**, 4316-4323 (2005).
189 Adeline Perro, F. M., Veronique Schmitt, Serge Ravaine. Production of Large quantities of Janus nanoparticles using wax-in-water emulsions. *Colloids and Surfaces A: Physicochemical and Engineering Aspects* **332**, 57-62 (2009).
190 Liang Hong, S. J., and Steve Granick. Simple Method to Produce Janus Colloidal Particles in Large Quantity. *Langmuir* **22**, 9495-9499 (2006).
191 Shan Jiang, M. S., Qian Chen, Jeffrey Moore, Steve Granick. Solvent Free Synthesis of Janus Colloidal Particles. *Langmuir* **24**, 10073-10077 (2008).
192 Bragg, J. R. Oil recovery method using an emulsion. United States of America patent 5,855,243 (1999).
193 Dickinson, E. Food emulsions and foams: Stabilization by particles. *Current Opinion in Colloid & Interface Science*, 40-49 (2010).
194 Angel Tan, S. S., Andrew K. Davey, Thomas Rades, Clive A. Prestidge. Silica-lipid hybrid (SLH) microcapsules: A novel oral delivery system for poorly soluble drugs. *Journal of Controlled Release* **134**, 62-70 (2009).
195 Angelika Menner, R. V., Milo Shaffer, Alexander Bismarck. Particle-Stabilized Surfactant-Free Medium Internal Phase Emulsions as Templates for Porous Nanocomposite Materials: poly-Pickering-Foams. *Langmuir* **23**, 2398-2403 (2007).
196 Lumsdon, B. P. B. a. S. O. Influence of Particle Wettability on the Type and Stability of Surfactant-Free Emulsions. *Langmuir* **16**, 8622-8631 (2000).
197 B. P. Binks, P. D. I. F. Particles Adsorbed at the Oil-Water Interface: A Theoretical Comparison between Spheres of Uniform Wettability and “Janus” Particles. *Langmuir* **17**, 4708-4710 (2001).
198 SAMUEL LEVINE, B. D. B., SUSAN J. PARTRIDGE. Stabilization of Emulsions by Fine Particles I . Partitioning of Particles Between Continuous Phase and Oil/Water Interface. *Colloids and surfaces* **38**, 325-343 (1989).
199 Bernard P. Binks, P. D. I. F., Benjamin L. Holt, James Parker, Pascal Beaussoubre, Kenneth Wong. Drop sizes and particle coverage in emulsions stabilised solely by silica nanoparticles of irregular shape. *Physical Chemistry Chemical Physics* **12**, 2010 (2010).
200 Basavaraj Madivala, S. V., Jan Fransaerb, Jan Vermant. Exploiting particle shape in solid stabilized emulsions. *soft matter* **5**, 1717-1727 (2008).
201 Xuan-Cuong Luu, A. S. Ellipsoidal Janus Nanoparticles Assembled at Spherical Oil/Water Interfaces. *Journal of Physical Chemistry B* **118**, 13737-13743 (2014).
202 Howard Wang, E. H. Amphiphobic Carbon Nanotubes as Macroemulsion Surfactants. *Langmuir* **19**, 3091-3093 (2003).
203 Randy K. Wang, R. D. R., Kirk J. Ziegler. Interfacial Trapping of Single-Walled Carbon Nanotube Bundles. *JACS Communications* **129**, 15124-15125 (2007).

204 Randy K. Wang, H.-O. P., Wei-Chiang Chen, Carlos Silvera-Batista, Ryan D. Reeves, Jason E. Butler, Kirk J. Ziegler. Improving the Effectiveness of Interfacial Trapping in Removing Single-Walled Carbon Nanotube Bundles. *JACS* **130**, 14721-14728 (2008).
205 Lichun Dong, D. T. J. Adsorption of Acicular Particles at Liquid−Fluid Interfaces and the Influence of the Line Tension. *Langmuir* **21**, 3838-3849 (2005).
206 Wenbao Chen, X. L., Yangshuo Liu, Hyung-Il Kim. Novel synthesis of self-assembled CNT microcapsules by O/W Pickering emulsions. *Materials letters* **64**, 2589-2592 (2010).
207 Wenbao Chen, X. L., Yangshuo Liu, Youngkil Bang, Hyung-Il Kim. Preparation of O/W Pickering emulsion with oxygen plasma treated carbon nanotubes as surfactants. *Journal of Industrial and Engineering Chemistry* **17**, 455-460 (2011).
208 Tong Wu, H. W., Benxin Jing, Fang Liu, Peter C. Burns, Chongzheng Na. Multi-body coalescence in Pickering emulsions. *Nature Communications* **6** (2014).
209 Carlos Avendano, N. B., Olivier Fontaine, Martin In, Ahmad Mehdi, Antonio Stocco, André Vioux. Multiwalled Carbon Nanotube/Cellulose Composite: From Aqueous Dispersions to Pickering Emulsions. *Langmuir* **32**, 3907-3916 (2016).
210 Earl Christensen, J. F., Mariefel V. Olarte, Asanga B. Padmaperuma, Teresa Lemmon. Acid Number Determination of Pyrolysis Bio-oils using Potentiometric Titration. (National Renewable Energy Labratory, 2016).
211 M. S. P. SHAFFER, X. F., A. H. WINDLE. Dispersion and packing of carbon nanotubes. *Carbon* **36**, 1603-1612 (1998).
212 J. S. Weston, R. E. J., B. P. Grady, D. E. Resasco, J. H. Harwell. Silica Nanoparticle Wettability: Characterization and Effects on the Emulsion Properties. *Industrial Engineering Chemistry research* **54**, 4274-4284 (2015).
213 B. P. Binks, S. O. L. Catastrophic Phase Inversion of Water-in-Oil Emulsions Stabilized by Hydrophobic Silica. *Langmuir* **16**, 2539-2547 (2000).
214 B. P. Binks, S. O. L. Effects of oil type and aqueous phase composition on oil–water mixtures containing particles of intermediate hydrophobicity. *Phys. Chem. Chem. Phys.* **2**, 2959-2967 (2000).
215 Bernard P. Binks, C. P. W. Silica Particle-Stabilized Emulsions of Silicone Oil and Water: Aspects of Emulsification. *Langmuir* **20**, 1130-1137 (2004).
216 Bernard P. binks, J. H. C. Solid Wettability from Surface Energy Components: Relevance to Pickering Emulsions. *Langmuir* **18**, 1270-1273 (2002).
217 Jinbo He, Q. Z., Suresh Gupta, Todd Emrick, Thomas P. Russell, Pappannan Thiyagarajan. Drying Droplets: A Window into the Behavior of Nanorods at Interfaces. *Small* **3**, 1214-1217 (2007).
218 S. Stiller, H. G.-B., M. Lergenmueller, F. Pflücker, J. Schulz, K.P. Wittern, R. Daniels. Investigation of the stability in emulsions stabilized with different surface modified titanium dioxides. *Colloids and Surfaces A: Physicochemical and Engineering Aspects* **232**, 261-267 (2004).

219 Hengquan Yang, T. Z., Wenjuan Zhang. A Strategy for Separating and Recycling Solid Catalysts Based on the pH-Triggered Pickering-Emulsion Inversion. *Angewandte Chemie* **125**, 7603-7607 (2013).
220 Xuan-Cuong Luu, J. Y., Alberto Striolo. Nanoparticles Adsorbed at the Water/Oil Interface: Coverage and Composition Effects on Structure and Diffusion. *Langmuir* **29**, 7221-7228 (2013).

Appendix A: Stable Pickering Emulsions using Multi-Walled Carbon Nanotubes of Varying Wettability

The following appendix is based on a publication which can be found in Colloids and Surfaces A using the citation: “N. Briggs, A. Raman, L. Barrett, C. Brown, B. Li, D. Leavitt, C. Aichele, S. Crossley. Stable pickering emulsions using multi-walled carbon nanotubes of varying wettability. *Colloids and Surfaces A* **537**, 227-235 (2018).”

Introduction

Pickering emulsions have found uses in catalysis[36,184,185], Janus particle synthesis[186-191], oil recovery[192], food applications[193], drug delivery[194], and templates[195]. With the many uses for Pickering emulsions, the ability to control their properties can have a positive influence on a variety of fields. Emulsions droplet size and type of emulsion can be controlled by tuning the wettability of silica nanoparticles (by varying the number of SiOH groups on the surface), which in turn allows for control over the emulsion’s properties[196]. In addition, silica particles fused with single-walled carbon nanotubes (SWNTs) can also be tuned to change emulsion droplet size and type of emulsion when the SWNTs are oxidized[37].

Results from silica nanoparticle experiments have indicated that the minimum emulsion droplet size is achieved when the silica particles are amphiphilic[196]. The relationship between droplets size and particle wettability is determined by the free energy of a spherical particle adsorption at a planar interface. For a spherical particle at a planar interface, the free energy is[196-198]

$$E = \pi R^2 \gamma_{ow}(1 \pm \cos(\Theta))^2$$

Equation 1: Free energy of a spherical particle at a planar interface

where R is the particle's radius, γ_{OW} is its interfacial tension, θ is its contact angle, and E is the energy required for the particle to be adsorbed or desorbed at the oil-water interface. By plotting the equation while holding both the radius and interfacial tension constant and varying the contact angle, it can be seen that the energy required to remove a spherical particle from the interface is greatest when the contact angle is at 90°[196].

The energy required to place or displace a particle at an oil-water interface (Equation A-1) plays a large role in controlling the emulsion droplet size when using fractal silica particles of different wettability. However, Binks et al. showed that droplet coalescence rates are in fact related to the ability of fractal particle to reorient at an oil-water interface. This was attributed to the size of fractal silica particles requiring energy higher than the amount produced during droplet coalescence for the particle to desorb from the oil-water interface[199]. However, enough energy during droplet coalescence is produced to cause the fractal silica particle to re-orient at the oil-water interface and whether re-orientation of the fractal silica particles occurs is dependent on the energy required to adsorb or desorb a particle from the oil-water interface. Weakly held fractal silica particles at the oil-water interface during droplet coalescence reorient from a high surface area orientation to a low surface area orientation until the film of particles at the interface is compressed enough to stop droplet coalescence. Fractal silica particles strongly held at the oil-water

interface maintain a high surface area orientation producing a close packed particle film over the particle surface, which inhibits droplet coalescence and keeps the emulsion droplets small. Thus, how well the fractal particles are held at the oil water interface determines the emulsion droplet size with particles strongly held at the oil-water interface stabilizing smaller droplets than particles weakly held at the oil-water interface [199].

Despite extensive work done with Pickering emulsions stabilized with silica, few studies have focused on the use of carbon nanotubes as Pickering emulsion stabilizers. The aspect ratio of colloidal particles has been shown to influence colloidal particle coverage and emulsion stability and surface coverage, although fundamental studies have been limited to aspect ratios of less than nine[200,201]. While it is generally known that both aspect ratio and surface chemistry can influence emulsion properties and stability, a systematic study with carbon nanotubes, containing aspect ratios orders of magnitude greater than those in the previously mentioned studies, have not been attempted. The first study with carbon nanotubes in Pickering emulsions was with SWNTs showing as the concentration of single-walled carbon nanotubes (SWNTs) increases the emulsion droplet size decreases[202]. Other evidence supports the claim that it may not be individual nanotubes that stabilize Pickering emulsions, but rather aggregates and bundles of nanotubes. The tendency of nanotube bundles and agglomerates to reside at the interface has been used as a strategy to separate bundles from individual SWNTs in solution [203,204]. It should be noted that the diameter of individual SWNTs is less than one

nanometer. It has been shown that particles with sub nanometer diameters require reduced energy for desorption from an oil/water interface than larger particles[199,205]. Bundles of nanotubes inherently behave as particles with larger diameter and as a result are held more strongly to the interface.

Individual multi-walled carbon nanotubes (MWNTs) have larger diameters ranging from ~2–100 nm[39,42], depending on the number of walls, and therefore are harder to desorb from the oil-water interface, making them more suitable for stabilizing emulsions. For example, MWNTs, functionalized with oxygen containing groups, have been used to create water-in-oil (w/o) emulsions that could then be dried out to create carbon nanotube microcapsules[206]. Plasma treated MWNTs were shown to stabilize oil in water (o/w) emulsions, however, variations in plasma treatment conditions did not change the emulsion droplet size and untreated MWNTs formed little to no emulsion droplets[207]. The influence of this oxidation treatment of the MWNTs on long term emulsion stability was not studied. The behavior of carbon nanotubes at an interface is quite complex, as the attractive van der Waals forces between carbon nanotubes makes them agglomerate together and create a rigid network at the emulsion interface[206]. For untreated MWNT's it has been hypothesized to result in a dramatic enhancement in emulsion stability when compared to emulsions stabilized with silica particles experiencing charge repulsion[208]. Our recent work investigated the morphology of MWNTs at an oil water interface and illustrated this network through a combination of microscopy and interfacial area stabilized. We also showed that the addition of a surfactant creates a

repulsive force between carbon nanotubes that decreases emulsion stability[35]. While a great deal is known about the stability of emulsion droplets as a function of defect density for colloidal particles, no study provides insight with MWNTs into the influence of wettability on emulsion droplet size, type, and stability. It is also well known that colloidal particles that are very hydrophilic or hydrophobic do not yield stable Pickering emulsions due to rapid coalescence. One might hypothesize that multi-walled nanotubes could be an exception if the contact angle is varied to a wide degree while the nanotube-nanotube attractive forces are able to inhibit droplet coalescence. Because these characteristics are controlled both by the contact angle at the interface as well as nanotube-nanotube interactions, this information will be very valuable to advance the field and take advantage of these unique emulsion stabilizers. In addition, the influence of blended nanotubes with varying wettability on emulsion type has not been studied. To the best of our knowledge, there has been no effort made to control the degree of MWNT functionalization and to determine the resulting influence on emulsion stability. Due to the vast use of Pickering emulsions in industry, the ability to be able tune emulsion properties and stability would have an impact in many industrial fields.

The main objective of this work is to examine Pickering emulsions stabilized with MWNTs of different wettability characteristics and the resulting impact on emulsion stability. In addition, we report the effects of using different oils, oil to water ratios, concentrations of MWNTs, mixtures of MWNTs with different wettability characteristics were studied, along with the phase in which

the MWNTs were initially dispersed. The remarkable influence of the nanotube network in contrast to typical colloidal particles is demonstrated with emulsions stabilized with very high and low contact angles, as well as through catastrophic phase inversion by varying oil water ratios. Studying these effects allows for further comparisons to be drawn between MWNTs and other emulsion stabilizers. While literature studies have reported observations of Pickering emulsions stabilized with surface modified nanotubes[206,207], or co-stabilized with nanotubes and polymers[209] or surfactants[35]. A systematic study varying the degree of functional groups and oil-water ratios independently as described here has not been conducted. This study shows how MWNT wettability can be changed to tune emulsion properties and shows the effects these changes have on MWNT stability. We discover the behavior of nanotubes to stabilize Pickering emulsions across a wide range of droplet sizes while maintaining emulsion stability. We further demonstrate nanotube stabilized emulsions can stabilize Pickering emulsions after catastrophic phase inversion.

Experimental

MWNTs were obtained from SouthWest Nanotechnologies, Inc. that were designated by the company as type SMW100. The MWNTs were less than one micron long with diameters between 6–9 nm, and contained from three to six walls. Nitric acid (70%), dodecane (99%), heptane (99%), and toluene (99%) were purchased from Sigma Aldrich. 18 MΩ water was obtained from a Cole Parmer filtration system set up in our lab. Water used from this system had a pH= 6.8.

Oxidation of the MWNTs was completed by adding one gram of MWNTs to a round bottom flask and using either 6 M or 12 M HNO3 to control the number of functional groups. The solution was then refluxed at 110 °C for either 1.5 h or 24 h to control the number of functional groups. After oxidation, the MWNT solution was filtered using a 0.22 μm PTFE filter. After this, the filtered material was rinsed with 18 MΩ water until the pH was neutral.

MWNT Pickering emulsions were made by horn sonication using a Fisher Scientific Model 505 Sonic Dismembrator with a 0.5-inch horn tip. Between 0.03% and 0.26% by weight with respect to water of MWNTs were then added to a 100 ml beaker. A concentration of 0.07 wt% of MWNTs was used for all emulsions, unless otherwise stated. Except for emulsions where the oil to water ratio was changed, an equal volume of Dodecane was then added to the same amount water used. The solution was then sonicated for five minutes at 75% amplitude to disperse the MWNTs since they are typically highly agglomerated and bundled naturally in their solid state. After this, the opposite phase, either oil or water, was then added and emulsification was performed by horn sonicating the solution for five minutes at 100% amplitude. Twenty-four hours after emulsification, emulsion droplet size, volume fraction of oil, emulsion, and water were measured and then the emulsions were left undisturbed for one month. After one month, the emulsion droplet size and volume fraction of oil, emulsion, and water were measured again and emulsion stability was determined by comparing emulsion droplet size and interfacial area one month and 24 h after emulsification. Interfacial area was calculated

using the number average droplet diameter and volume fractions of oil, emulsion, and water. A sample calculation illustrating interfacial area calculations can be found in the supplementary information.

Optical microscopy was used to obtain the average emulsion droplet size for each emulsion by depositing a drop of the emulsion phase on a microscope slide and viewing it under an optical microscope, which allowed for capturing the images shown in this study. Image J software was used to measure the diameter of one hundred emulsion droplets from the captured images, which was then used to make a histogram of droplet size and determine average droplet size. Histograms of the droplet sizes can be found in the supplementary information.

Two methods were used to test if the resulting emulsion was of type o/w or w/o. If an aliquot of the emulsion dispersed in a beaker of pure water, then the test indicated that it was an o/w type of emulsion. If the aliquot did not disperse, then it was determined to be a w/o type of emulsion. The second method utilized the opposite phase in the same manner. If an aliquot of the emulsion dispersed in a beaker of pure dodecane, then the test indicated it was a w/o type of emulsion, and similarly, if it did not disperse, it was determined to be an o/w type of emulsion.

All temperature programmed desorption (TPD) experiments were performed in a Thermcraft Furnace (Model SST-0.75-0-12-1C-D2155-A). Each MWNT sample was prepared by drying it at 120 °C in a vacuum oven to remove any moisture, adjusting its weight to 50 mg, and then placing it in a quartz tube

(3 mm inner diameter, 5 mm outer diameter, 50 cm length). An Omega thermocouple was placed in the quartz tube at the surface of the CNT material to ensure that the heating rate was maintained at 10 °C/min. Quartz wool (~300 ml) was used at the inlet and outlet of the furnace around the sample tube in order to minimize heat loss. These samples were heated programmatically from room temperature to 900 °C at a heating rate of 10 °C/min in the Thermcraft furnace with a helium flow of 35 ml/min. After the samples reached 900 °C, after approximately 90 min, the temperature was held isothermal for an additional 30 min with a helium flow of 35 ml/min. The outlet gas from the furnace was then mixed with a hydrogen stream (45 ml/min) and fed into a nickel (aluminum supported) catalyst held at 400 °C, which converted all of the carbon containing gases to methane. This gas stream was then sent to a flame ionizing detector (FID) (SRI 110 Detector Chassis) where it was mixed with oxygen (80 ml/min) and hydrogen (10 ml/min) to produce combustion for the detector.

Total integrated TPD signals were used to determine the atomic percentage of the Oxygen groups on the MWNT sample material. This was achieved by using Simpson's rule for integration of the FID signal over time. The total moles of carbon desorbed were calculated by multiplying the integrated area by a constant, which was determined by injecting CO2 (in 64 micoliter pulses) through the TPD system under the same conditions and flow rates used for all of the other gases described above. Treating this CO2 as an ideal gas provided a molar value associated with the total integrated TPD signal, 1.3 ×10−13 mol C/area. It was assumed that the carbon desorbed from

the CNT material during the TPD experiments was equivalent to the oxygen functional groups created by the acid treatments, due to the lower thermal stability of these groups which convert to CO or CO2. Based on this assumption, the atomic percentage of the thermally unstable functional groups containing carbon and oxygen was calculated to be the ratio of total molar carbon desorbed (found by the process above) and the total molar carbon in the initial sample.

The TPD experimental data suggests that the four samples tested above had 0.8%, 2.3%, 3.1% and 4.4% by weight of thermally unstable carbon on their surfaces. These four samples were then designated as follows: sample 0.8MWNT, which was the as-received sample from SouthWest Nanotechnologies, Inc; sample 2.3MWNT, which had been oxidized for 1.5 h with 6 M HNO3 at 110 °C; sample 3.1MWNT, which had been oxidized for 24 h with 6 M HNO3 at 110 °C; and sample 4.4MWNT, which had been oxidized for 24 h with 12 M HNO3 at 110 °C.

Differentiation of oxygen species was accomplished using the modified acid number determination method as set forth by the National Renewable Energy Laboratory[210]. A solution of 200 mg CNT sample in 50 ml IPA was sonicated to mimic breakage during emulsification and titrated with 0.1 M tetrabutyl ammonium hydroxide in IPA to reach two equivalence points, the first from carboxylic acids and a second from phenolic groups. To convert the number of acid groups on the surface into a wt%, an assumed molecular weight of 45 was used for carboxylic acids and 29 was used for alcohols. All oxygen

groups identified by TPD but not measured by the titration were considered to be esters, ethers, and ketones on the surface.

Heat of immersion measurements were performed with a Setaram C80 microcalorimeter with a custom built pair of powder cells. Before each experiment the MWNTs were dried in a vacuum oven at 120 °C for twelve hours. A known quantity of sample was loaded into each cell and sealed with nitrile rubber membrane. Both powder cells were then placed in larger calorimetry cells with approximately eight millimeters of water. Then each calorimeter cell was placed in the microcalorimeter and allowed to equilibrate to 40 °C. After stabilization the sample and reference cell were punctured and the energy released by the samples measured. A series of blank punctures of sealed and empty powder cells were used to estimate the heat released when puncturing the nitrile membranes and this data used to correct when MWNT samples were used. An average was calculated from the two samples and used to calculate the particle contact angle. A sample calculation is provided in the supplementary information.

Results and Discussion

MWNTs are inherently hydrophobic and tend to agglomerate due to van der Waals forces. A typical method to increase the hydrophilicity and decrease agglomeration is to oxidize the MWNTs with nitric acid or a mix of nitric and sulfuric acid to create hydrophilic functional groups[5,51,211]. By varying the MWNTs treatment with nitric acid, the number of hydrophilic functional groups can be controlled, which was determined using TPD methods, Fig. 51.

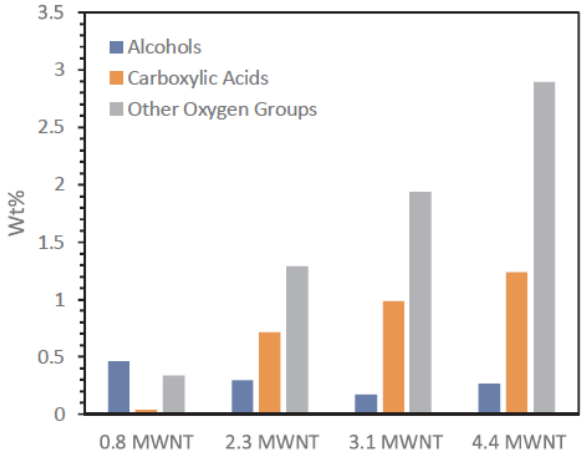

Figure 52: Weight percent of various oxygen containing functional groups based on a combination TPD results and titration of MWNT samples.

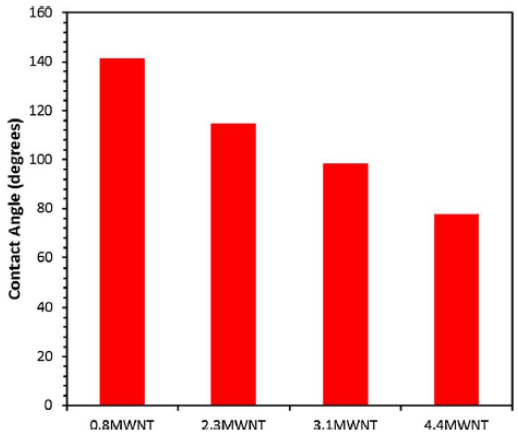

Figure 51: Air-particle-water contact angle measurements for the four MWNT samples.

Functional groups were then distinguished through the use of titration to decouple carboxylic acid groups and alcohols from all other oxygen containing groups. TPD plots showing the carbon desorbed as a function of temperature for each sample are included in the supplementary information, Fig. S1.

Further proof of MWNTs having different wettability was performed by measuring the air-particle-water contact angle using the heat of immersion method[212]. The heat of immersion, enthalpy of immersion, is a result of the change in the Gibbs free energy which results from replacing a solid-gas interface with a solid-liquid interface. This can be related to the solid-liquid contact angle using the Young-Laplace equation. A sample calculation is provided in the supplementary information. As can be seen in Fig. 52 each of the MWNT samples has different air-particle-water contact angle. This indicates the oxidation treatment is sufficient at producing MWNTs with different wettability. Another method was used to further confirm each MWNT sample

Table 2: Emulsion type for each O:W ratio of the MWNT samples.

O:W Ratio	Sample			
	0.8MWNT	2.3MWNT	3.1MWNT	4.4MWNT
1:4	w/o	o/w	o/w	o/w
2:3	w/o	o/w	o/w	o/w
1:1	w/o	w/o	o/w	o/w
3:2	w/o	w/o	o/w	o/w
4:1	w/o	w/o	w/o	o/w

had a different wettability. This method was used by Binks et al. showing that silica nanoparticles of different wettability had different emulsion inversion points when changing the oil to water ratios[196,213]. Hydrophobic particles favor w/o emulsions at a one to one oil to water ratio, while hydrophilic particles favor o/w emulsions[5,196]. A high oil to water ratio is required for emulsion inversion of particles with a high amount of hydrophobic groups, while a low oil to water ratio is required for particles with a low amount of hydrophobic groups. It also follows that a roughly equal oil to water ratio is required for emulsion inversion of particles with an intermediate amount of hydrophobic groups. Since particles of different hydrophobicity have different emulsion inversion points when changing oil to water ratios, a quick characterization of the particles' hydrophobicity can be accomplished using this phenomenon. Using this characterization method, it was found that different oil to water ratios were required for emulsion inversion for each MWNT sample, as shown in Table 2. This indicates the hydrophilicity of each MWNT sample is unique, which correlates with the TPD experimental results and contact angle measurements. Initially no inversion in emulsion was

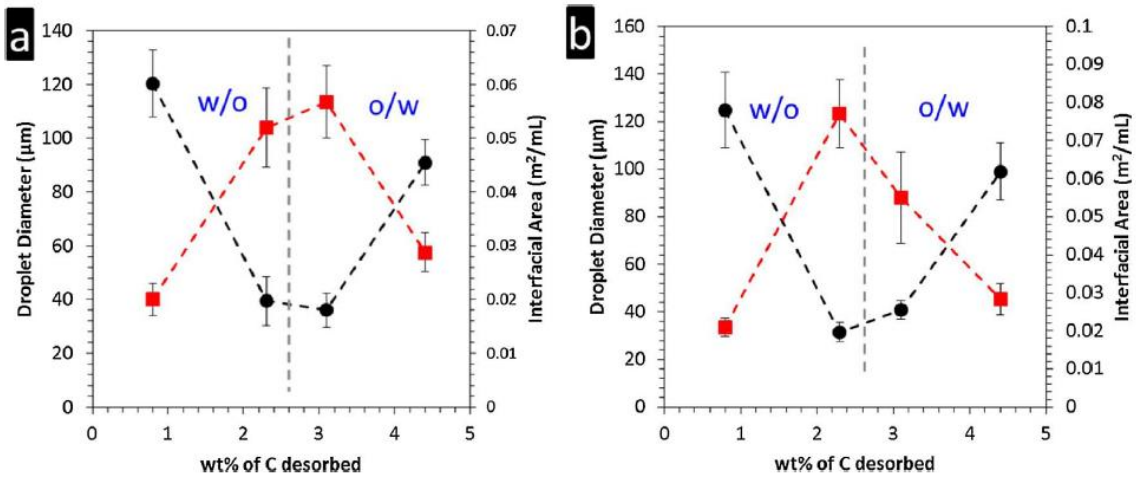

Figure 53: for dodecane and water systems, (a) shows change in droplet diameter and interfacial area as a function of MWNT wettability when dispersing MWNTs in water while (b) shows change in droplet size and interfacial area as a function of MWNT wettability when dispersing MWNTs in dodecane. 0.07 wt% of MWNTs were used in both cases. Circles represent droplet diameter and squares represent interfacial area. All emulsions are made with one to one oil to water ratio. Lines are included to help guide the eye.

obtained, due to the MWNTs' inherent hydrophobicity. As the number of hydrophilic functional groups increased on the MWNTs, the point at which emulsion inversion occurred required higher oil to water ratios. For sample 4.4MWNT, with the greatest fraction of functional groups, no emulsion inversion was observed, indicating that the nanotubes are hydrophilic. The most hydrophobic and hydrophilic MWNTs may invert at higher or lower oil to water ratios, respectively, but this was not tested as the results show each MWNT samples wettability is different.

Emulsion droplet size and interfacial area change based on the MWNTs wettability, as shown in Fig. 53. Fig. 53 illustrates that the emulsion droplet diameter is largest with hydrophobic and hydrophilic MWNTs and smallest with amphiphilic MWNTs, and that the emulsion type inverts in the range of amphiphilic MWNTs. Prior studies with colloidal silica particles have reported

the type of emulsion to change depending on the phase (oil or water) that silica particles of intermediate wettability were initially dispersed in[214]. For MWNTs in the amphiphilic range, however, it was found that the emulsion type did not change if the MWNTs were dispersed in water, Fig. 53(a), or oil, Fig. 53(b), which may have been due to not having MWNTs of the required wettability. Regardless of whether the MWNTs were dispersed in the oil or water, the trend in droplet size with MWNT wettability remains the same. Amphiphilic MWNTs create the largest interfacial area from having the smallest emulsion droplet size. The most hydrophobic and hydrophilic MWNTs stabilize the smallest interfacial area due to the large emulsion droplet sizes, Fig. 53 (a).

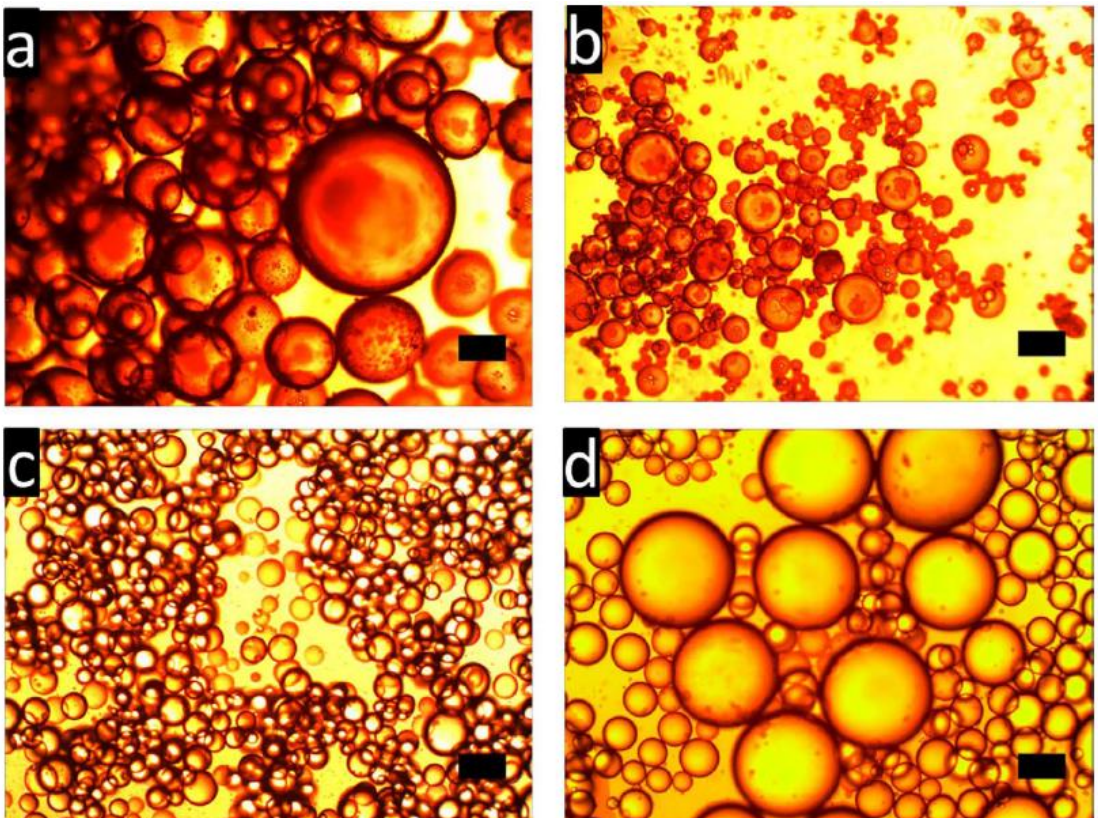

Figure 54: Optical microscope images for dodecane and water systems (a) sample 0.8MWNT, (b) sample 2.3 MWNT, (c) sample 3.1MWNT, and (d) samples 4.4MWNT. 0.07 wt% of MWNTs were used in all cases. The scale bar shown in the images in 100 μm.

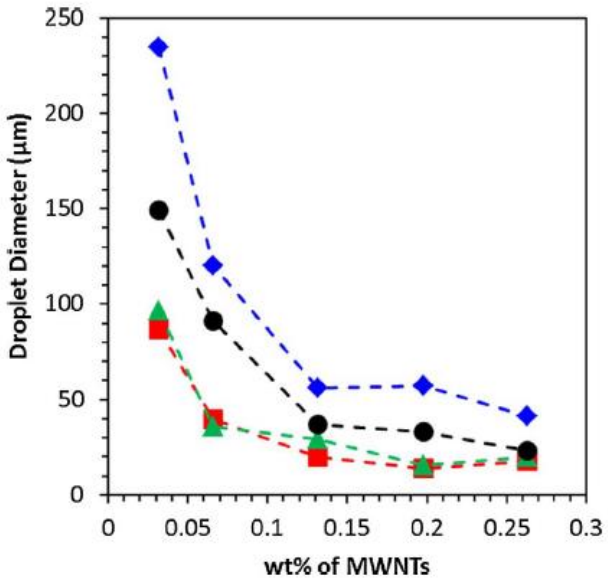

Figure 55: Effect of concentration of MWNTs on emulsion droplet size for each sample. Diamonds are for sample 0.8MWCNTs, squares are for sample 2.3 MWNT, triangles are for sample 3.1MWNT, and circles are for sample 4.4MWNT. All emulsions are made with one to one oil to water(volume: volume) ratio. Lines are included to help guide the eye.

The results of studying the variation in MWNT concentration, Figs. 54 and 55, showed the same trend as shown in Fig. 53 for MWNTs of different wettability. Previous work by others showed that the emulsion droplet size decreases as the concentration of particles in an emulsion system increases until a point is reached where the emulsion droplet size plateaus as the particle concentration increases[215]. The initial decrease in emulsion droplet size is dependent on the number of particles. With more particles in the system, more particles reside at the oil-water interface and thus prevent droplet coalescence by way of steric hindrance. It was found that at a particular point, there were sufficient particles to cover the emulsion droplets and droplet sizes no longer changed. For all of the MWNT samples, it was found that the emulsion droplet size decreased until reaching a plateau at which point the emulsion droplet size no longer changed significantly.

The studies described below with varying functional groups all used 0.07 wt% MWNT concentration. As can be seen in Fig. 55 this is not in the region of

excess nanotube concentration. To further elucidate this, the same data is plotted on a log–log plot in the supplementary information, revealing that all of the MWNT samples studied at 0.07 wt% are in a linear region on the log–log plot and it is not until 0.2 wt% of MWNTs that this begins to deviate from linearity.

To further study the extent to which the change in MWNT wettability could be used to tune emulsion droplet size, two additional oils with differing oil-water contact angles on silica surfaces, toluene and heptane, were used and tested in addition to dodecane. n-Heptane has an oil–water interfacial tension of 50.7 mN/m and contact angle of 105°and dodecane has an oil-water interfacial tension of 52.5 mN/m and contact angle of 122° [212]. Toluene has an oil-water interfacial tension of 36.0 mN/m and contact angle of 125°[216]. Dodecane and toluene vary the most in interfacial tension, however, both interfacial tension and oil-water contact angle affect the energy of adsorption/desorption for a particle at the oil-water interface. Viscosity may also play an important role in droplet size, with the viscosity of toluene, heptane, and dodecane being 0.550 mPas, 0.386 mPas, and 1.34 mPas, respectively. In spite of these differences in oil properties, all of the oils tested exhibit to the same general inverse volcano trend in emulsion droplet size and volcano shaped curve with interfacial area observed as a function of increasing particle hydrophilicity. This observation is similar to those reported for oil/water systems stabilized with traditional colloidal particles[196-198]. As expected, the emulsion droplet size and interfacial area varies depending on if heptane, Fig. 56(a), toluene, Fig. 56(b),

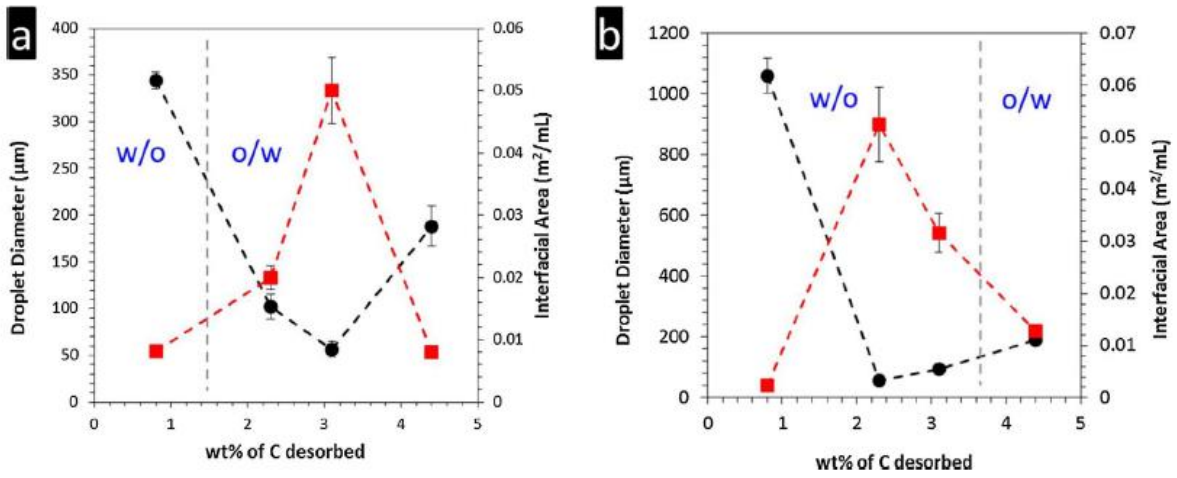

Figure 56: Change in emulsion droplet size and interfacial area for (a) heptane and (b) toluene. Circles are for droplet diameter and squares are for interfacial area. 0.07 wt% of MWNTs were used. All emulsions are made with one to one oil to water ratio. Lines are included to help guide the eye.

or dodecane, Fig. 53, is used. The point at which the emulsion type changes with respect to MWNT wettability also depends on the type of oil. With heptane, the emulsion type changed from w/o to o/w between sample 0.8MWNT and sample 2.3MWNT and with toluene this inversion occurred between sample 3.1MWNT and sample 4.4MWNT. Similarly, the point at which emulsion type changes with respect to silica wettability has been found to vary when using toluene[196] and limonene[199].

The reason for the variation in emulsion droplet size when changing MWNTs wettability may follow the same line of reason as for silica nanoparticles of different wettability. As has been shown with silica nanoparticles, the energy with which a cylinder adsorbs or desorbs from the oil-water interface is greatest for cylinders that are amphiphilic[203,204,217]. Cylindrical particles have been found to favorably orient parallel to the oil-water interface[203] and our recent work has shown that the majority of multi-walled carbon nanotubes (MWNTs) orient parallel to the interface of the emulsion droplet[207]. In

a parallel orientation, MWNTs take up the most surface area at the oil-water interface. We hypothesize that extremely hydrophobic and hydrophilic MWNTs at the oil-water interface may re-orient from a high surface area orientation to a low surface area orientation during droplet coalescence due to being weakly held at the oil-water interface. With the hydrophobic and hydrophilic MWNTs re-orienting to a low surface area orientation the emulsion droplet size increases. Droplet coalescence may not cause amphiphilic MWNTs to re-orient to the same degree at the oil-water interface due to their strong affinity for the oil-water interface. Therefore, amphiphilic MWNTs could maintain a high surface area orientation and prevent droplet coalescence, keeping emulsion droplet sizes smaller than when using hydrophobic or hydrophilic MWNTs.

Emulsion stability is governed by four primary mechanisms: sedimentation, creaming, flocculation, and coalescence. Steric hindrance and electrostatic repulsion are the primary mechanisms that aid in stabilization of solid-stabilized emulsions. Agglomeration of carbon nanotubes, caused by strong van der Waals forces, has been shown to enhance emulsion stability when compared to silica nanoparticles which suffer from charge repulsion[206]. Van der Waals forces between carbon nanotubes form a rigid network at the interface of an emulsion droplet that keeps emulsion droplets from coalescing. Charge repulsion between silica particles creates a weak network at the interface of an emulsion droplet that allows for the rate of coalescence to increase. Emulsions stabilized with silica particles with different wettability properties have been shown to have different emulsion stability

characteristics[196]. In their study the wettability of the silica nanoparticles was determined by changing the oil to water ratio and determining at which point the emulsion inverted. A low oil fraction is required for emulsion inversion with hydrophilic particles and a high oil fraction is required for emulsion inversion to occur with hydrophobic particles. The most unstable emulsion was made with hydrophobic and hydrophilic fractal silica particles. The wettability of these particles, which form unstable emulsions, can be characterized roughly by their emulsion inversion point. Hydrophobic fractal silica particles require a water fraction above 0.9 to invert, while hydrophilic fractal silica particles required a water fraction of 0.35 to invert in a water-toluene system.

Emulsion stability tests done for this study with MWNTs showed small changes in the interfacial area 24 h and one month after emulsification, Fig. 57,

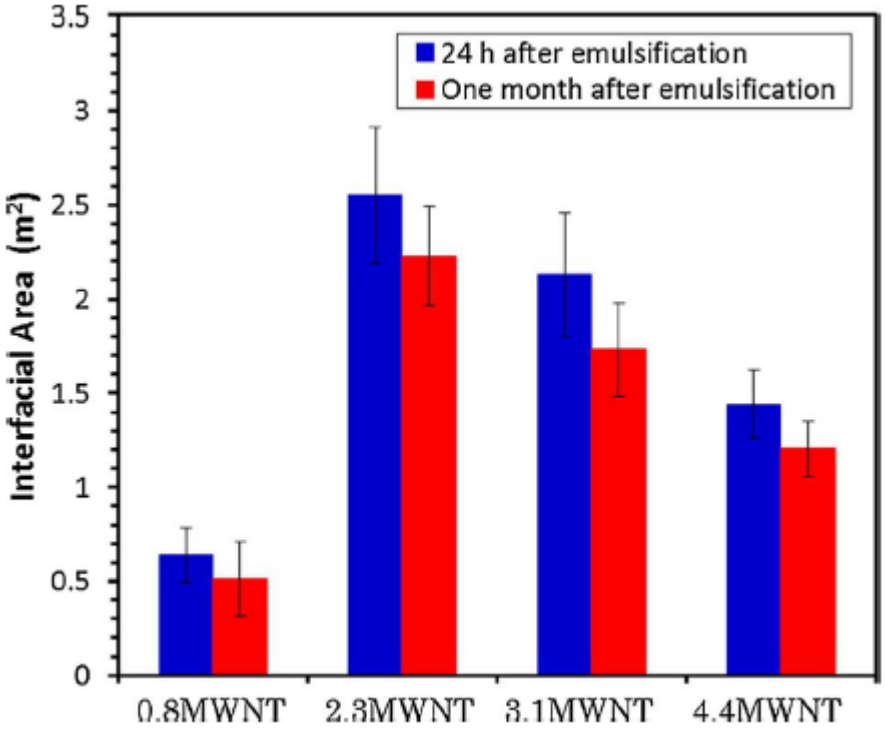

Figure 57: Change in interfacial area 24 h and one month after emulsification. Emulsions were made with dodecane and water. All emulsions are made with one to one oil to water ratio. 0.07 wt% of MWNTs were used.

indicating that the MWNT network was maintained even though the MWNT wettability characteristics had been changed. Treatment of the MWNTs with nitric acid added oxygen-containing functional groups and can help disperse the MWNTs by creating repulsion. In this case, however, the functionalization was enough to change the MWNT wettability characteristics but not enough to weaken the MWNT network that inhibited droplet coalescence. The fact that the most oxophilic nanotubes, 4.4MWNT, exhibit the same remarkable stability as the most hydrophobic nanotubes tested, 0.8MWNT, supports this statement. The MWNTs tested here have roughly the same wettability as the silica nanoparticles based on inversion points in the literature[196]. Silica particles with similar wettability exhibit reduced emulsion stability than the nanotubes studied here. The most hydrophobic nanotubes investigated, 0.8 MWNT, require a water fraction greater than 0.8 for emulsion inversion to occur and the most hydrophilic nanotubes, 4.4MWNT, require a water fraction lower than 0.2 for emulsion inversion to occur. This range is comparable to fractal silica particles studied by Binks et al. and allows direct comparison between the MWNTs used in this study and fractal silica[196]. This high emulsion stability can be maintained even for droplets of 1000 μm in diameter when using toluene and 0.8MWNTs, with no significant change in emulsion droplet size occurring after one month. For comparison, silica particles with similar wettability exhibited complete coalescence in ten minutes. From these results it can be concluded that for applications requiring high emulsion stability MWNTs offer greater flexibility

than other colloidal stabilizers, as the properties of the emulsions can be tuned while the stability is maintained.

The unique geometry of carbon nanotubes and the attractive forces between carbon nanotubes may play a role in providing this enhanced emulsion stability. Calculations have shown that cylindrical particles at the oil-water interface require a greater energy to desorb than their spherical counterparts[203]. As Binks et al. have shown, this energy can be attributed to the likelihood of the particles to re-orient to accommodate droplet coalescence[199]. The attractive forces between carbon nanotubes create a network at the oil-water interface capable of significantly reducing multibody coalescence compared to particles exhibiting repulsive particle-particle interactions. This carbon nanotube network at the oil-water interface is strong enough that emulsion droplets retain their shape even after the oil and water have been evaporated, which has been used as a strategy to create hollow capsules[42]. The fact that the interfacial areas stabilized per nanotube decrease as more oxygen containing functional groups are introduced (Table S1), while the net emulsion stability is not diminished (Fig. 57) further supports the presence of an attractive network across all of the nanotube samples compared here. The high energy required to remove carbon nanotubes from the interface due to their geometry and the reduction in multibody coalescence rates due to the attractive forces between carbon nanotubes likely contributes to the superior emulsion stability observed here.

Manipulating the oil to water ratio of an emulsion allows for tuning of the emulsion characteristics without having to change particle properties, or the oil

or aqueous phase. When changing the oil to water ratio for hydrophobic MWNTs, a decrease in emulsion droplet size was observed as the oil fraction increased with no change in emulsion type, sample 0.8MWNT, Fig. 58(a). Stiller et al. showed a similar trend for hydrophilic titanium dioxide, except the emulsion droplet size increased with increasing oil fraction due to the hydrophilic nature of the titanium dioxide[218]. Holding the amount of MWNTs constant and decreasing the volume of water the number of emulsion droplets

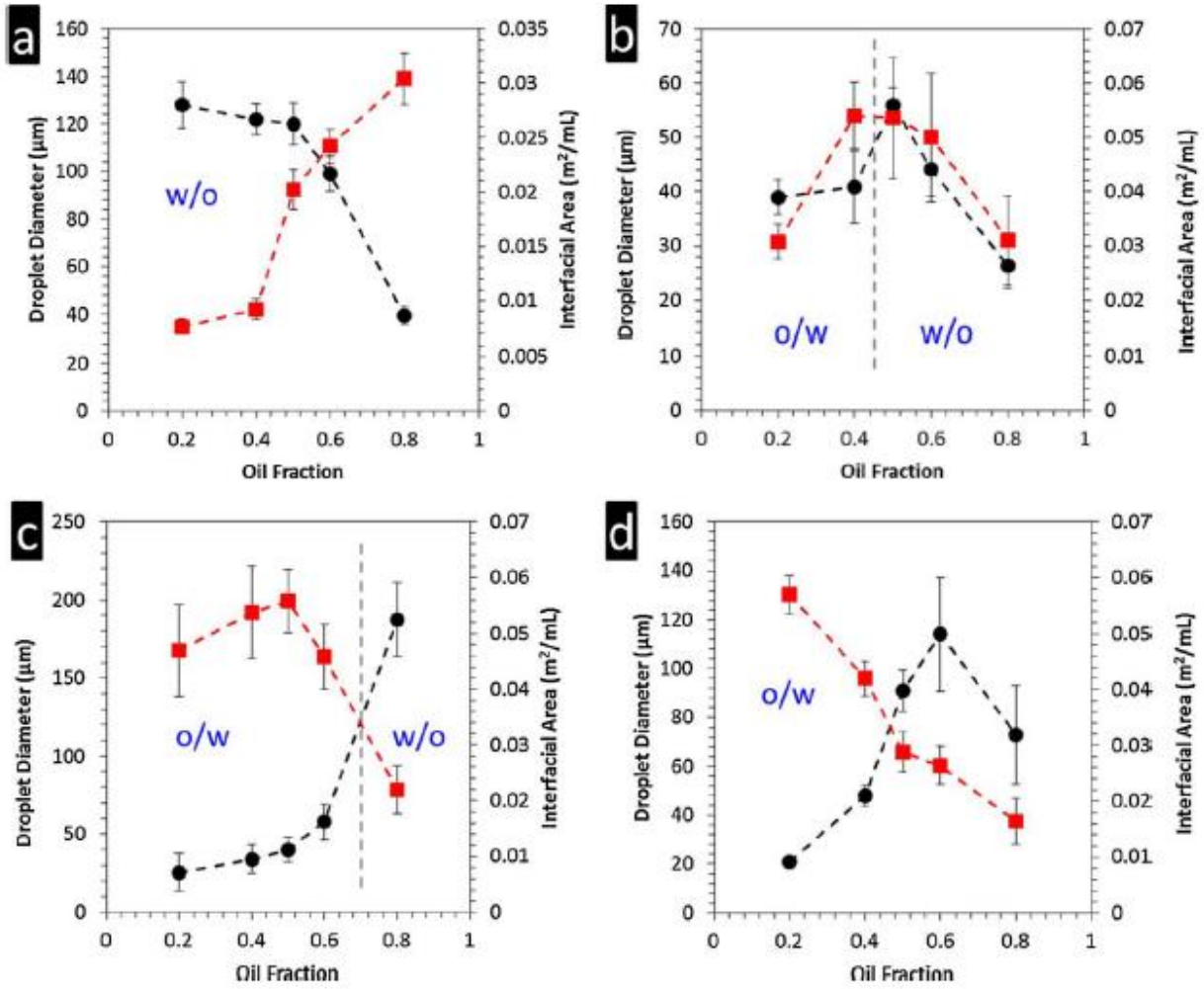

Figure 58: Effect of changing the oil (dodecane) to water ratio on droplet diameter and interfacial area. Sample (a) 0.8MWNT, (b) 2.3MWNT, (c) 3.1MWNT, & (d) 4.4MWNT. Circles are for droplet diameter, and squares are for interfacial area. 0.07 wt% of MWNTs was used. Lines are to help guide the eye.

increased. With this increase in the number of emulsion droplets and the decrease in droplet size, the interfacial area stabilized increases.

For MWNTs with intermediate wettability characteristics, the emulsion droplet size and interfacial area decreased at high and low oil fractions, sample 2.3MWNT, Fig. 58(b). Because emulsion inversion occurs close to an oil fraction of 0.5, the MWNTs are approximately equally wet by both oil and water[196]. This may be why the greatest interfacial area is obtained at an oil fraction close to 0.5, and that the change in emulsion droplet size at the inversion point is not catastrophic.

Test results from sample 3.1MWNT shows that since the emulsion droplet size is small, catastrophic phase inversion does not occur until an oil fraction of 0.8 is reached Fig. 58(c). This type of catastrophic phase inversion has also been observed with hydrophobic and hydrophilic silica particles[5]. This study found that emulsion droplet size increases significantly after reaching the oil fraction that causes emulsion inversion from o/w to w/o and that the significant change in emulsion droplet size corresponds with a decrease in interfacial area.

The observation of catastrophic inversion provided an opportunity to further study the ability of MWNTs to stabilize emulsions since this causes significant changes in emulsion type and droplet size. Fig. 59 illustrates that emulsion stability did not change regardless of the oil to water ratio as shown for sample 3.1MWNT, Fig. 59. It was also found that even after emulsion inversion and a significant change in emulsion droplet size, the emulsion was

still stable. With MWNTs, the oil to water ratio can be used to change the emulsion type and droplet size without affecting emulsion stability, which may prove useful for separating and recycling solid catalyst particles based on Pickering emulsion inversion[219].

This study found that the most hydrophilic MWNTs, sample 4.4MWNT, exhibits no change in emulsion type, Fig. 58(d), as the fraction of oil is varied over the ranges studied here. As the oil fraction is decreased, emulsion droplet size decreases and the interfacial area increases. A similar trend is seen in emulsion droplet size when using hydrophilic titanium dioxide particles[216]. With less oil in a system and the amount of MWNTs held constant, the number of emulsion droplets increased. The number of emulsion droplets is calculated as part of the calculation to calculate the interfacial area, as can be seen in the supplementary information. The increase in the number of emulsion droplets and the decrease in droplet size increased the interfacial area.

Mixtures of MWNTs of different wettability were used to further study the behavior of MWNTs at the oil-water interface. Emulsion droplet size and emulsion type changed depending on the ratios of hydrophobic MWNTs, sample 0.8MWNT, and amphiphilic MWNTs, sample 3.1MWNT, mixed together. Both types of MWNTs were initially dispersed in water, and as stated previously, no significant change was initially observed when dispersing the MWNTs in oil or water. Increasing the ratio of sample 0.8MWNT to sample 3.1MWNT produced increases in emulsion droplet size that occurs slowly at first as the ratio increases, but rapidly accelerates after the mixture of the two

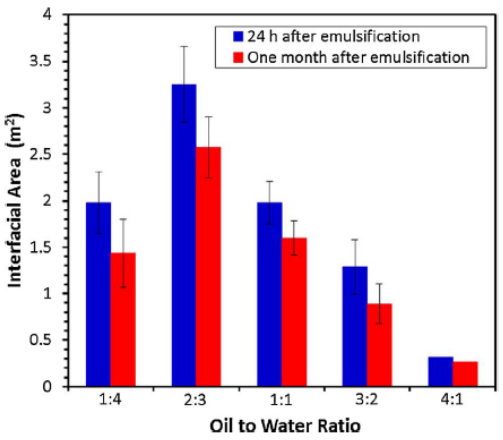

Figure 59: Change in interfacial areas for different oil to water ratios over a one month period for samples 3.1MWNT. 0.07 wt% of MWNTs was used.

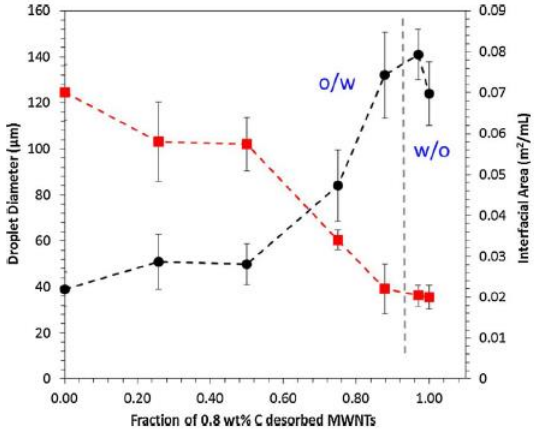

Figure 60: Effect of changing the ratio of MWNTs with different wettability on emulsion droplet size and interfacial area. 0.7 wt% of MWNTs used, varied fraction of 0.8MWNT to 3.1MWNT. Circles are for droplet diameter and squares are for interfacial area. All emulsions are one to one oil to water ratio.

sample types of MWNTs become equal, Fig. 60. The emulsion type does not change until the ratio of sample 0.8MWNT to sample 3.1MWNT reaches 0.97.

This trend agrees with what has been seen by others using silica particles of different wettability when mixed together to make emulsions, which has been attributed to the average wettability of the particles at the oil-water interface[213]. For mixtures of MWNTs with different wettability, the emulsion droplet size is non-linear, Fig. 60. Recent dissipative particle dynamics simulations have shown that particles of opposite wettability are closer together than particles of the same wettability at the oil-water interface[220]. If the two MWNTs of different wettability are influencing each other's ability to re-orient at the interface, this may cause the non-linear trend in emulsion droplet size with varying ratio of hydrophobic to hydrophilic MWNTs that is observed.

Conclusions

Pickering emulsions stabilized with MWNTs are highly stable. The MWNTs used to stabilize emulsions can also be tuned to have different wettability characteristics to change emulsion properties. Through controlled functionalization of MWNTs, the properties of Pickering emulsions can be controlled along with changes in emulsion droplet size and emulsion inversion points consistent with different oils. Changing the oil to water ratio allows for emulsion droplet size to be changed, and for amphiphilic MWNTs, the emulsion type to be changed. Mixing MWNTs of different wettability characteristics in different ratios can be used to control emulsion droplet size and type, which creates the prospect of achieving the same results as tuning MWNTs to specific wettability characteristics. Most importantly, MWNT wettability characteristics can be tuned to change emulsion properties while inhibiting emulsion droplet coalescence and opens this possibility for a wider range of possibilities with Pickering emulsions due to their high stability over other solid particle emulsion stabilizers.

Acknowledgements

The authors thankfully acknowledge Ricardo Prada Silvy of Southwest Nanotechnologies for donating the multi-walled carbon nanotubes used in this study. This work was supported by the U.S. Department of Energy, DOE/EPSCOR (Grant DESC0004600). Nanotube surface characterization was supported by NSF under grand 1436532.

Supplementary data

Supplementary data associated with this article can be found, in the online version, at http://dx.doi.org/10.1016/j.colsurfa.2017.10.010.

Appendix B: Observations of Carbon Nanotube Growth

Growth on Vermiculite

Effects of Catalyst Composition on CNT Growth on Vermiculite

Growth on two different substrates allowed for the possibility of different effects on the growth rate. The hydroxyethyl cellulose added to the catalyst solution to increase its viscosity for the spin coating may cause a mass transfer issue preventing the catalyst particles from reaching in between the layers of vermiculite. The cellulose was burned off prior to growth through calcination, so it shouldn't affect the actual growth of the nanotubes, but it may affect the coverage of catalyst particle. Growth was performed with and without the cellulose and it was confirmed the height of the forest was the same, but the thickness of the forest was reduced without the cellulose. This is due to sintering of the particles during the drying of the catalysts. For this reason the incipient wetness impregnation on the vermiculite was repeated to ensure maximum coverage after the drying effects. Figure 61, 62, and 63 show a top down SEM view of a forest on the vermiculite after 1, 2, and 3 impregnations respectively. After 3 impregnations the forest appeared to have reached full coverage of the support, while the coverage was spotty after 1 and 2 coatings.

Vermiculite Sheet Adherence and Separations

The purpose of using a lamellar support was to enable growth in a fluidized bed while protecting the inner particles from attrition. To that end several tests were performed to study how the vermiculite layers would hold

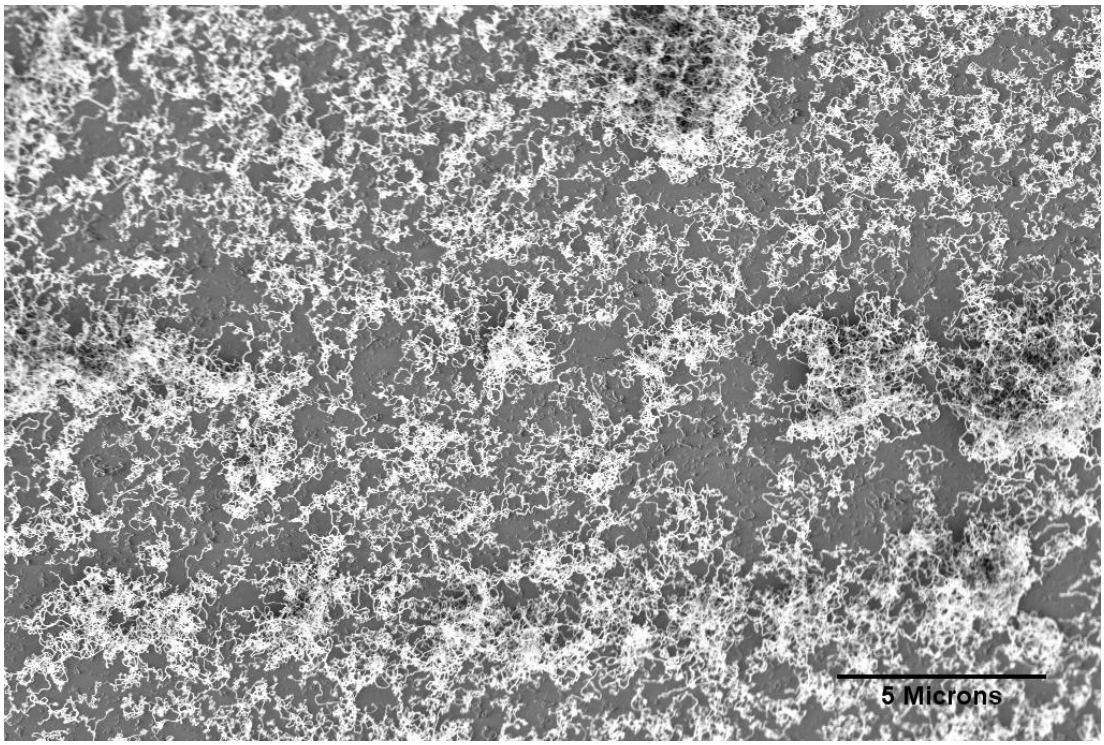

Figure 60:Top down SEM image of nanotubes grown on vermiculite at 675°C with pure ethylene after a single incipient wetness impregnation

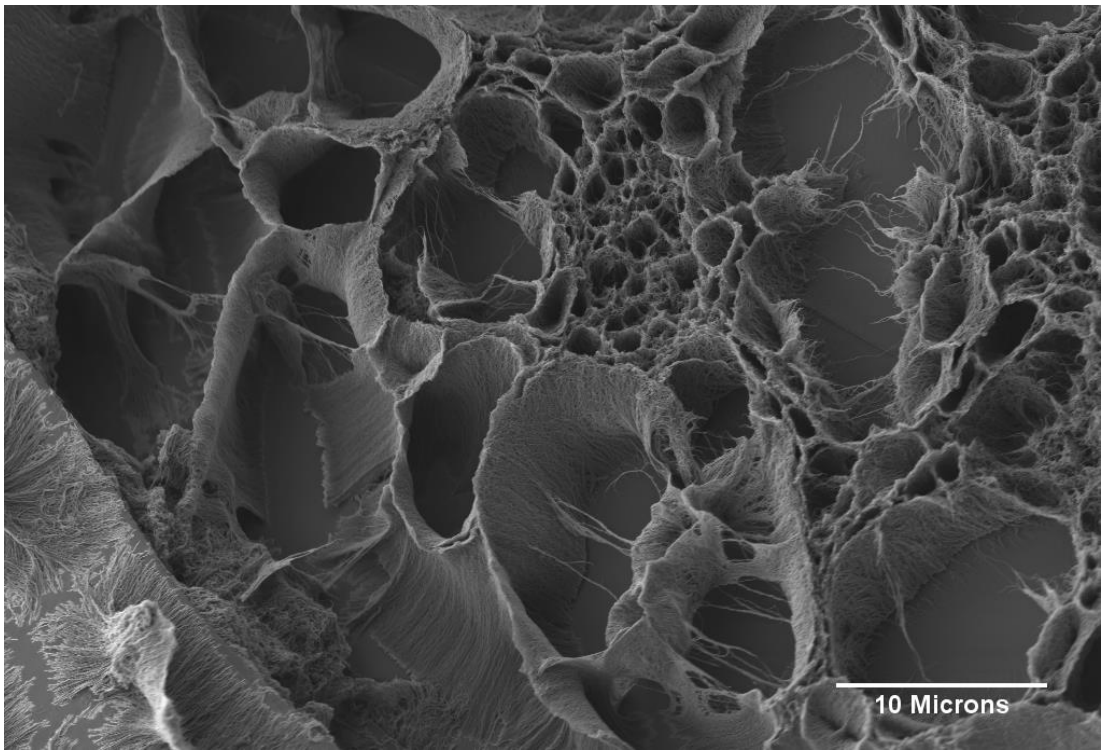

Figure 61: Top down SEM image of nanotubes grown on vermiculite at 675°C with pure ethylene after two incipient wetness impregnations

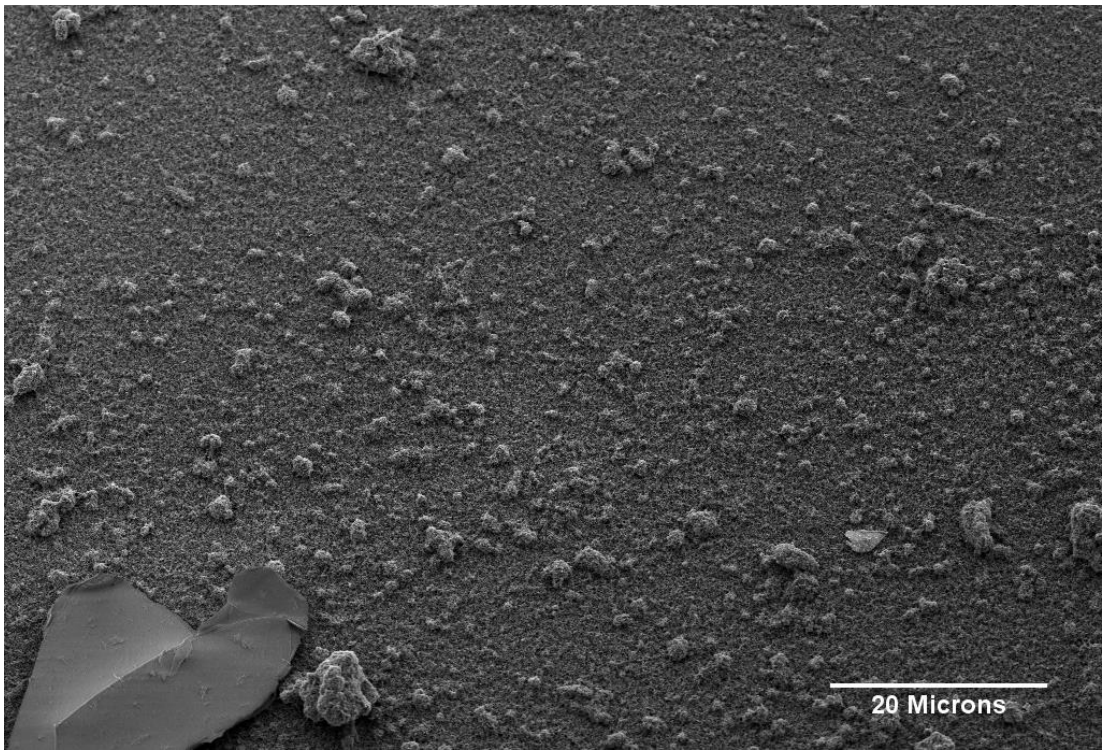

Figure 62: Top down SEM image of nanotubes grown on vermiculite at 675°C with pure ethylene after three incipient wetness impregnations

together under various pretreatments. Figure 64 shows a fleck of vermiculite with 5 micron nanotubes grown on and in between the sheets, with the sheets still held together. This catalyst was prepared with the triple impregnation method described elsewhere. Figure 65 shows a much thinner flake of vermiculite without other sheets directly attached. The only difference between the two catalysts is the single sheet was sonicated for 4 hours prior to the impregnation to break up the sheets. The overall particle size was significantly smaller, <80 microns, compared to the standard method, >150 microns. Additionally the sheets have separated, which should cause significantly higher surface area available for growth. The SEM image confirms the mica sheets were separated.

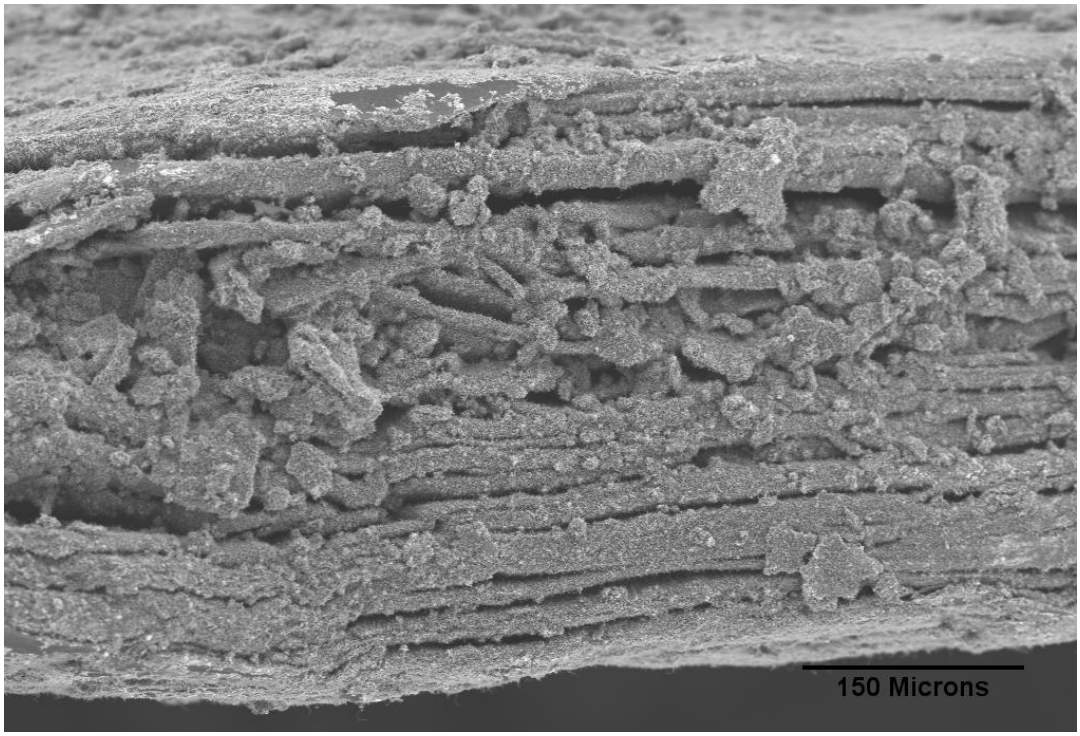

Figure 63: Side on SEM image of a stack of vermiculite layers, all of which exhibit growth while maintaining the integrity of the vermiculite layers. Forests were grown with ethylene at 675°C to a height of 5 microns

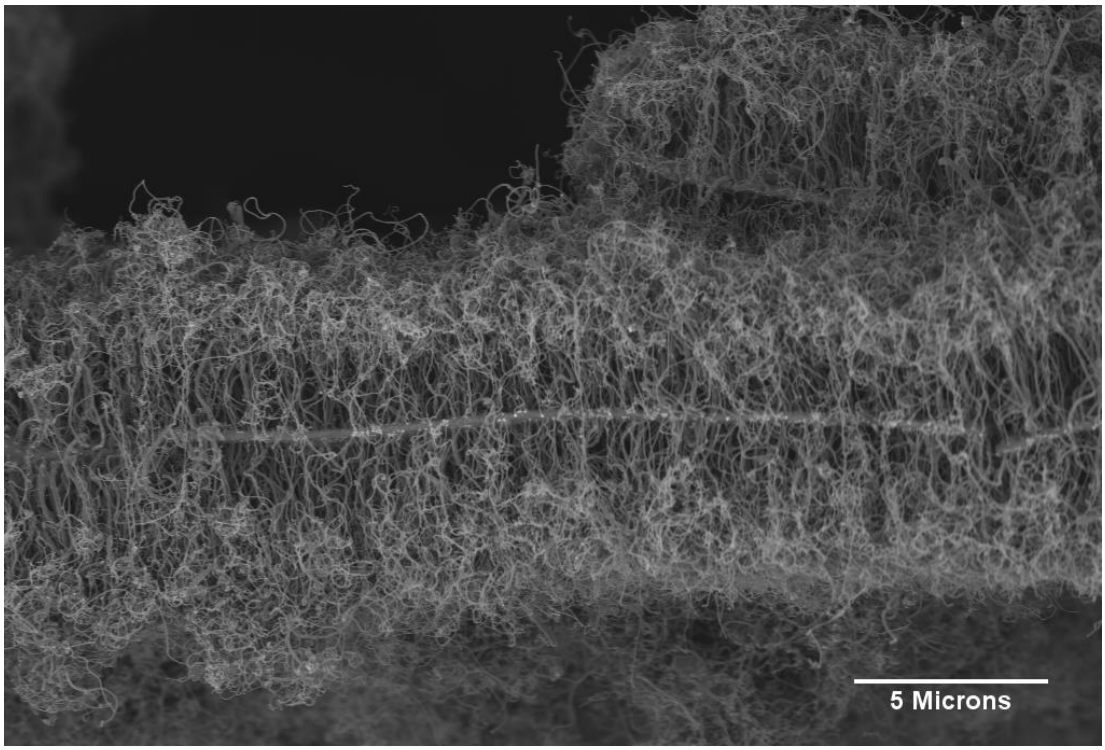

Figure 64: Side on SEM image of a single flake of vermiculite. Nanotube forest was grown at 675°C with ethylene to a height of 5 microns.

It was believed that the nanotube forests growth could force the vermiculite wafers apart if the forests were grown long enough. Figure 66 shows the nanotube forests which were ultimate used to grow block nanotubes, approximately 5-10 microns in length with half the length as nitrogen doped. In this instance the vermiculite sheets stuck together, possibly due to interactions between the tops of the nanotube forests, either the van der Waals forces which cause nanotubes to agglomerate in solution, or though a physical interlocking of the curly portion of the nanotubes. Figure 67 shows the same catalyst mixture grown with pure ethylene at 675°C for 20 minutes, reaching approximate 95 microns. In this case the lamellar layers have separated. The increased weight of each sheet of vermiculite with the large forest may cause the forces caused by the fluidization and collision of particles to outweigh the attractive forces of the nanotube forest, and lead to the separation of the sheets.

Growth Mechanism: Tip or Base Growth

It has been shown in literature than the difference between tip and base growth of the nanotube is the attractive forces of the catalyst particle for the substrate and the surface energy minimization achieved from the particle obtaining a spherical shape. At large catalyst particle sizes there are more sites with which to bond to the substrate, making base growth more energetically favorable. At very small particle sizes there are fewer binding sites, and a larger number of the atoms are on the surface as opposed to the bulk, making surface energy more important and tip or kite growth more favorable.

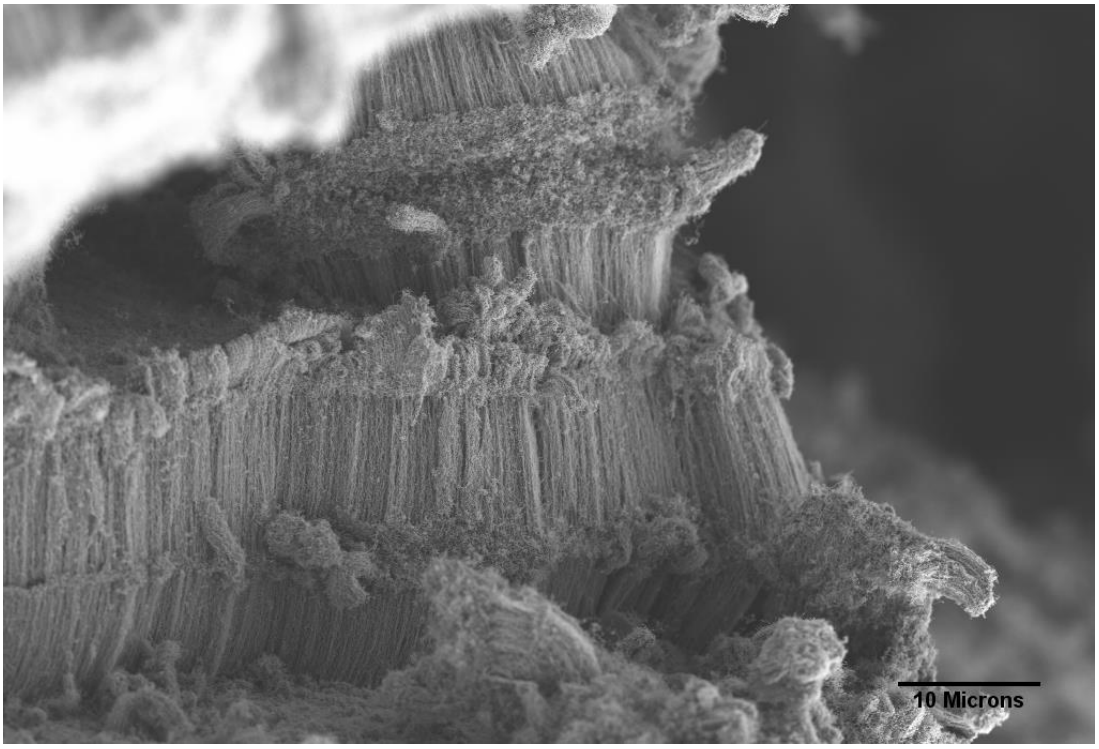

Figure 66: Block nitrogen doped nanotubes on vermiculite grown at 725°C with acetonitrile and ethylene as the feedstocks, showing the vermiculite layers held together by the nanotube forests.

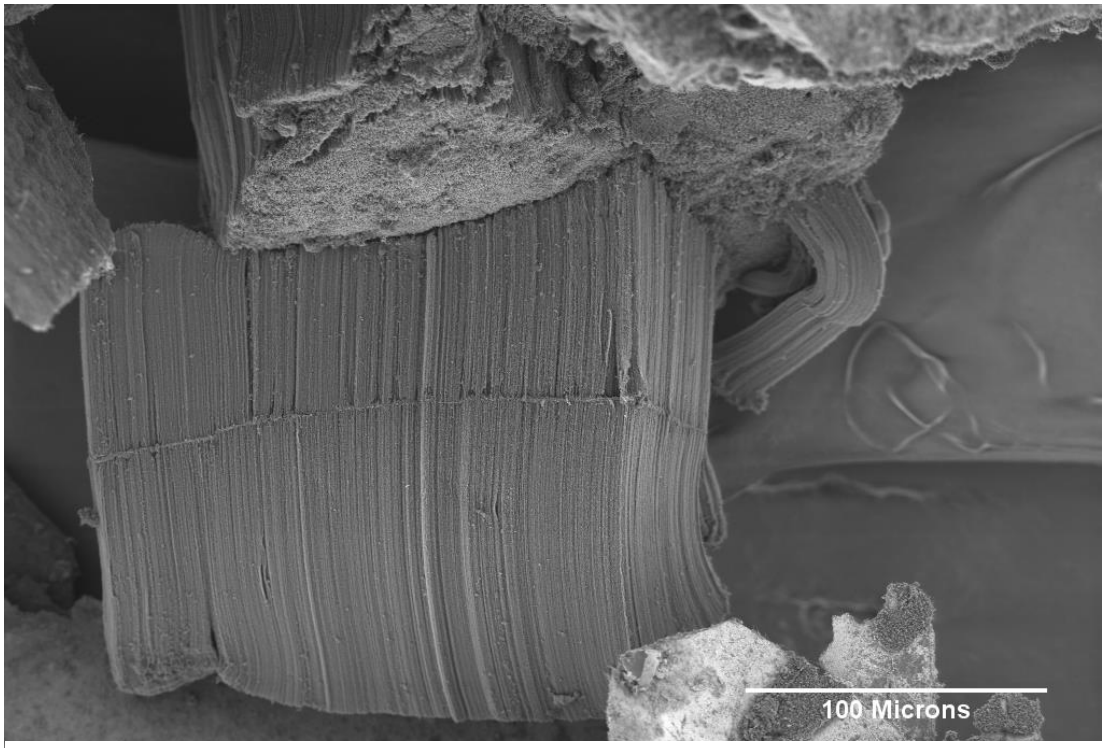

Figure 65: Nanotube forest grown with ethylene at 675°C on vermiculite for 20 minutes. The long forest length caused the vermiculite layers to separate.

The question has been raised as to which growth mechanism is present in the block functionalized nanotubes. I believe the answer is both are present with a majority being base growth based on the growth trials using two different temperatures for the different phases. For these nanotubes a layer of amorphous carbon layer was observed. It is possible this layer formed on the surface in between growth phases and was pushed up by continued growth. If the kite growth was present it would not be believable that a layer which spanned between nanotubes would form, but rather amorphous carbon would form along the nanotube and not span to adjoining tubes. However, it cannot be thought of as purely one or the other as several times under TEM a nanotube was observed which exhibited catalyst particles at both ends, such as seen below in Figure 68. The curled nanotube exhibits a dark mass at each end of itself, thought to be the catalyst pellet. It is possible that during a nitrogen growth phase, at the moment of slip a portion of the catalyst particle was bound tightly to the nanotube and part was forced to slip either through pressure buildup or a surface energy minimization, causing the particle to split in two. It is not likely in this case the particle left behind would be able to continue growth, however if it was bound to the surface it is possible. This would explain the fact that both sections near the catalyst particle exhibit little herringbone or bamboolike structure, indicating pristine growth.

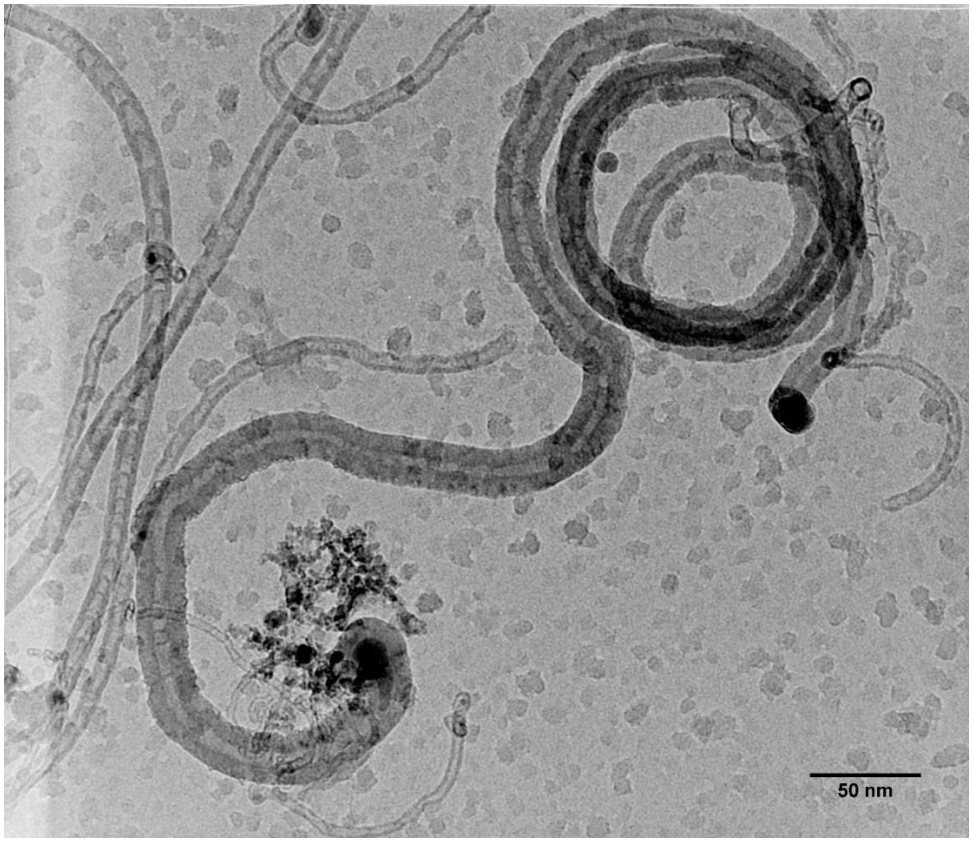

Figure 67: TEM image of a nanotube showing a catalyst particle at each end. The lack of bamboo or herringbone structure near either particle indicates both sides may have been available for growth during the ethylene growth phase.

Growth with Nitrogen Containing Precursors

Throughout literature there are reports of nitrogen doped nanotubes exhibiting either herringbone or bamboolike structure, particularly when grown on iron or cobalt catalysts. These terms are often used interchangeably, so much so that they have become synonymous in scientific circles. A herringbone structure however is technically a structure is in which the walls are at and angle to the direction of growth. The bamboo like structure is the walls are parallel to the direction of growth with sections which cross the middle of the

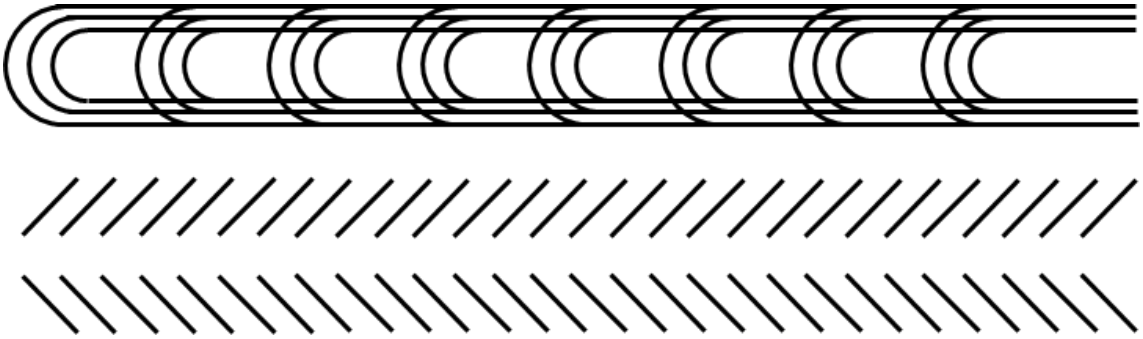

Figure 68: Diagram showing the difference between bamboolike structure (Top) and herringbone structure (Bottom)

tube, forming segments. The herringbone structure can be though of as a differentially small segment of the bamboo like nanotubes at the moment of slip as theorized by Holmes et. al. in Chapter 3, but without the crossing internal walls, likely from a lack of diffusion through the deepest part of the catalyst particle, or a lack of nucleation of these particles on the catalyst particle. The differences in the structure can be seen below in Figure 69. It is not known if the herringbone structure stays together by van der Waals forces or from defects in the walls linking them together, alternatively it is possible it is one or more spirals stacked inside each other.

The nanotubes grown with nitrogen in this project primarily exhibited a bamboolike structure, either faintly or heavily. A few nanotubes did show herringbone structure, primarily during the transition region between nitrogen doped and pristine. An example of this can be seen below in Figure 70. The pristine portion of the nanotube gives way to a section that clearly has herringbone structure along the wall, with a few bamboolike structures. As the herringbone primarily occurred in the transition regions it is likely a function of nitrogen content in the feed. Figure 71 shows only heavy bamboolike structure

with little to no herringbone. These nanotubes were grown at the same growth conditions, using different batches of catalyst, indicating another possible reason for the difference is minute changes in the catalyst composition.

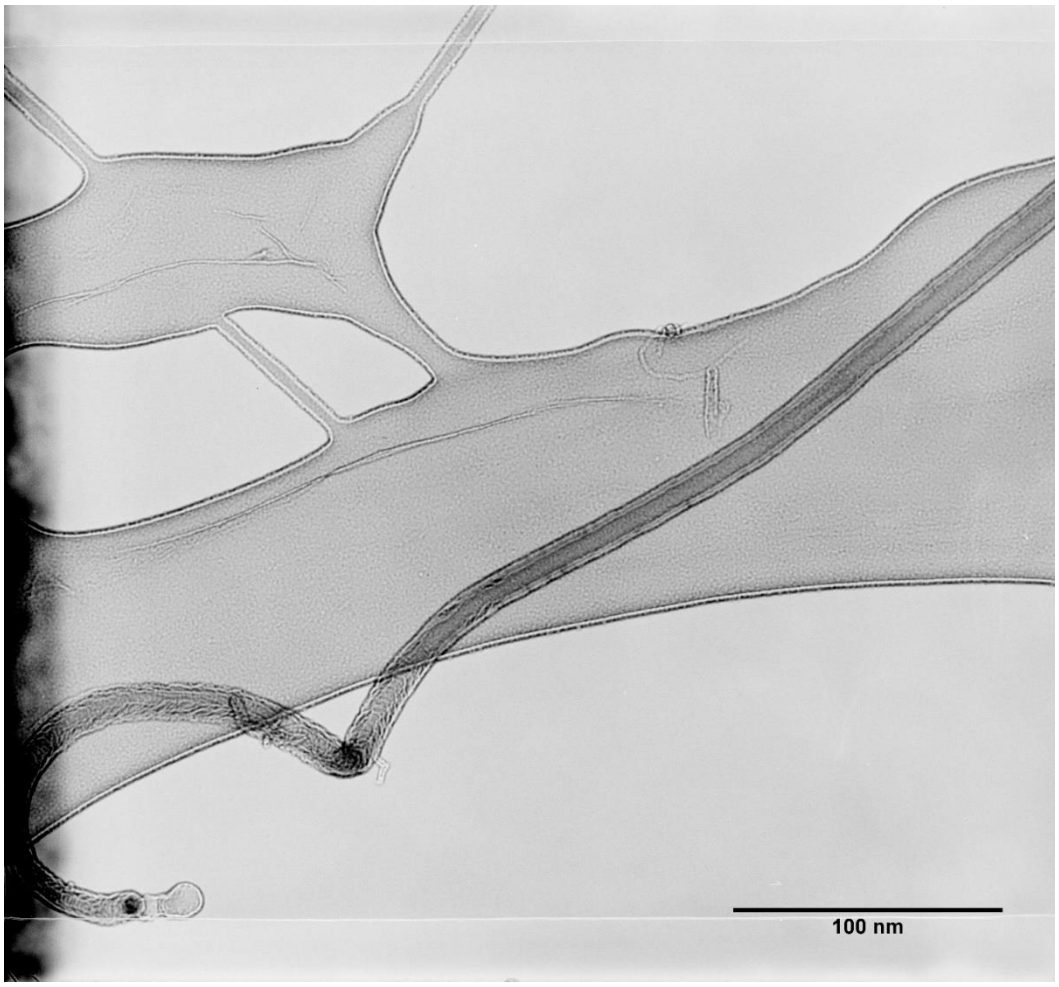

Figure 69: Block nitrogen doped nanotube demonstrating herringbone structure. In this instance the pristine section was grown prior to the nitrogen doped section, as indicated by the direction of the herringbone structure.

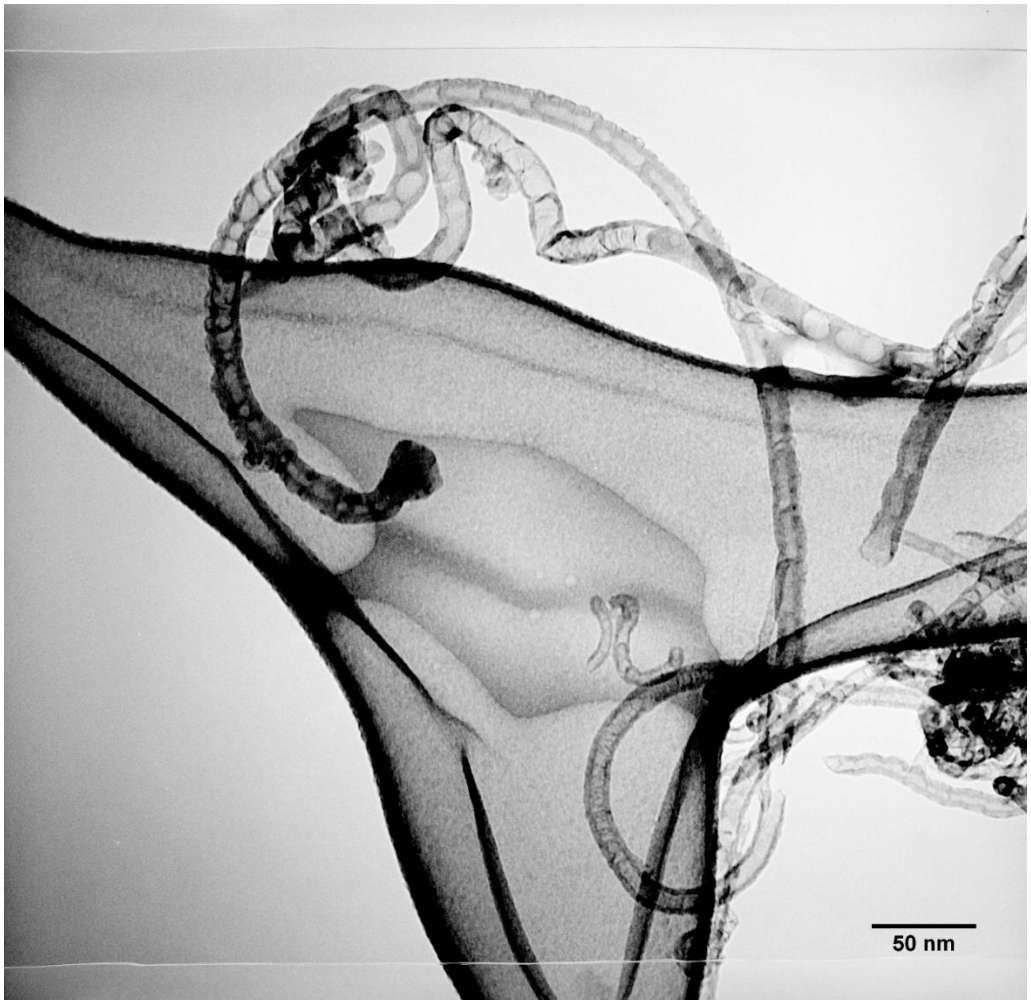

Figure 70: Nitrogen doped nanotubes grown demonstrating bamboo structure.